

Visualization Investigation of a Diesel-Gasoline Mixture Jet

by

Jiaxin Zhu

A thesis submitted in partial fulfillment of the requirements for the degree of

Master of Science

Department of Mechanical Engineering
University of Alberta

© Jiaxin Zhu, 2016

ABSTRACT

This thesis is an experimental investigation using optical methods to study atomization of fuel injectors for IC engines using a dual fuel mixture involving diesel and gasoline blends, which is called “dieseline”. Experiments were executed in a heated pressurized optical chamber which simulated some of the conditions typical in internal combustion (IC) engine fuel injection. High speed videography was used to obtain shadowgraph and Schlieren images which were used to evaluate the important atomization geometrical parameters of spray angle and penetration. The effect of fuel blending on fuel injection is shown.

The experimental chamber was heated up to 850 K from room temperature (approximately 300 K), so as to cover the non-evaporating and evaporating conditions of the jet. Optical access windows in the vessel allow the simultaneous measurement using two high speed cameras. Traditional shadowgraph of liquid fuel jet is obtained through one camera; while the vapor phase of the fuel jet is observed using focused shadowgraph technique, whose setup is similar to the Schlieren technique. A total of 189 injection events are investigated.

The effect of three input variables, chamber temperature, background gas density and injection pressure are studied on the jet penetration, quasi-steady liquid jet length, jet area and jet angle as output variables. The results show that dieseline fuel decreases the quasi-steady jet length significantly compared with pure diesel fuel, and the advancement of evaporation in temperature is less than 200 K in this study. The dieseline fuel is found not to change the sensitivity of the three input variables. Background gas density and chamber temperature are found to have significant influence on the quasi-steady liquid jet length. At the end, the experiment validity is checked with current literature.

ACKNOWLEDGEMENTS

Firstly, I would like to take this opportunity to thank my supervisor Dr. Brian Fleck for his continuous support and guidance throughout my study. His insightful thoughts help driving this research to the full extend, and I am highly motivated and inspired in this subject thanks to his rich knowledgeable advices. The internship opportunity provided by Dr. Fleck has been proved to be rewarding and the time I spent in B.I.T. has become one of the most cherishable memory in my life. I would also like to express my gratitude to my co-supervisor Dr. Bob Koch who has been always patience and helpful on this work. Dr. Koch's generously teaches me numerous academic skills and habits, which benefits this study and influences the rest of my life. I would to special thanks for both of my supervisors for their kind concerns when I was not physically fit after my return. Their support really helps me a lot in finishing this thesis.

Secondly, I would like to thank my colleagues in the Engine Labs of Beijing Institute of Technology. With Dr. Xu He's professional guidance, this experiment was progressing smoothly and encountered less difficulties. A special thanks to Mr. Yongli Gao, Ph.D. candidate and Mr. Bo Liu, M.Sc candidate. Both colleagues spent much of their valuable time helping me with the experiments. For the rest of the colleagues, I thank you all for the supports, and I enjoy the time spent with you while we are talking high about experiments, researches and life.

Thirdly, I would like to thanks colleagues in Dr. Fleck's group, Miss. Pallavi Bhambri, Miss. Jianfeng Hou and Mr. Nitish Sarker, who make my campus life vivid and sound. Their professional attitude toward researches and enthusiasm upon life always spur me to keep a positive attitude at school or at personal life. I feel very grateful to have met such elegant people.

Lastly, I want to specially thank my mother, who come all the way to Canada to help me tackle with my personal issues. Her support is really valuable especially at the end of finishing this thesis. Thanks for sacrificing her time and her help is really appreciated. Thanks for the support from all my family members, who send continuous support over the past years.

TABLE OF CONTENTS

1	Introduction	1
1.1	Research Motivations	1
1.2	Objectives of Experiment	3
1.3	Thesis Outline	3
2	Literature Review	4
2.1	Investigations in Turbulent Jet	4
2.2	Turbulent Jet in Fuel Injection	9
2.3	The Study of Dieseline as a Substitute Fuel	21
3	Equipment and Methodology	24
3.1	Equipment	24
3.1.1	General Assembly	24
3.1.2	Constant Volume Chamber System	26
3.1.3	Optical System	27
3.2	Methodology	32
3.2.1	Detailed Experiment Procedure	32
3.2.2	Processing Computation Scheme	34
3.3	Uncertainty	39
3.3.1	Instrumental Uncertainty	40
3.3.2	Repeatability of the Output	44
4	Results	48
4.1	Visualization Results	48
4.2	Gas Jet Results – from image post processing	57
4.3	Liquid Jet Results – from image post processing	64
4.3.1	Effect of temperature on vaporization	67
5	Discussion	71
5.1	Jet Self-Similarity Analysis	71
5.2	Sensitivity of Independent Variables	76
5.3	Comparison to the Literature	82
5.3.1	Penetration Data	82
5.3.2	Quasi-steady Jet Length and Jet Angle	85

6 Conclusion	88
6.1 Summary	88
6.2 Future Work	90
References	93
A Appendix A: Experiment Data Summary	102
B Appendix B: Liquid Jet Code Documentation	105
C Appendix C: Plots for Complete Data Set	108
D Appendix D: Temperature Calibration	121
E Appendix E: Injection Rate	123

LIST OF TABLES

3.1	Fuel properties	33
3.2	Independent variables	34
3.3	Scale factor uncertainties	42
5.1	Summary of sensitivities	80
5.2	Non-dimensional sensitivities	81
5.3	Summary of literature	82
A.1	Experiment summary 1	103
A.2	Experiment chart 2	104
D.1	Thermocouple temperature calibration	121
D.2	Derivation table	122
E.1	Injection amounts	125
E.2	Discharge coefficients	125

LIST OF FIGURES

2.1	Sketch of jet disintegration	6
2.2	Jet velocity response of sudden velocity change	10
2.3	Öz jet model	13
2.4	Jet angle and penetration definition	17
2.5	Diesel spray model	20
3.1	General setup	25
3.2	Combustion chamber	28
3.3	Temperature calibration	29
3.4	Light path setup 1	30
3.5	Light path setup 2	30
3.6	Flow chart of the processing schemes	35
3.7	Sample image of processing gas jet	37
3.8	Processing liquid jet	39
3.9	Noisy background subtraction results	44
3.10	Variations on a single run	45
3.11	Repetition tests	47
4.1	G20 videograph results at 300 K	50
4.2	Fuel jet time evolution for case buld1G20	51
4.3	Jet area ratio	52
4.4	G20 videography results at 850 K	54
4.5	Jet Details	55
4.6	Jet evolution with frame subtraction	57
4.7	Jet evolution details at 450 K	58
4.8	Jet evolution details at 550 K	59
4.9	Jet evolution details at 650 K	60
4.10	Gas jet behavior at various background gas densities	61
4.11	Penetration at different time	62
4.12	Gas penetration of G20 and G60 on density variation	63
4.13	Liquid jet penetration and jet area plot with background density variations	65
4.14	liquid jet penetration on various injection pressure	66
4.15	Examination of temperature variation on liquid jet	68

4.16	Jet area plots for the three fuel blends (G0, G20, G60) on temperature variation for Liquid Jet	69
5.1	Self-similarity prediction applied to vapor jet	73
5.2	Self-similarity prediction applied to liquid jet	74
5.3	Self-similarity evident on area plot	76
5.4	Self-similarity prediction with high temperature liquid jet	77
5.5	Jet area v.s. jet penetration	77
5.6	Jet self-similarity change over temperature 450 K to 650 K	78
5.7	The effect of density on quasi-steady liquid jet length	79
5.8	The effect of temperature on quasi-steady liquid jet length	79
5.9	The effect of injection pressure on quasi-steady liquid jet length	80
5.10	Different fuel effect on quasi-steady liquid length	81
5.11	Vapor jet penetration compared with literature	84
5.12	Quasi-steady liquid jet length comparison	86
5.13	Comparison of liquid jet angle with literature model	87
6.1	Pure background motions	91
C.1	Vapor penetration S on G0 fuel	109
C.2	Vapor penetration S on G20 & G60 fuel	110
C.3	Vapor area A on G0 fuel	111
C.4	Vapor area A on G20 & G60 fuel	112
C.5	Vapor jet angle θ on G0 fuel	113
C.6	Vapor jet angle θ on G20 & G60 fuel	114
C.7	Liquid penetration S on G0 Fuel	115
C.8	Liquid penetration S on G20 & G60 fuel	116
C.9	Liquid area A on G0 fuel	117
C.10	Liquid area A on G20 & G60 fuel	118
C.11	Liquid jet angle θ on G0 fuel	119
C.12	Liquid jet angle θ on G20 & G60 fuel	120
E.1	Injection Rate Profile	124
E.2	Discharge coefficient v.s. injection pressure	124
E.3	Discharge coefficient v.s. injection pressure for different gasoline percentage	126

NOMENCLATURE

Acronyms

CI	Compression Ignition
ECN	Engine Combustion Network
ECU	Engine Control Unit
FWHM	Full Width Half Max
IC	Internal Combustion
LTI	Linear Time-Invariant
NO _x	Nitrogen Oxides
PIV	Particle Image Velocimetry
PPCI	Partially Premixed Compression Ignition
QE	Quantum Efficiency
RAM	Random Access Memory
RCCI	Reactivity Controlled Compression Ignition
RGB	Red, Green and Blue
SMD	Sauter Mean Diameter
SNR	Signal-Noise Ratio

Symbols

a	Jet Angle Correction Constant used in Naber and Siebers [1996]
A_0	Jet Area of Nozzle
A_l	Liquid Jet Area
A_g	Gas Jet Area
A_x	Jet Area of Upstream Half ($< 0.5S$)
b	Detected Jet Pixels from Start to End
C_a	Area Contraction Coefficient of Nozzle
C_d	Discharge Coefficient of Nozzle
$C_{p,a}$	Heat Capacity of Ambient Gas
$C_{p,liq}$	Heat Capacity of Liquid Fuel
C_v	Velocity Coefficient of Nozzle
d_0	Nozzle Diameter
d_f	Corrected Nozzle Diameter by Naber and Siebers [1996]
h_l	Liquid Characteristic Length
h_{vap}	Vaporization Enthalpy
h_{ch}	Chamber Gas Enthalpy
h_f	fuel Component Enthalpy
I	Intensity Map of Greyscale Images
L	Quasi-steady Jet Length
M_{N_2}	Molar Mass of Nitrogen Molecule
m	Mass of Fuel (or Fuel Component)
Oh	Ohnesorge Number
P_{ch}	Chamber Pressure

P_{inj}	Injection Pressure
q	Non-dimensional Penetration Parameter with Naber and Siebers [1996]
r	Radial Location from the Jet Centerline
R	Jet Radius
R_{gas}	Universal Gas Constant
S	Jet Penetration
\tilde{S}	Non-dimensional penetration
S_l	Liquid Jet Penetration
S_g	Vapor Jet Penetration
t	Time after Injection
\tilde{t}	Non-dimensional time
T_{ch}	Chamber Temperature
$T_{b,max}$	Maximum Boiling Temperature of Fuel
u_0	Injection Velocity at Nozzle Exit
u_f	Corrected Jet Velocity at Nozzle Exit
v_l	Velocity of liquid
We	Weber Number
w	Jet Width
x	Jet Penetrating Direction Location
α	Corrected Jet Angle used in Naber and Siebers [1996] Penetration Model
β	Constant used at Musculus and Kattke [2009] Penetration Model
γ	Surface Tension
Δm	Injected Amount of Fuel Mass
ΔP	Pressure Difference across Nozzle

Δt	Difference of Time
η	Similarity Variable
θ	Jet Angle
θ_g	Gas Jet Angle
θ_l	Liquid Jet Angle
ν	Kinematic Viscosity
ν^*	Turbulent Fiction Factor
ξ	Similarity Variable
ρ_l	Liquid Fuel Density
ρ_{ch}	Ambient Density
ρ_s	Specific mass of Jet, Combined with Entrained Gas
τ	Time Constant for the First Order LTI
Ω	Jet Spreading Rate

CHAPTER 1

INTRODUCTION

1.1 Research Motivations

Engine research has been a vigorous topic for a long time because of its practical use and the concerns from the society related to vehicle emissions. As a major method of power supply to transportation vehicles, the efficiency and emission of an engine greatly affect the choice of consumers. The general awareness of global warming and greenhouse gas effect have driven cities and countries to produce more and more stringent vehicle emission policy, especially for the diesel fueled vehicles, while the understanding of the long term health effects of emitted particles from vehicles on the human lungs is driving IC vehicles to become environmentally competitive with zero emission power drives from electric and fuel cell engines.

A revolution in diesel engines was triggered by the common-rail system and its elevated injection pressures. It proved itself by meeting emission requirements and provided sufficient power for driving vehicles. Researchers continue to investigate the effect of pressure [Hariprasad, 2013] in modern compression ignition (CI). The improved spray quality has been proven and direct injection becomes possible in model engines, e.g. Volkswagen TDi diesel engines and Ford Ecoboost gasoline engines. However, the reduction of emissions will no longer simply rely on the pressure in-

crement, since many other parameters affect the spray as well [Parks et al., 1966]. Diesel engines have been widely used for heavy-duty jobs for their high power (torque) output compared with the gasoline engines, but they are notorious for the particulate emission problem. The recent scandal of Volkswagen diesel vehicles emission fraud in the U.S. has shocked the society and increased the demand for real emissions reductions.

The main gaseous pollutants from engine emission include oxides of nitrogen (NOx), carbon monoxide and unburnt hydrocarbons. The diesel engine also emits soot as a major pollutant, which is harmful to environment and is a severe magnifier of the greenhouse effect. Soot is formed by incomplete combustion, or it is partially burnt, meaning it can be eliminated by improving the combustion temperature (oxidation effect), yet high temperature environments will result in a higher rate of formation of NOx. The dilemma of the trade-off effect between NOx and soot emission is the imminent problem facing diesel engines [Anitescu, 2008]. To meet the current emission regulators, post combustion treatment devices are usually installed. These oxidizer devices usually require noble metals or dangerous chemicals (e.g. ammonia in selective catalytic reduction) as catalyzer which increases the vehicle manufacturing cost.

To solve this problem, alternative fuels were proposed as well as various injection strategies, e.g. pilot injection [Tanaka et al., 2002] and elevated injection pressured [Smallwood and Gülder, 2000]. Researchers have tried to employ different blended fuel to power the engines; diesel and gasoline mixture is one of the promising alternatives to diesel fuel. Diesel and gasoline blended fuel has already showed simultaneous reduction in soot and NOx in some diesel engine testes [Park et al., 2013]. While many researcher tried biofuel or pure substances (like ethanol [Michikawauchi et al., 2011]) to blend with diesel, gasoline and diesel blending is also more accessible as gasoline is already in massive production. As is known, petroleum refinement produces diesel,

kerosene and gasoline as the carbon chain gets smaller. By blending the light fuel to the heavy fuel products, the subsequent ignition properties are controlled. Reitz and his research group conducted a comprehensive survey on the reactivity controlled compression ignition (RCCI) engine with in-combustion-chamber mixing [e.g. Reitz and Duraisamy, 2015; Kokjohn et al., 2011; Splitter et al., 2011]. Their research involved ethanol and gasoline blended into diesel. Zhang et al. [2012] first used diesel and gasoline blend to conduct direct injection, and they called the blended fuel “dieseline”. In this study, the diesel and gasoline mixture single injection system is studied.

1.2 Objectives of Experiment

- Simultaneous measurement to the mixture fuel jet with focused shadowgraph and general shadowgraph technique
- Study the morphology of diesel and gasoline blend fuel jet
- Determine the parametric effect on the spray including the fuel type, injection pressure, chamber temperature, chamber background density

1.3 Thesis Outline

The thesis is divided into seven sections. Chapter 2 give introductive reviews on general fuel jet researches, with focus on diesel jet. Chapter 3 describes the experiment methods, equipment and estimate the experimental uncertainties. Chapter 4 gives the results on the results on experimental parameters, with discussion. Chapter 5 further explores the data with theory, fittings and validations with literature.

CHAPTER 2

LITERATURE REVIEW

2.1 Investigations in Turbulent Jet

Turbulence is defined for high speed fluid motion featured with vorticity dissipation, according to the Kolmogorov turbulent spectrum theorem. Tennekes and Lumley [1972] suggests that turbulent flow is viscous dissipative compared with random motion flows. Kolmogorov turbulent spectrum theorem further specifies that the turbulent dissipation is done by eddy transformations [Pope, 2000]. Fuel jets in IC engines are generally subject to turbulent motion. Turbulent jets have been thoroughly studied as a single phase as a shear free fluid flow, characterized by self-similarity. It has been relatively simple to model with Navier-stokes equation once the characteristic length, velocity were selected [Pope, 2000]. To further investigate the turbulent jet, the instability and jet mixing were of higher interest to researchers.

Early in 1878, Lord Rayleigh investigated the instability of jets caused by capillary force [Rayleigh, 1878]. At that time, the investigation of liquid jet was mostly done by including perturbation into the momentum equations. The analytical solutions for the linear stability of jet from Lord Rayleigh enhanced the understanding of jet development and was highly comparable with Savart's experiment [Eggers and Villermaux, 2008]. Further investigation on the jet breakup mechanism was also found by

Marmottant and Villiermaux [2004]. Later Batchelor and Gill [1962] investigated the inviscid fluid stability of a free jet with small disturbances. The historical development of liquid jet theory was well summarized by Eggers and Villiermaux [2008]. There were two non-dimensional numbers commonly used to describe the jet: the Weber number (We) and Ohnesorge number (Oh).

$$We = \rho_l h_l v_l^2 / \gamma \quad (2.1.1)$$

$$Oh = \nu \sqrt{\rho_l / h_l \gamma} \quad (2.1.2)$$

The Weber number is defined as the ratio of the inertia force to the surface tension, while the Ohnesorge number compares viscosity to surface tension. In the laminar jet case, the liquid surface tension and viscosity dominated the break up mode of the jet, therefore they were commonly mentioned for the past research and often extended to use in the turbulent jet studies. These two parameters were often included for plotting the jet penetration and spray angle correlation when investigating the effect of fluid properties. McCarthy and Molloy [1974] summarized the investigation of fluid jet break up. Many of the postulations utilized the two non-dimensional numbers to find the instability relations, both in the theoretical solutions and empirical solutions.

The observation of jet disintegration is shown in the rough sketch in Fig. 2.1, from McCarthy and Molloy [1974] who summarized previous works. The graph showed that the laminar jet disintegration differentiated itself from the turbulent jet disintegration. Each portion of the curve could be described by an empirical or theoretical equation, e.g. the empirical equation from Grant and Middleman [1966], $Z/d_0 = 19.5[(We)^{0.5} + 3We/Re]^{0.85}$ could be used to describe the BC portion, where Z was the distance of disintegration [McCarthy and Molloy, 1974]. Although the sketch was not necessarily completed for describing the relationship of laminar and turbulent jet, it revealed that the onset of turbulence did shorten the break-up length. A similar plot was

also given by Giffen and Muraszew [1953], who indicated that the period AC was breakup without air effect, period CD was breakup with air effect and period DE was wave-like breakup.

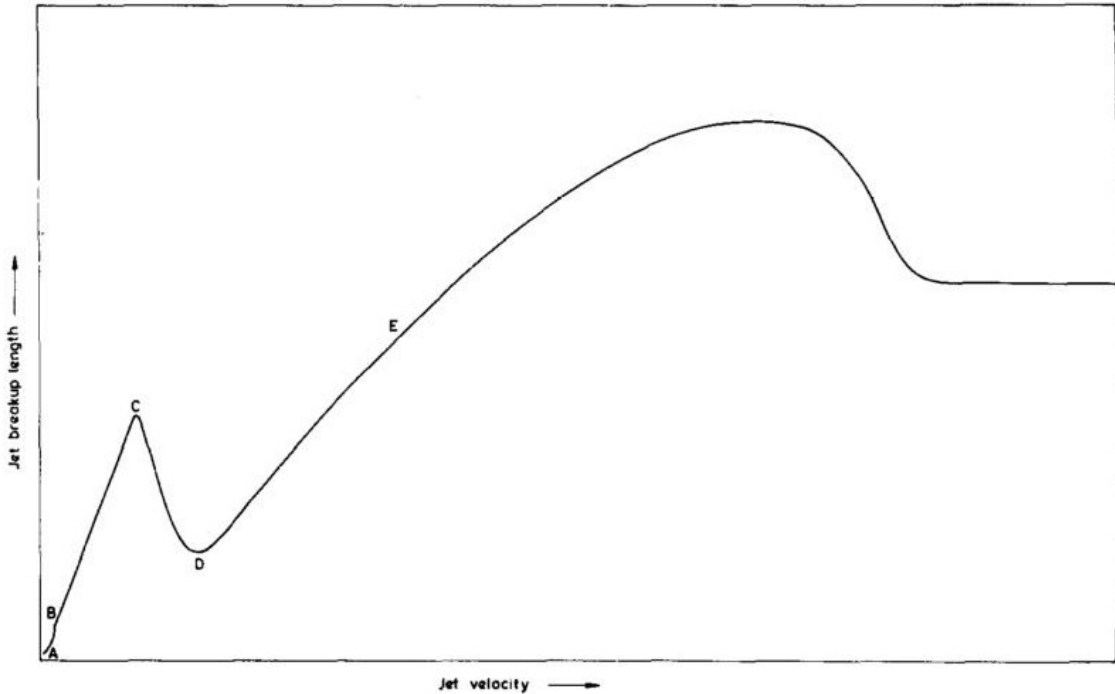


Figure 2.1: Sketch of jet disintegration [McCarthy and Molloy, 1974], reprinted with permission.

Further investigation on jet break-up can be found by Schweitzer [1937], who investigated the atomization of jets. For high pressure jets, the Rayleigh theory on the sphere globule collapse did not apply. The high pressure jet was known for aerodynamic break-up by air resistance and surface tension, as was often seen with diesel engine fuel injection [Schweitzer, 1937]. Schweitzer summarized some empirical equations from previous researchers and proposed his model of jet disintegration. His conclusions showed that the viscous force was significant, while the low pressure jet break up was most affect by the surface tension [Schweitzer, 1937]. However there was no decisive evidence that one kind of force would determine the disintegration length of a jet; the blended effect of surface tension and viscosity together determined

the atomization process. Schweitzer also observed that the outer surface of the jet was more laminar than the inside core. His model suggested that the transition to turbulence may not be solely relying on the Reynolds number. The surface roughness and the geometry of the nozzle play an important role in transition. The work of Schweitzer inspired the study of the relationship between fluid properties and jet disintegration.

National Advisory Committee for Aeronautics (known as N.A.C.A.) also had great interests in this subject in the 1930s. Haenlein [1931] imaged the spray with different kinds of fluid (water and mostly oils) into air. The report included the issuing velocity (highest at 73m/s) of the jet and used instantaneous imaging to visualize the jet motion, so as to investigate the disintegration length. These were possibly one of the earliest imaging techniques using to investigate the jet behavior. The fuel jet break-up images were further revealed by Lee and Spencer [1933]. The comprehensive set of images by Lee and Spencer [1933] covered the microscopic views on the ligaments and the measurement of the drop sizes. Their method was highly recognized and the advanced photographic methods were commonly used in current research. Later, Lee further investigated the impact of different nozzle designs on the fuel jet [Lee, 1936]. It was interesting to see that the images captured were able to identify the spray core and spray envelope (which was highly possible to be the gas jet). The trend of penetration was based on the injection pressure and ambient air pressure was also investigated in their study.

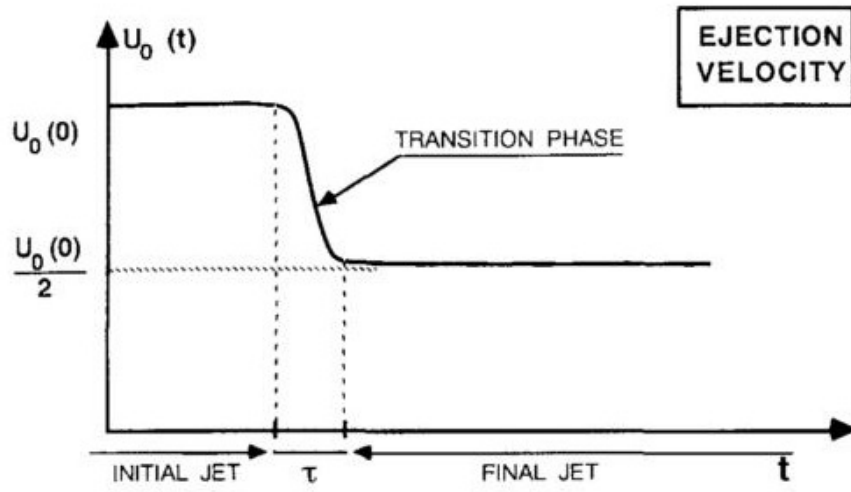
While the work done with the laminar jet was important in understanding the basics of the jet, this study will focus on the study of turbulent fuel jet atomization, where no theoretical solution exists. The difficulty of predicting an atomized jets behavior was obvious; for the two phase nature and the unknown boundary condition (or the unknown internal flow). Consequently, researchers can only deduct the relation from the emanated jet. The large-scale structure of turbulence was investigated

by Crow and Champagne [1970] for the study of jet noise. The study was completed on a single phase gas jet. The study of the gas jet was different from the liquid jet because of the buoyancy effect and the gas jet is compressible, leading to a different boundary conditions or internal flow condition. Yet the study was complementary to a vaporizing liquid jet, where the behavior may be similar to gas jet. The imaging results of these reveal the “vortex train” structure in the beginning the jet [Crow and Champagne, 1970]. After knowing the vortex shedding frequency, the preferred mode of the jet under a periodic force is characterized by the dimensionless frequency or Strouhal number. In addition to the direct imaging of jets, they employed Schlieren image photography to visualize the gas jet [Crow and Champagne, 1970]. Although the Schlieren visualization of a single phase jet by Crow and Champagne [1970] was not discussed in great detail, the method was found to be very useful in later studies on the vaporizing liquid jet. Later, Liepmann and Gharibs [1992] further visualized the jet with laser-induced fluorescence and investigated the persistency of the vortices. Their cross-sectional images related the entrainment process with the vortices. In addition, their particle image velocimetry (PIV) technique maps the entrainment velocity relative with the positions of the vortices. The results strongly related the entrainment effect with vortices, or in other words, the growth of vortices was the main mechanism corresponding to entrainment [Liepmann and Gharibs, 1992]. In the 1990s, Boree and his coworkers conducted a series of experiments investigating the axisymmetric turbulent gas jet with hot wire anemometry and visualization techniques [e.g. Atassi et al., 1993; Borée et al., 1996, 1997]. They took the study further by understanding that the vortices only displayed orderly structure at the beginning if the jet was forced [Atassi et al., 1993]. They imposed a sudden decrease of exit velocity to the jet so as to avoid the orderly vortices. They hoped that the response of the jet to the sudden velocity decrease would increase the turbulent mixing, and in their calculation the entrainment rate is increased [Borée et al., 1996]. Their experiments were

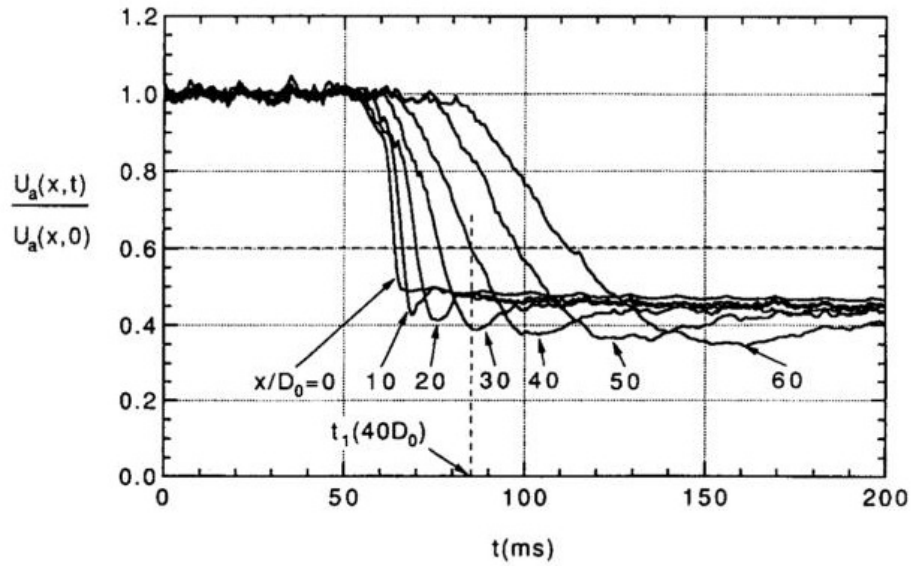
novel to this field because they investigated the response of a jet subjected to a certain changing perturbation pattern and proved the hypothesis with experiments. The jet velocity actually undershot when the exit velocity decreased, which was kind of like a proportional-integral-derivative (known as PID) controller as seen with Fig. 2.2. At different longitudinal location (x/d_0) of the jet, the response of the velocity change undergoes the different undershoot. The perturbation was therefore another possible method to improve the jet control. These experiments conducted with gas jet were related to the aircraft propeller system most of the time. Their researches greatly enhanced the understanding of turbulent jets which in turn was helpful to understand the two-phase jet investigated with this study and often presented in direct injection engines. The decelerating jet was further solved by Musculus [2009]. By that time, the analysis was already coming close to the fuel spray used with direct injection engines. Unlike Boree et al., Musculus applied momentum flux perturbation to the jet. The results allowed Musculus to evaluate the penetration, mixing ratio or even the equivalence ratio of the jet [Musculus, 2009]. However, the model developed by Musculus [2009] does not captured the experimental undershoot from Borée et al. [1997].

2.2 Turbulent Jet in Fuel Injection

CI engines require the fuel to be finely atomized when entering into the environment, since the atomization is believed to increase the vaporization of fuel jet. Control of combustion relies on the equivalence ratio, where the turbulent mixing takes effect. The general relation between atomization and turbulent mixing is unclear. The general characterizing parameters includes the Sauter mean diameter (SMD), defined as the ratio of total sum of drop volume to the total sum of drop surface area, spray penetration and spray cone angle. The early investigations were well documented in



(a)



(b)

Figure 2.2: Jet velocity response of sudden velocity change (Left: step input, Right: response) [Borée et al., 1997], reprinted with permission.

Giffen and Muraszew [1953]. Austen and Lyn [1960] found the atomization, measured as SMD, has an inconclusive effect on the combustion process. Yet the improvement of common rail system injection pressure over the past decades has proven that the atomization has a positive effect on the combustion process and can be seen in Fig. 1

of Smallwood and Gülder [2000]. The relationship is certainly a must when conducting engine research. Most of the time, it was impossible to instantaneously measure the SMD of drops in an engine or a pressure vessel. Therefore, the visualization technique became an important tool to evaluate the spray. The modern investigation of diesel injection is largely led by the Society of Automotive Engineering (known as S.A.E.), who continues to have substantial impact on this subject. Parks et al. [1966] did their visualization experiment on spray penetration. Perhaps the spray penetration depth and spray angle were the most obvious parameter for investigation, most researchers used these two parameters to characterize the spray jet, and the two parameters affect the combustion chamber design most. Parks et al. modified the equation proposed by Schweitzer, and included the chamber environment gas temperature into the correlation for better estimation. The equation developed by them was,

$$\frac{s}{d_0}(1 + \rho_{ch}) = 200 \left\{ \frac{\rho_{ch}\sqrt{\Delta P}}{d_0} \left[1 - \left(1 - \frac{d_0}{d_{ref}} \right) 1.12 \times 10^{-3}(T_{ch} - 70) \right] \right\}^{0.6} t^{0.6} \quad (2.2.1)$$

Their equation used imperial units (inch, lb.wt and Fahrenheit). By observing the equation, it can be found that the equation used a reference orifice diameter d_{ref} (0.6 mm). The use of a reference diameter limits the applicable range of the equation. When the orifice diameter was the same as the reference diameter, the ambient gas temperature calibration was invalid. It also seems that if the orifice diameter is smaller than the reference diameter, the higher ambient temperature takes a negative effect on the penetration length. Therefore, the applicable range of the equation was limited to diesel injection environment, reasonably large orifice diameters, and possibly non-evaporating sprays (highest test condition used was 538 °C). Although the equation may not be very useful for plotting the penetration of current diesel engine injections,

it tells us that the penetration did not increase linearly with time. Excluding the fuel properties (which was not considered in his experiment), the pressure differences contribute most to the penetration. The starting of the fuel jet penetration has higher penetration speed compared with the later jet, reading from the graph. The development of the equation was useful in preventing (or improving, depends on the engine design) fuel impingement therefore it was highly stressed in the literature. The summarized list of equations was given by Hay and Jones [1972]. It can be seen that there were continuous efforts from 1950s to develop a good correlation for the fuel jet penetration. Hay and Jones [1972] concluded that the equation developed by Dent was the most effective one by the time of the paper.

The modeling of fuel jet has led to fruitful results, including Dent [1971]. The results from Öz were also very impressive in the way the model was set up and processed. By assuming the jet was a free jet, Öz [1969] used the Navier-Stokes equation to model the jet. The biggest assumption by Öz was the elimination of high pressure component of the jet, and Öz assumed that the jet pressure within the jet was equal to the background pressure. The background pressure effect was investigated by previous researchers, who also developed an empirical equation on the penetration length [Öz, 1969]. Öz further pushed this investigation with constant pressure within the jet, so as to solve the 1-D Navier-Stokes equation and continuous equation. By employing the self-similarity ($\eta = r/x^n$), the stream function was defined by $\psi \propto x^k F(\eta)$, where n and k are constants. Solving the Navier-Stokes equation, the stream function and η was given, the following was the axial velocity (u) and the model given by Öz was shown in Fig. 2.3.

$$u = \frac{3}{32} \cdot \frac{\rho_l}{\rho_s \nu^*} \cdot \frac{u_0^2 d_0^2}{x} \cdot \frac{1}{[1 + (\xi/2)^2]^2} \quad (2.2.2)$$

$$\xi \propto \eta = \sqrt{\frac{3\rho_l}{\rho_s}} \cdot \frac{u_0 d_0}{8\nu^*} \cdot \frac{r}{x} \quad (2.2.3)$$

where ρ_s was specific mass of the jet (combined with entrained gas) and ν^* was the turbulent friction factor. Due to lack of information these two variables, the solved penetration equation (not given here) by Öz was not readily usable. Thus, later in the paper, they gave out another empirical equation.

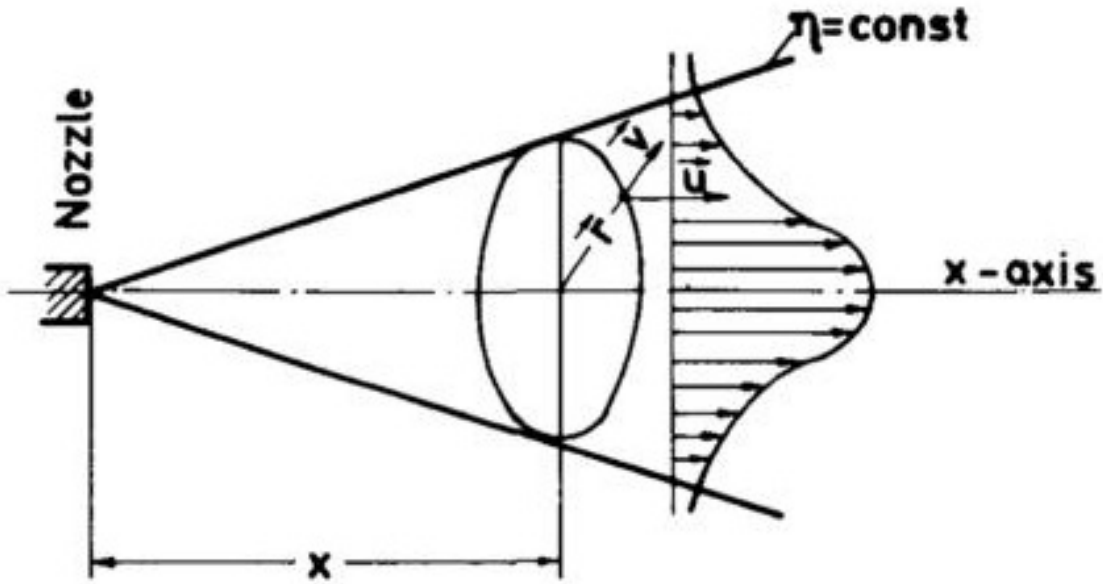


Figure 2.3: Jet model by Öz [1969], reprinted with permission.

The axial velocity solved by Öz's equations suggested there was maximal (in the axis) and minimal (in the edge) values in the jet, which was close to what was observed by this study and various other experiments. The theoretical contribution of Öz was greater than the empirical equation proposed. The analyses treated the fuel jet as a free jet, e.g. a single phase jet, thus Öz's work was more applicable to the non-vaporizing jet. However, the extended use of these analyses can be used in the vaporizing condition, as will be described later.

Dent took another approach to solve this problem. Dent treated the jet as a core-mixing two region spray, which was close to a vaporizing jet [Dent, 1971]. Yet the model was also applicable for non-vaporizing jets because the mixing was also quite

separated from the core region. By scaling the jet using equation (1) from Dent, the penetration can be solved. When solving the equation [Dent, 1971], empirical corrections were applied and the final form of the equation was given as,

$$S = 13.6 \left[\left(\frac{\Delta P}{\rho_{ch}} \right)^{1/2} \cdot t \cdot d_0 \right]^{1/2} \cdot \left(\frac{530}{T_{ch}} \right)^{1/4} \quad (2.2.4)$$

Imperial units were also used in this equation. The equation was perhaps the most widely used one before the 1990s for its accuracy over a wide range. The equation shows that the pressure drop across the exit, ambient gas density and temperature and nozzle diameter affects the penetration length. The equation by Dent was less counter-intuitive than Parks et al., which makes it suitable for many engine situations. The factors affecting the penetration may not be limited to the factors discussed above with Dent or Parks et al. Varde and Popa [1983] conducted a series of experiments showing that if the nozzle dimension and discharge coefficient were changed, the penetration relation will be altered as well. The experiments carried out by Varde and Pope alters the aspect ratio since the discharge coefficient was uncontrollable. They also induce surface tension, as the major fuel parameter, to their equation, which was similar to Oh number [Varde and Popa, 1983]. Yet they did not involve the background temperature to the consideration. The fact that Varde and Pope take the nozzle dimension into account is beneficial to the direct injection engine designs, but it was also difficult to consider every single factor into the equation. Most equations developed were only suitable to specific conditions. The point was not to find the best solution to the jet penetration, but it was when the conditions were defined, one could adapt the most suitable equation to solve the problem. Indeed, Reitz and Bracco [1982] investigated the atomization mechanism of a liquid jet with a two-phase Navier-Stokes equation, and tried to explain the problem with surface wave growth perturbation (see their Equation 2 with the perturbing velocity

and pressure). They observed that a single mechanism alone may not be sufficient to explain the aerodynamic break-up, so one needs to understand the cavitation condition of the internal flow [Reitz and Bracco, 1982]. The empirical equations suiting the need of certain conditions consequently will not be very accurate for the absence of boundary conditions, which was determined by the nozzle internal flow. A further three dimensional analyses can also be found in the work of Li [1995], who conducted a complex investigation on the impact of wave growth rate on the jet disintegration.

In addition to the penetration depth, the spray angle was also a major parameter of interest in understanding the spray atomization mechanism. However the spray angle was not a parameter easily measured. The manual measurement of spray angle was not very reliable because the definition of it was inconsistent, since the spray plume is not a perfect cone, or triangle in the two dimensional perspective. Some researchers used near-field and far-field angle as a set of spray angle definitions but this further involves the definition of near-field and far-field. Measurements became troublesome if the definition method was not clear. The spray angle empirical equations were seldom proposed by the researchers. Hiroyasu and Arai [1990] gave their empirical relation (in their equation 2) based on their image measurement. Their measurement reveals some trend of the spray angle. The jet tends to have a quasi-steady spray angle once developed. The quasi-steady angle was under 20° as this experiment was conducted without evaporation. Giffen and Muraszew [1953] indicated that the spray angle increases with higher ambient pressure without exceeding 20° according to their figure.

Most of the modern investigations on diesel fuel jets were done by the Sandia National Lab from the United States, and the engine combustion network (ECN) it initiated. The first prominent research from Sandia National Lab was done by Naber and Siebers [1996]. They provided a detailed description of the testing environment and the equipment used, which helped setting up the standard for many future studies.

The pre-burnt type of combustion vessel used in their lab was fully described in this study where the temperature error analysis inside the chamber became possible, compared with previous works that used the same type of vessel. Aside from these contributions, Naber and Siebers applied novel visualization methods to imaging the spray. They used high speed line-scan charge-coupled device (CCD) array and typical high speed cameras in their experiment. Their line-scan camera reached a frequency of 80 kHz, enabling them to evaluate the early near-field [Naber and Siebers, 1996]. The Schlieren setup used in their study was exemplary for the later studies. The Schlieren system was capable of visualizing a gas jet [Crow and Champagne, 1970] without the need for fluorescing additives in the fuel, and was also proven to be useful on combustion imaging [Pickett et al., 2009]. Naber and Siebers [1996] extended the method using a laser light source with or without Schlieren imagery. The images were clear to see even at high density condition of their tests. Similar images were obtained by Myong et al. [2004]. It was shown that the laser light was not so easily distorted by the dense ambient condition. But even with the laser light, the background noise for high density conditions could not be eliminated. Naber and Siebers [1996] gave the details of their digitalizing the film images (based on refined masking and intensity thresholding) and it appears that the calculated vapor jet contour was reasonable by human eye comparison. They used an iterative process to define the spray angle, expressed as,

$$\frac{\theta_g}{2} = \tan^{-1} \left(\frac{A_{jet,S/2}}{(S/2)^2} \right) \quad (2.2.5)$$

where the $A_{jet,S/2}$ was the jet area of the upstream half of the spray. The penetration, S , was also defined as the length when half of the arc (with an angle of $\theta/2$) occupied by the detected jet contour [Naber and Siebers, 1996]. Since the penetration and spray angle depend on each other by definition, an initial spray angle was

of radial locations or a top hat profile as shown in their appendices, unlike earlier model of Öz [1969].

Siebers [1998] conducted experiments to investigate the effect of fuel volatility on the penetration. Siebers found that higher volatility fuel results in shorter penetration length. The study was further pursued by Higgins et al. [1999], who proposed the correlation for the fuel properties.

$$\frac{L}{d_0} = 10.5 \left(\frac{\rho_l}{\rho_{ch}} \right)^{0.58} B^{0.59} \quad (2.2.6)$$

$$B = \frac{\sum_i m_i h_{vap,i} + (T_{b,max} - T_l) \sum_i m_i C_{p,liq,i}}{C_{p,a}(T_{ch} - T_{b,max}) \sum_i m_i} \quad (2.2.7)$$

where m was the mass fraction of fuel component, $T_{b,max}$ was the max boiling point of the fuel components and $C_{p,liq}$ was the heat capacity of fuel component at liquid state. The equations are quite comprehensive but too complex for most practical use. It requires the complete fuel composition to be known. Siebers spent another effort to investigate the maximum liquid length reached by the vaporizing fuel jet. Siebers asserted that the vaporizing jet was mixing limited, which means that the atomization or surface area of the liquid did not significantly affect the vaporizing state of the jet [Siebers, 1999]; in other words, the saturation state at the jet surface dominates the final evaporation. They used the energy balance and mass conservation equation to solve for the maximum length,

$$L = \frac{0.41}{0.66} \sqrt{\frac{\rho_l}{\rho_{ch}}} \frac{\sqrt{C_a} \cdot d}{\tan(\theta/2)} \sqrt{\left(\frac{2}{B_1} + 1\right)^2 - 1} \quad (2.2.8)$$

$$B_1 = \frac{h_{ch}(T_a, P_a) - h_{ch}(T_s, P_a - P_s)}{h_f(T_s) - h_f(T_f, P_a)} \quad (2.2.9)$$

where the constants, 0.41 and 0.66 were the correlated results from their experimental data. The correlation was compared with Versaevel et al. [2000] model by

Luijten and Kurvers [2010], including the real gas effects. Versaevel et al. [2000] included the energy balance equation into the model and applied it to computational simulations. Although Versaevel and Wieser did not explicitly give the penetration equation in their study, Luijten and Kurvers [2010] solved the equation of Versaevel et al. [2000] model and compared it with the Siebers [1999] equation [Luijten and Kurvers, 2010]. Their equations were very similar except there was an additional subtracted term in Versaevel et al. [2000]. Versaevel et al. [2000] model may be better in capturing the jet physics but Siebers [1999] equation was more accurate using Sandia's data set [Luijten and Kurvers, 2010]. Along with the maximum liquid length prediction, Siebers [1999] also gave an empirical equation for the measurement of spray angle, as shown below in Eq. 2.2.10, which was also included for modeling in Versaevel et al. [2000] and Luijten and Kurvers [2010].

$$\tan\left(\frac{\theta_g}{2}\right) = 0.260 \left[\left(\frac{\rho_{ch}}{\rho_l} \right)^{0.19} - 0.0043 \sqrt{\frac{\rho_{ch}}{\rho_l}} \right] \quad (2.2.10)$$

Musculus and Kattke [2009] improved the spray model, which is currently in popular use. They made several assumptions when solving the equation, including assuming a constant spray angle during the process. The velocity profile used was adapted from Abramovich [1963] as described in Fig. 2.5. The velocity profile resembles to a Gaussian function which peaks at the center and diminishes on both side [Musculus and Kattke, 2009], but it is not completely Gaussian. The Gaussian profile assumption was also used by Pastor et al. [2008], who used similar spray model as Musculus and Kattke. The analysis was fairly simple, where the velocity and mass fraction were averaged and used to solve the momentum and mass conservation. The discretization of the jet was solved using the upwind differencing, which made sense because the information only spread from upstream to downstream, judging from the strong unidirectional flow. The method gives a very good estimation of the

penetration and entrainment rate (or equivalent ratio if converted) and is easy to implement into the computational method. At the end of the study, they gave an analytical solution to the steady jet, the transient jet solution was discussed in their major study. The main result obtained from the study was the observation that there was an increased entrainment region which they called “entrainment wave” [Musculus and Kattke, 2009]. The wave speed was $2\beta\bar{u}$ as shown in the momentum wave function of equation in 2.10 of Musculus [2009], where \bar{u} is the averaged speed of the jet cross-section.

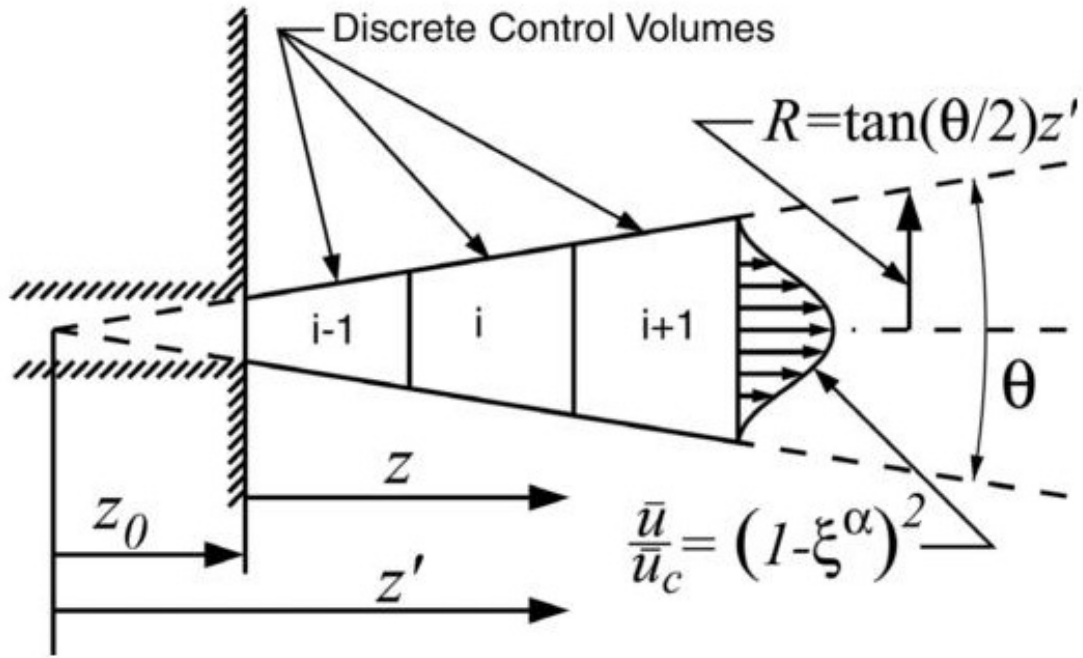


Figure 2.5: Diesel spray model by Musculus and Kattke [2009], reprinted with permission.

Musculus and Kattke [2009] along with [Naber and Siebers, 1996] theory was examined by Pickett et al. [2011]. Pickett et al. [2011] employed Mie scatter imaging (liquid drops), Schlieren Imaging (vapor jet) and Rayleigh scatter imaging (for equivalent ratio detection) to evaluate the jet. The results were compared with the variable

spray profile model (Musculus and Kattke [2009], but further derived in the penetration, constant β evaluation and transient time, see Pickett et al. [2011] Appendix A and Appendix B) with a constant spray angle of 21° (they used a different angle for better prediction, which ranged from 18° to 23°) The results were generally matched with the prediction, and some uncertainties in the equivalence ratio was concluded from the low signal of Rayleigh scatter imaging. Recent developments with the ECN group focused on the early stages of jet growth. Pickett et al. [2013] investigated the start of the penetration period in comparison with Naber and Siebers [1996] experiment.

The ECN group has spent great efforts in exploring and standardizing the fuel spray environment; comparison of experimental data can be found in literature [e.g. Bardi et al., 2012; Pastor et al., 2012; Pei et al., 2015]. The improved theoretical solutions were helpful in predicting the design and improvement of engine combustion systems [Reitz and Bracco, 1982]. With the understanding of the current developed fuel jet model, this study carries on to study the effect of gas properties on fuel spray with dieselene being used in this study. Known as a promising fuel for low temperature combustion and supercritical fuel injection, the dieselene spray was fully characterized in this study.

2.3 The Study of Dieselene as a Substitute Fuel

Fuel properties are important parameters for fuel injection, and have been widely studied [e.g. Higgins et al., 1999; Dernet et al., 2012]. Published works indicate the use of different kinds of fuels or fuel substitutes (n-heptane, n-dodecane) to test for the influence of fuel properties. Obviously, different fuel types often have a wide range of fuel properties (heating value, viscosity and etc.). Consequently, the experiment results are difficult to compare when the variations in fuel properties are considered.

Furthermore, although fuel blends may add more complexity, it has the potential to provide researchers design and control tool to the fuel properties. This was where the concept of reactivity controlled injection came into play. As was mentioned in Chapter 1, the concept was well-documented in Reitz and Duraisamy [2015]. Different fuels were injected and mixed inside the combustion cylinder to achieve control over the ignition delay. By avoiding misfire or knock issues inside an engine using reactivity controlled techniques, the engine emissions were effectively controlled for the dual fuel blend of diesel and gasoline [e.g. Leermakers et al., 2011; Kokjohn et al., 2011]. Similar control of fuel properties is possible with biofuel and ethanol as these fuels become more popular.

The direct mixing of gasoline and diesel before injection was proposed to avoid stratification in the cylinder, along with the benefit of minimal modification to the current injection system, but again the combined chemical and physical properties need to be thoroughly studied [e.g. Bao et al., 2014; Anitescu et al., 2012]. The early direct injection experiment with dieseline was done by Turner et al. [2009] and Zhang et al. [2012]. The diesel and gasoline mixture injection and combustion was usually related to application in the partially premixed compression ignition (PPCI) mode in contrast with the RCCI mode. PPCI has fuel stratification only within the one single shot of injection. The fuel and air mixing becomes the barrier to ignition. In this strategy, the dieseline direct injection was harder to control in terms of ignition delay, compared with in-cylinder fuel mixing. The achievement of dieseline direct injection could greatly reduce the particulate pollutant production. Many of the current researches face the “diesel dilemma”, which means some of the other pollutants (NO_x for example), will be increased concurrently with this soot reduction method. Dieseline direct usage is studied by Park et al. [2013] who partially conquered this in a traditional four-cylinder diesel engine. They showed the pollutant emissions were reduced by adding a small amount of gasoline into the diesel fuel. All

this promising results lead to the current study of this thesis, an optimal injection condition for the diesel and gasoline must be obtained.

Looking forward to the future study of fuel injection, dieseline fuel is a suitable fuel for supercritical injection. Supercritical injection referred by the aerospace industry is the case when a jet became supercritical after kerosene or hydrogen fuel were injected into the combustion chamber, due to the high pressure and high heat in the aircraft engine [Seebald and Sojka, 2011]. However, researchers were curious about effects on jets if the fuel was supercritical before entering the combustion chamber. In the supercritical state, physical properties of the fuel change dramatically, and the jet forming mechanics shall change accordingly. It is believed that this helps to promote the boundary air-fuel mixing. When conducting diesel supercritical researches, it was known that diesel fuel coked at a temperature around 400 K, even when it was pressurized to maintain a liquid state. Blending gasoline into diesel helped preventing the fuel from coking in high temperature, and therefore the current injection system could be kept with minimal modification Anitescu et al. [2012].

CHAPTER 3

EQUIPMENT AND METHODOLOGY

3.1 Equipment

3.1.1 General Assembly

The purpose of this experiment is to monitor the fuel jet with high speed videography. The liquid and vapor phases of the fuel jet are captured simultaneously so as to attain a direct comparison. The assembly of this experiment is similar with engine combustion network labs as were summarized in Bardi et al. [2012]. Major components of this setup include a combustion pressure vessel and optical instrumentations, provided by the Engine Labs, Beijing Institute of Technology. Fig. 3.1 shows the schematic of the setup, with the positions of cameras shown. The combustion chamber is a constant volume vessel of about 100 cm height. The observation chamber is elevated at 120 cm from the ground to properly position the gas vacuum pump. The system incorporates an engine control unit (ECU) to coordinate time signals of injections.

This setup is used to examine three different types of fuel under high pressure injection: pure diesel (denoted as G0), 20% gasoline blended in diesel (G20) and 60% gasoline blended (G60). In the case of switching fuel for the test, the fuel supply tank and the fuel filter have to be replaced to avoid contamination. To eliminate the residual fuel from the previous test, the fuel supply pipe, the injector and the

common rail pump must be recirculated for a period of 100 injections using the new fuel.

To briefly summarize the procedure of the experiment, the chamber is pressurized and preheated to the set temperature by the controller. Fuel starts circulating from the supply tank to the return tank, and the injector is pressurized. Then the ECU gives a launching signal to the injector and the two cameras to trigger the injection and recording. Three injection events are saved to the hard-drives from the random access memory (RAM) of the cameras. Only three injections can be recorded before the RAM was filled. Then compressed nitrogen gas purges the system and then the chamber vacuumed after each injection run and the return fuel is disposed in the end.

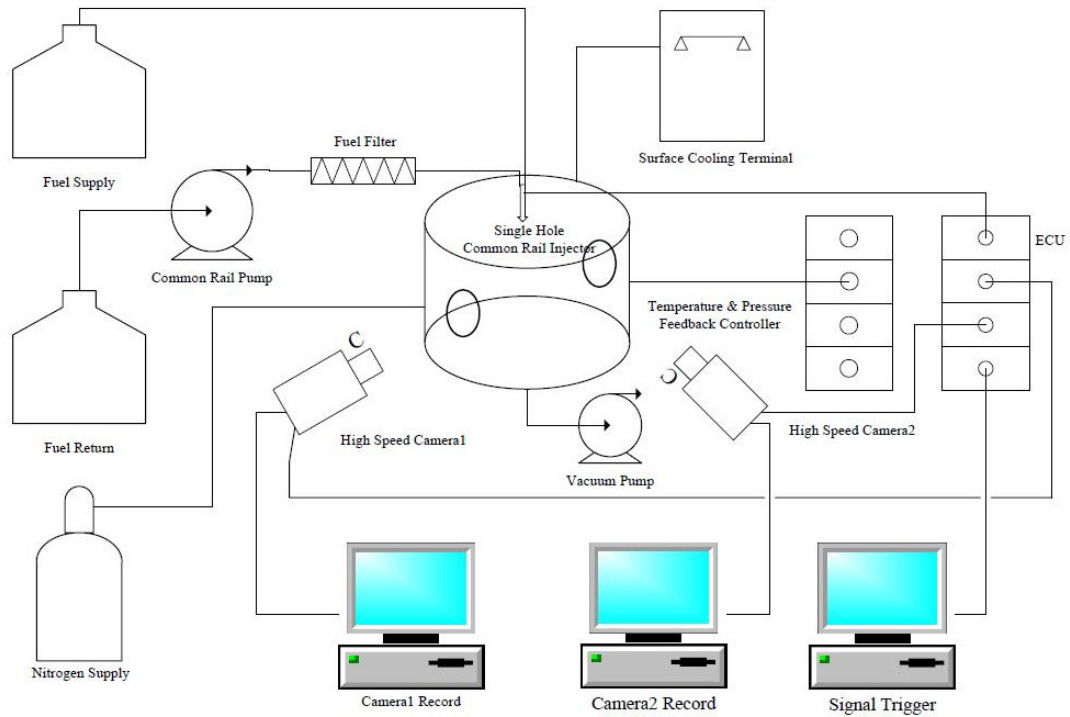


Figure 3.1: General setup.

3.1.2 Constant Volume Chamber System

In order to simulate the actual engine stroke condition, a constant volume pressure chamber is used. There are different types of combustion chambers used in similar setups. The one used by the Sandia group in the 1990s would be the ignition type of chamber [Naber and Siebers, 1996; Bardi et al., 2012]. This type of chamber pre-burns the fuel and air mixture inside the chamber to achieve high temperature and pressure. The air-fuel ratio must be exactly stoichiometric so that there is no residual air to affect the inert injection event. Usually diesel engine runs at lean condition, but the injection tests focus on the observation of the jet development. Therefore, stoichiometric ratio is used to avoid the jet burning. The chamber used by the Sandia group also includes an internal fan to promote mixing and heat convection. Another type of chamber is used by Universitat Politècnica de València CMT-Motores Termicos, with continuously heated flow through the chamber [Bardi et al., 2012]. The compressed and heated gas is generated outside of the cell and is continuously transported to the chamber. The inflow is at negligible velocity compared to the jet velocity, and it is capable of creating a “nearly quiescent, and steady thermodynamic conditions” [Payri et al., 2012]. The flow is kept with low speed to avoid affecting the injection event. The chamber used in this thesis is a third different type, which involved electric heating and constant volume chamber.

The internal volume of the chamber is heated with an electric heater, and it is capable of maintaining an inside temperature up to 900 K. The advantage of this setup is that it enables large volume of measurement and the flow is relatively stationary during the injection events. The chamber is also pressurized up to 6 MPa to mimic the high pressure around the top dead center of the piston. The pressure transducer inside chamber is model P30 manufactured by E+H. The chamber gas density is calculated from temperature and pressure using ideal gas law. After the calculation, maximum

gas density of chamber is found to be 22 kg/m^3 . The chamber is also built with optical path accessibility. There are four observational windows for the arrangement of optical light paths. Each opposed pair of the windows allows one light path to go through and the two pairs of windows are orthogonally arranged, which minimizes the light interference. To avoid overheating the optical glass windows, recirculation of coolant is used to lower the metal temperature around the windows.

The injector used in this experiment is a Bosch single-hole diesel injector, but its tip is customized to be $120 \text{ }\mu\text{m}$ by a local manufacturer. The injector is pressurized with a common-rail system. The common-rail pressure is monitored by feedback sensors. In this experiment, the injector was pressurized to 140 MPa.

The temperature of the vessel is measured with near wall thermocouple. The K type thermocouple (serial: WRNK-101) has a diameter of 1.5 mm and a length of 300 mm, and is capable of measuring temperature from 0 to 1000 °C. Calibration experiments are done to estimate the difference of the near wall temperature with the inside of the chamber by placing three thermocouple aligned with the nozzle center line, as is shown in Fig. 3.3. It is found that at low temperature the difference is small, while the difference enlarges at higher temperatures. At the highest temperature, the centerline temperature would have a temperature of maximum 30 °C higher than the near wall thermocouple. The experimental data are shown in Appendix D. For consistency of reporting, the near wall temperature will be used.

3.1.3 Optical System

Two optical assessments are used to monitor the spray process: one is backlit shadowgraph with stage lamp, and the other is focus shadowgraph method where a Schlieren arrangement is used (without the knife-edge), lighted with a USHIO xenon lamp. The two systems utilize the two orthogonal light paths mentioned above at the same time. The term “focus shadowgraph” is mentioned in Settles [2001] and Sandia reports

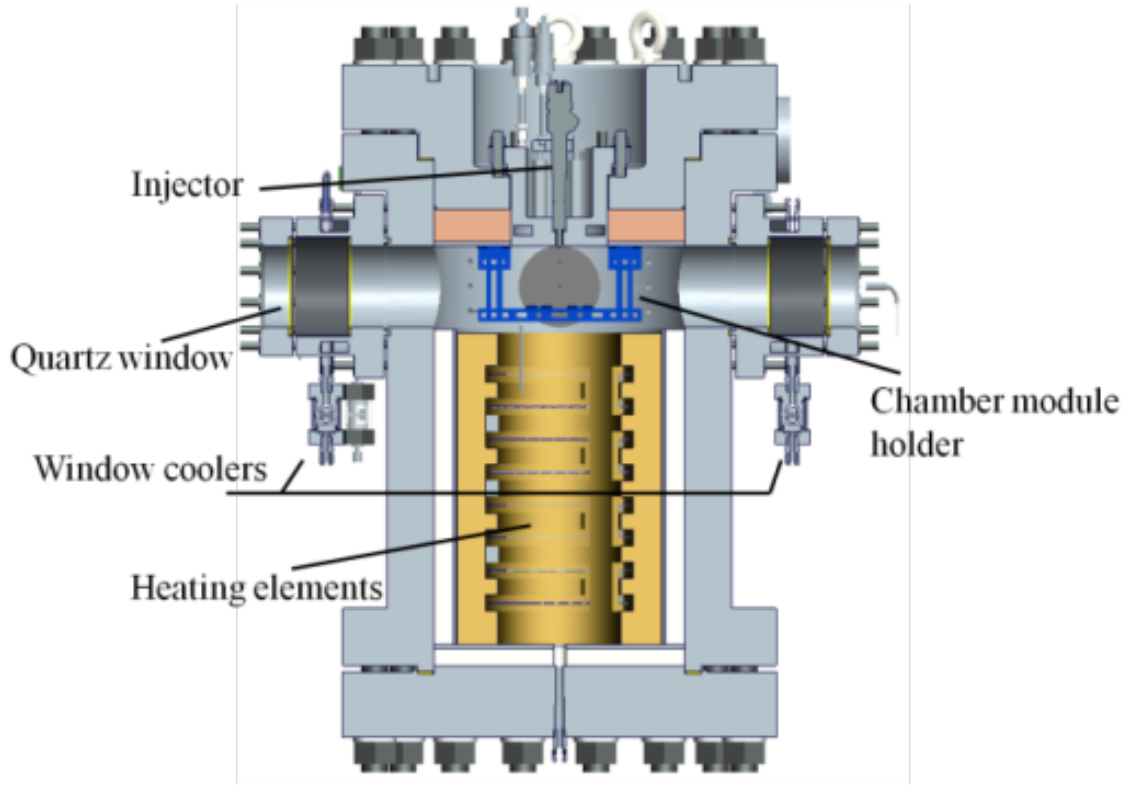


Figure 3.2: Combustion chamber cross section view.

[e.g. Pickett et al., 2009] to accommodate this type of setup without knife edge, since this setup will not induce the Schlieren effect by the knife-cut. Schlieren imaging is a common technique used to visualize fuel jet, the common z-type setup is seen in Kook et al. [2011] for gasoline jet. The arrangement of this focus shadowgraph setup is semi-Z type (Figure 3.4 where balloon 1 is combustion chamber, 2 is stage lamp, 3 is lens, 4 is cameras, 5 is reflective mirror and 6 is xenon lamp) for the reason that the collimated light right after the exit window requires immediate collection because severe beam steering in high pressure and high temperature environment. The collimated light is emphasized in Fig. 3.5 and during the experiment process, no light intervening was found with the backlit shadowgraph method (by switching one source on and off, then do the same to another), suggesting the feasibility of simultaneous measurement. Two Phantom branded high speed cameras are set up to capture the



Figure 3.3: Temperature calibration image showing thermocouple positions.

spray process, at the same speed rate. The speed used for experiment is 34188 fps and 25000 fps. The backlit shadowgraph method is used to monitor the liquid phase of the jet while the focused shadowgraph method is to observe the vapor phase of the jet. The images are 90° rotated relative to each other due to this setup.

To observe the vapour state of the fuel, the Schlieren technique is the most suitable in this case. As a common technique used for fluid mechanics research, the Schlieren technique was originally used to study shock waves with aircraft. Schlieren technique involves the use of collimated light to detect density gradients. The change of refractive index caused by a density gradient will diffract the light passing through it and leave a clear boundary on the edges of the different density regions. Conventional Schlieren techniques used a knife edge to increase the sensitivity on density gradient by blocking some of the deviated light. Pickett et al. [2011] researched into the utilization of a Schlieren setup on diesel sprays, and they concluded that a Schlieren

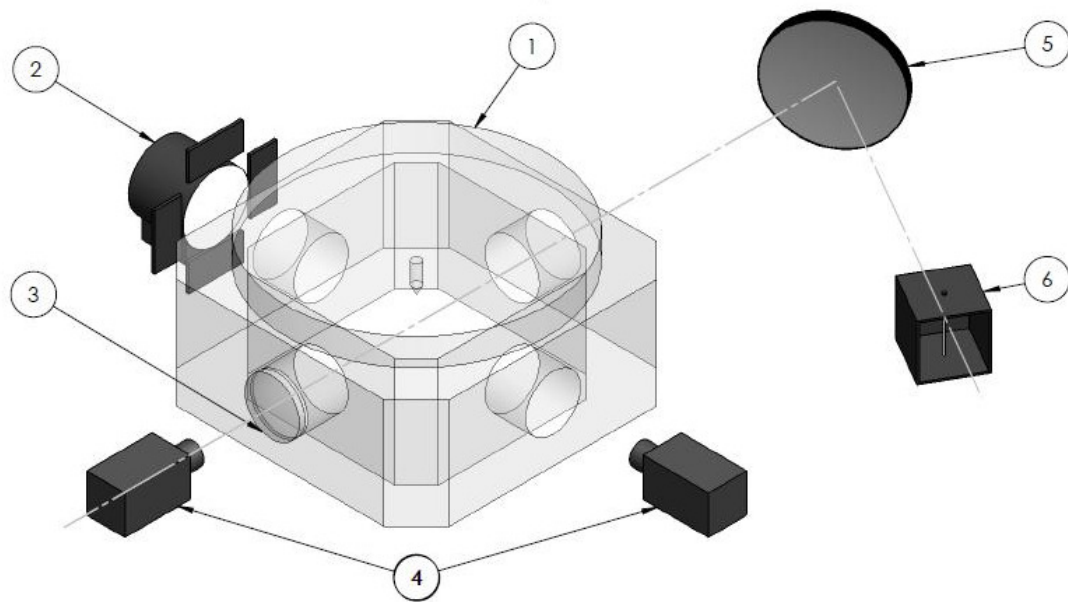


Figure 3.4: Light path setup 1: solid models.

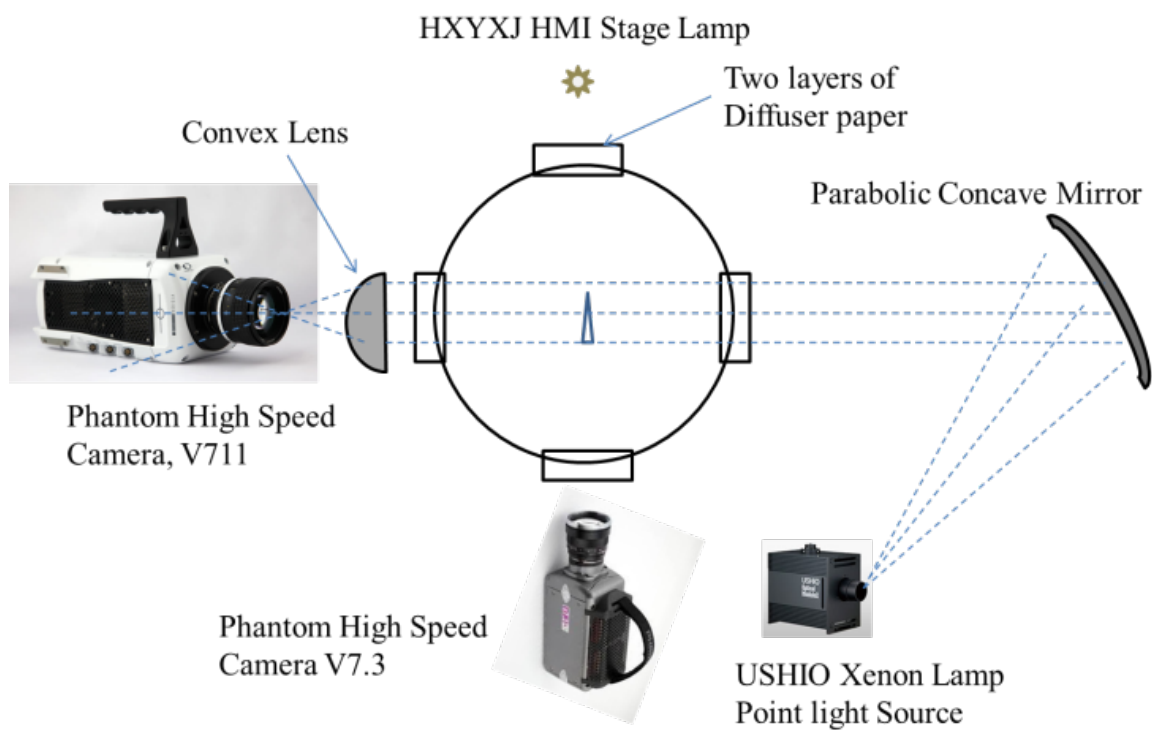


Figure 3.5: Light path setup 2: 2-D model with collimated light path.

setup without a knife edge is sensitive enough for fuel vapour jets, which has much higher density compared with the surrounding ambient gas. Ma et al. [2014] investigated the near-parallel light setup for diesel and gasoline blended fuel as well. In his setup, he was able to detect the liquid and vapour fuel jet in one single image. These studies implied the direct applicability of a Schlieren setup on diesel spray.

In terms of the focused shadowgraph light path arrangement and the apparatus, it is similar with the CMT setup as described in Bardi et al. [2012]. The setup is a semi-z-type configuration as seen in Fig. 3.5. The light going into the vessel is generated by a USHIO xenon lamp and is collimated by a parabolic mirror according to a traditional z-type Schlieren system. The light going out the vessel immediately passes a convex mirror of 100 mm focal distance. Unlike z-type system, this setup is found to be better in terms of image quality. The beam steering caused by the hot environment distorts the collimated light. When the light comes out from the vessel, its travel distance should be minimal to inhibit the distortion from worsening. The distance of travel required by a z-type setup was found to be unacceptable in this experiment. Being focused by the convex mirror, the light is collected by a Phantom v711 camera, with a 60 mm Nikon lens. The exposure time is set to be $17 \mu\text{s}$ and the frame speed is 25000 fps (with 144×552 resolutions) or 34188 fps (with 128×456 resolutions) upon different conditions. At high pressure and high temperature condition, the experimental noise is also high. Higher imaging speed is required to better cancel the noise. The scale of the images is 0.1662 mm/pixel.

The shadowgraph setup is less complex compared to the focused shadowgraph setup, also shown in Fig. 3.5. The lamp used to backlight the liquid jet is an HXYJ Daylight Compact 1200 stage lamp. Before the light enters the vessel from the windows orthogonal to the focused shadowgraph light path, there are two layers of diffusers to turn the light source into a uniform source. The images are collected by a Phantom v7.3 camera with a Nikon 105 mm lens. The exposure is set to $10 \mu\text{s}$, and

the frame speed is 25000 fps (with 112×400 resolution) or 34188 fps (with 112×400 resolution) in synchrony with the focused shadowgraph camera. Both cameras are 12 bit with images recorded to suit the processing algorithm. The scale of images is 0.2395 mm/pixel.

Both of the cameras are supposed to take images at the same instant to achieve simultaneous measurement. However, this is not very practical because differences in camera models and cord lengths. Since the trigger signal arrives at the cameras at a slightly different time, and the signal processing speeds of two cameras are not same (one is a newer model of the same brand) there is a time difference. To mitigate this time difference so as the fuel jet images from the two cameras are almost at the same instant, a signal lag of 400 μs is imposed between the two cameras. This time lag is artificially generated so that the the first images of emanated jet has almost the same length from both of the cameras. The liquid and gas images will always have an error of less than 1 frame, or 40 μs at low speed case and 29 μs in high speed case. It is not saying that the one frame error can be negated by the 400 μs lag, but rather the 400 μs signal lag is only there for experiment conductors to compare the develop trend and help spotting abnormality in the system. Abnormality, such as severe images time gaps, is not found in this experiment.

3.2 Methodology

3.2.1 Detailed Experiment Procedure

The blended fuel is mixed right before the experiments take place. Fuels are stored in a storage room with a temperature lower than 20 °C and properly sealed after every drain. Fuel are mixed on a volumetric basis and fully stirred to avoid separation. The diesel is graded as #0 as provided by the Beijing Institute of Technology Engine Lab, and the gasoline was graded with a research octane number of 93 as per Chinese

national standard. To obtain the physical properties, fuels were sampled and tested by chemical labs. The most recent available data for the fuel properties is included in Table 3.1. Each type of the fuel (G0, G20 and G60) was stored at a specified fuel tank, and the tank was emptied at the end of experiments.

Fuel Type	Diesel	Gasoline
Density @20°C [kg/m ³]	821.4	720.6
Heating Value [MJ/kg]	43.15	43.58
Viscosity @20°C [mm ² /s]	4.615	N/A
Vapor Pressure [kPa]	N/A	58.6
5% Recovery Temperature [°C]	206.5	47.6
95% Recovery Temperature [°C]	357.0	176.3

Table 3.1: Fuel properties.

The injector temperature is not monitored in all experiment runs, but a return fuel temperature range is determined between 37 °C to 69 °C as the system is on for the time of experiment running. Generally, the temperature is lower at low injection pressure. The injection rate (mass of fuel per shot) of different types of fuel is estimated by the scaling method. An injection rate v.s. time curve can only be obtained from the pure diesel fuel since the machine is not designed to be used on gasoline, which may damage the seals. Using the method that just scales the mass of the injected fuel, it is observed that the volumetric injection rate is almost constant over the three types of blended fuel.

When the experiment begins, the fuel circulates within the injection pipes and gives 100 injections in order to clear the residue of the previous fuel. The experiments are conducted through altering the chamber parameter, namely the injection pressure, chamber temperature and background gas density. The parameter ranges are shown in Table 3.2. The pure diesel tests are also useful when comparing with literature results. Gasoline fraction of 20% and 60% are the low and high fraction levels used to blend with diesel. In fact, further increasing the gasoline blending ratio will create stress

on the fuel supply pump due to the lack of lubricity with gasoline. Other parameters (background density, temperature and injection pressure) are divided from low to high, in order to obtain 7 levels of measurements as is shown. This is a typical multi-level design of experiment. A complete measurement map will consist 7 levels for 3 independent variables \times 3 repetitions \times 3 fuels, which results in 3087 injection events. The huge amount of tests could waste a lot of time and resources. To focus on the research goal, which is investigating the sprays at an engine environment, simplified design is adapted in this study. Knowing the maximum conditions obtainable for the system to be [140 MPa, 850 K, 22 kg/m³], the experiment is conducted based on this origin and equally step down 7 measurement points. For a complete table of measurement Table 3.2 is shown. The kind of simplification is widely adapted since the studies focus in on high pressure and high temperature environment [e.g. Naber and Siebers, 1996; Pickett et al., 2011; Kook and Pickett, 2012; Ma et al., 2014]. After the simplification, a total of 7 levels \times 3 independent variables \times 3 repetitions \times 3 fuels, or 189 injection events were conducted. The maximum condition is chosen because this condition is close to a true low temperature combustion injection timing (e.g. 11° crank angle before TDC [Musculus et al., 2013]).

Parameter	Range
Gasoline %	0, 20, 60
Injection Pressure [MPa]	80,90,100,110,120,130,140
Chamber Temperature [K]	300,350,450,550,650,750,850
Background Gas Density [kg/m ³]	10,12,14,16,18,20,22

Table 3.2: Independent variables.

3.2.2 Processing Computation Scheme

Imaging processing scheme is done separately on the liquid and vaporized jets. The vapor jet is processed using the schlieren code developed by the Sandia National

Lab, from the U.S [Sandia, 2011]. The basic but robust program gives relatively easy process for this kind of problem, and to access the vital characters of the spray. The definition of the spray penetration and spray angle follows the definition given in Naber and Siebers [1996]. The liquid jet background is relatively clear compared with the schlieren images. It is easier to assess the jet with known algorithm which is widely accepted. A Matlab based program is developed to extract to contour using full width half max (FWHM) threshold method. The scheme is presented as flow chart in Fig 3.6.

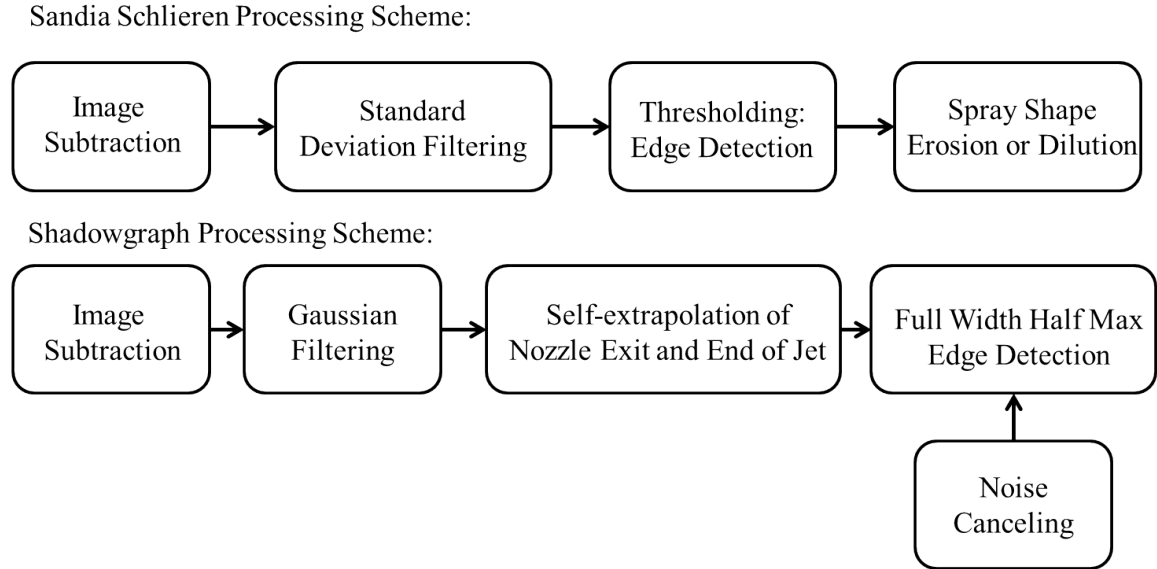


Figure 3.6: Flow chart of the processing schemes.

The image processing algorithm is adapted from the Sandia engine combustion network. Their code is developed specifically for high temperature and high pressure focused shadowgraph. The background noise canceling approach used is by frame subtraction since the noise is near stationary in the high speed video. To be specific, the current processing frame is subtracted by the previous image to get an intensity image. The boundary detection method is the standard deviation filtering option as provided inside the Matlab program, which is programmed to find the texture differ-

ence between the jet and its surroundings. The code input function is reprogrammed for the use of detection of color images from Phantom cameras. The pixel intensities of the images are directly read from the camera sensor through this modification. As is known, color cameras have a layer of red, green and blue (RGB) filters immediately covering the sensors. When the sensor values are read, it can be observed that some pixels are darker than their neighbours, so the images appear to pixelate. This is due to the RGB filters and the quantum efficiency (QE) of the sensors. Since the xenon lamp has a wavelength spectrum close to sunlight, its luminance intensity peaks at the green wavelength. The QE of most camera sensors peaks at the green wavelength as well. Therefore, it is deduced that a brighter pixels observed are covered by green filters. It is known that a pixelated image may increase measurement error for the program, but after frame subtraction applied, the pixelation vanishes and the jet boundary is clear for detection by observation. Therefore, the raw images from a color camera can be used for the program. Other than the Sandia group, Ma et al. [2015] used a modified algorithm of a similar kind to improve the automation and accuracy for detecting the vapour boundary. In order to maintain the accuracy of vapour boundary detection, the Sandia Schlieren code required input parameter adjustments (grids, threshold, erode, dilate and etc.) on poor quality images to obtain consistency as it is seen. The option of “free hand drawing” is used to estimate the boundary of the first image, as it is visualized by subtraction of frames but not detected with the algorithm, or used when the detection algorithm fails. With higher imaging speed in the future, the background noise shall no longer be an issue for diesel jet studies. It may be worthy to mention that the jet head contour usually includes some extra area that does not belong to the jet, it is suspected that the fast moving jet severely compresses the nearby fluid and the density change is captured by the collimated light. This issue also shows in Ma et al. [2015]. Sample image of the processor is shown in Fig. 3.7.

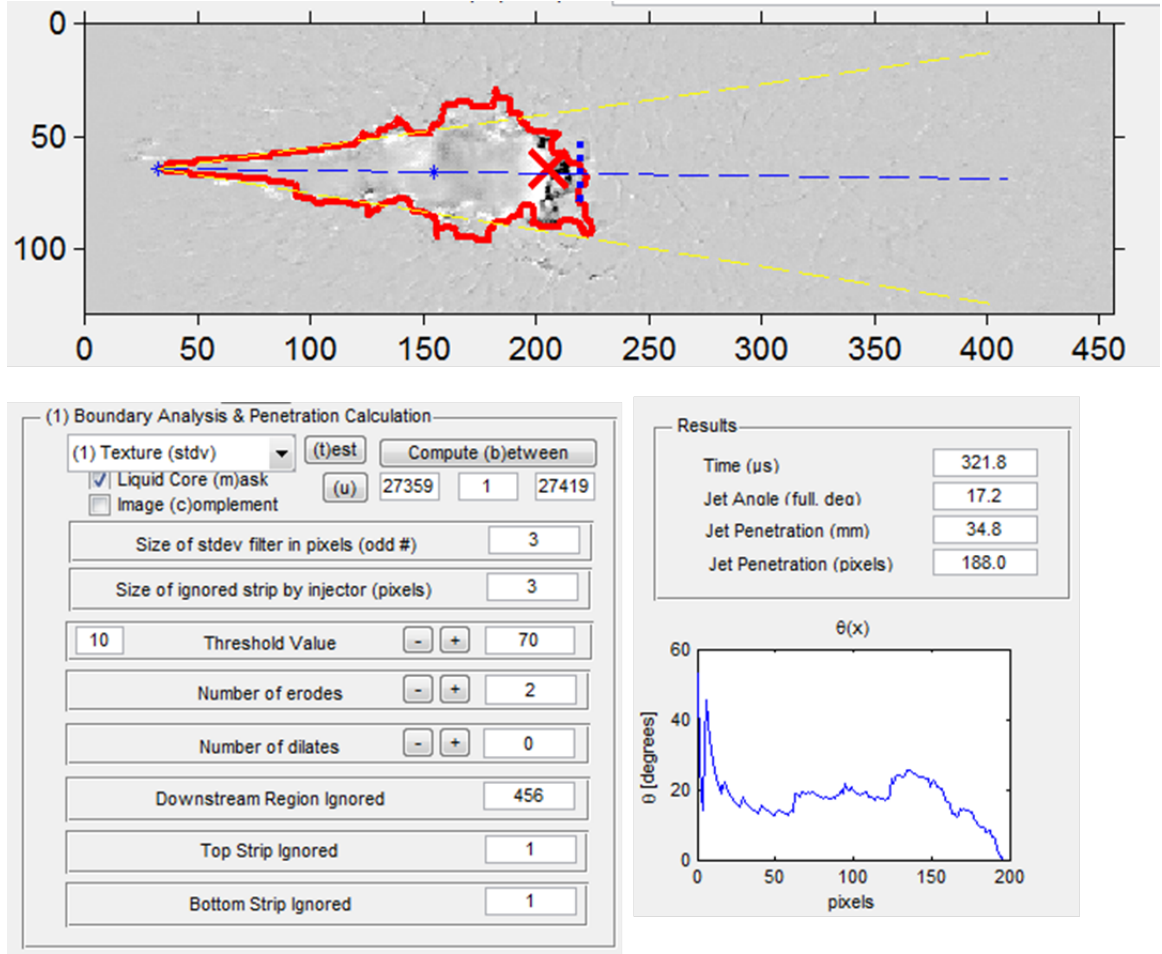


Figure 3.7: Sample image of processing gas jet.

The processing of the liquid jet utilizes the image binarizing technique based on FWHM. Color images are also read directly from the sensor as well, and bright points are observed just like the gas jet images. The background subtraction approach is slightly different from the previous algorithm. The first frame (the frame before fuel jet emanated) is always used as the background, leaving the pure jet plume in the image. A Gaussian filter of size 5×5 is included to further suppress the noise. Even though the filter might decrease the sharpness of images, the final contours of jet show no change by applying this filter. Unlike the Sandia Schlieren code, this liquid jet detection code is designed to be fully automatic, thanks to the more robust algorithms available. The position of the nozzle tip and the end of the jet

is determined by comparing with the residual background noise. The signal-to-noise ratio is set to be 3 in this case. Upon knowing the jet range, the code is able to determine the jet width by a FWHM algorithm. The algorithm compares the grey-scale level of the jet with its background at a single line of pixels. The pixels with brightness value higher than 50% of the maximum are considered as the jet. Through line-by-line scanning, the contour of the jet is drawn. To ensure this plotted shape is reasonable, the jet contour is compared with the Canny edge detection method, and the threshold with Otsu's technique. Results are shown with good agreement by sight. The example processed result is shown in the upper image of Fig. 3.8. The example of determining the FWHM of jet is shown in the 2nd image of Fig. 3.8. The code is broken into 5 function blocks which can be found in the Appendix B.

For the matter of measuring the jet parameters (jet angles, penetration), the Sandia code embedded algorithm is utilized since it is already in place. Although in the literature they claim that the code implemented the concept by Siebers [1999], it is slightly different than what is described in that paper. The actual equation used in the spray angle counts half of the jet and assumes axis-symmetry. The equation is shown below,

$$\frac{\theta}{2} = \tan^{-1} \frac{A_x}{(0.5b)^2} \quad (3.2.1)$$

where b is jet length (assume as penetration) and A_x is the area of jet from the upstream half. Since penetration would not be known at the first calculation, an initial b would be given by the processing scheme. To further define the penetration length, a triangle with half of the spray angle is plotted as seen in Fig. 2.4.



Figure 3.8: Sample image of processing liquid jet (top to bottom: subtracted Image, detected Contour, Canny edge detection contour).

3.3 Uncertainty

This section serves as an evaluation of the current setup and the validation of results, rather than quantifying the effect of error from each parameter to the final output uncertainty. The reason for not performing a complete analysis is because of the lack

of an analytical model to explain how the independent variables affect the final jet penetration, jet angle and jet area. Some parameters, such as nozzle diameter, are not included in this study because of the complicity in quantifying the nozzle geometry. In fact, few researchers in the literature emphasized a focus on the experimental error because experimenters lack comprehensive control of every parameter. For this reason, the uncertainty analysis in this thesis focuses on providing a validation of the experimental setup.

3.3.1 Instrumental Uncertainty

Many instruments are used in this experiment, including the thermocouple, pressure transducers and caliper. The quantifiable errors are shown for the measured conditions in the following paragraphs.

For the thermocouple, test data in Appendix D have shown that the wall measurements deviates a maximum of 63 K from the centerline measurements (see Table D.2), which is 7% difference from the reading value. The temperature difference is high at 63 °C when the chamber background density is low and the chamber temperature is high. The maximum temperature difference occurs at the thermocouple close to the heater side as expected. The resolution of the thermocouple is 1 °C in the digital panel. During the experimental procedure, the turbulent heat flow is circling through the chamber, and the wall temperature is impossible to stabilize. However, the heat transfer analysis is out of scope of this thesis. Therefore, a reading of the temperature is taken for a simultaneous output. The experimental standard deviation is found to be 1.67%, i.e. if the chamber temperature is reported as 850 K, the centerline temperature can be $850 \text{ K} + 14 \text{ K}$. The detailed measurement record can be found in Appendix D.

It is more difficult to determine the background density as it is not a directly observed value. The background density is obtained from the ideal gas law,

$$\rho = \frac{P_{ch}M_{N_2}}{R_{gas}T_{ch}} \quad (3.3.1)$$

Where $M_{N_2} = 28.02$ g/mol for nitrogen and $R_{gas}=8.314$ J/K-mol as the universal gas constant. For this kind of parameter, uncertainties can be estimated from propagation of parameter uncertainties. However, the pressure measurement uncertainty is determined to negligible, since it does not fluctuate in the control panel, and there is no calibration target. The pressure transducer used in the chamber is the model P30 manufactured by Endress+Hauser. Repeatability of pressure control is not known therefore uncertainty propagation is abandoned. The calculated background density data in Table A.1 and Table A.2 is used to estimated the uncertainty. The mean of background density for the 45 cases with 22 kg/m³ nominal pressure is 22.23 kg/m³, and the maximum deviation from mean is 0.87 kg/m³. Standard deviation of the records is 0.36 kg/m³, leading to a ± 0.73 kg/m³ 95% confidential interval (two-tail). Therefore, the interval is calculated as [21.50 kg/m³, 22.96 kg/m³]. The reporting value, a background density of 22 kg/m³ is basically accurate laying within the 95% confidential interval.

The injection pressure fluctuation curves were not recorded by the software system. The errors are only estimated from the monitoring screen. The stabilized pressure was not observed to fluctuate a lot, except the G60 case. A high percentage of gasoline blended diesel fuel causes the high pressure pump to work with more pulsation. The injection pressure will fluctuate approximately ± 4 MPa, from the monitor screen.

Visualization experiments usually involve a conversion process which converts the pixel space into physical space. The calibration is done with a calibration target, which feature two holes with a known distance. Since the conversion factor is critical in further programming, it is measured at each day of experiments. The repeated measurement results are shown in Table 3.3. The average scales are determined to

be 0.2395 mm/px for the shadowgraph setup and 0.1662 mm/px for the focused shadowgraph setup. Since there is only four measurements, the confidential interval method is not used here. The uncertainties are root mean square (rms) summed with the physical distance uncertainty and the repeatability uncertainty, which is found to be 0.0251 mm/px for shadowgraph and 0.01462 mm/px for the focused shadowgraph setup. Both of the uncertainties are close to 10%.

Physical Distance (mm)	4.87	Uncertainty (mm)	0.4	
	Shadow	Uncertainty	Schlieren	Uncertainty
Trial 1	0.2532	0.0210	0.1679	0.0140
Trial 2	0.2423	0.0200	0.1675	0.0140
Trial 3	0.2309	0.0190	0.1620	0.0130
Trial 4	0.2316	0.0190	0.1675	0.0140

Table 3.3: Scale factor uncertainties.

Programming software error can be discussed in the context of instrument uncertainty as it is one of the important elements that contributes to the final value uncertainty. Unlike the experimental instruments, which affect the final output through a set of unknown mechanism, the post-processing software directly affects the outputs, therefore it is most-worthy to discuss.

The discretization error is one of the most common errors in computer processing. The discretization error for a liquid jet penetration is estimated to be 1 pixel. It is also worthy to mention that the subtraction of vapor jet images still give a high amount of residual noise in the background, implying that the jet penetration uncertainty does not simply includes the discretization error, e.g. light refraction and scale factor uncertainty. It is unknown how much the noise affects the measurement results, which makes the quantitative discussion difficult for the vapor jet. It is possible that as the imaging frame speed rise in the future, the background will be cleaned up and uncertainty is reduced.

For the liquid images, the background is easier to be cleaned up; an example is

shown in Fig. 3.9. Again, big pixels are seen in the images because the cameras used are color cameras, the RGB filters create this pixelation but the effect is completely canceled by the background subtraction.

The quantification of the discretization of the jet area is difficult due to the irregularity of shapes. Ghaemi [2009] gives a detailed analysis on this subject. Figure 5-1 of Ghaemi [2009] illustrates the discretization error with a spherical area. The error of area can be significantly reduced with the increase of imaging resolution. Therefore, the highest error usually comes from the vaporizing liquid jet because the jet area is relatively small and includes much fewer pixels. The discussion of the area discretization error is different from Ghaemi [2009] who used 4-connection or 8-connection boundary detection method. The boundary detection used in this problem is FWHM for the liquid jet and the threshold method by the Sandia group for vapor jet images. In the FWHM method, the jet boundary is not necessarily continuous for the boundary, as can be seen in Fig. 3.8. The boundary is scanned for each column of pixels in the images. Therefore the evaluation of uncertainty relies on the number of columns containing the liquid jet, or the detected jet length. The uncertainties for vapor jet detections cannot be quantified due to manual adjustment “Erode/dilate” function used.

The last parameter to be discussed is the signal to noise ratio (SNR) in the liquid jet processing. This parameter is required to estimate the end column. An SNR of 3 is used in this study to compare the light signal strength to the background signal strength. This end processing column of pixels is not used to determine the jet penetration, which is measured according to the definition in the previous section. The uncertainties of detection is minimized as long as the entire jet is covered. The SNR value in this program is aimed to minimize experimental error.

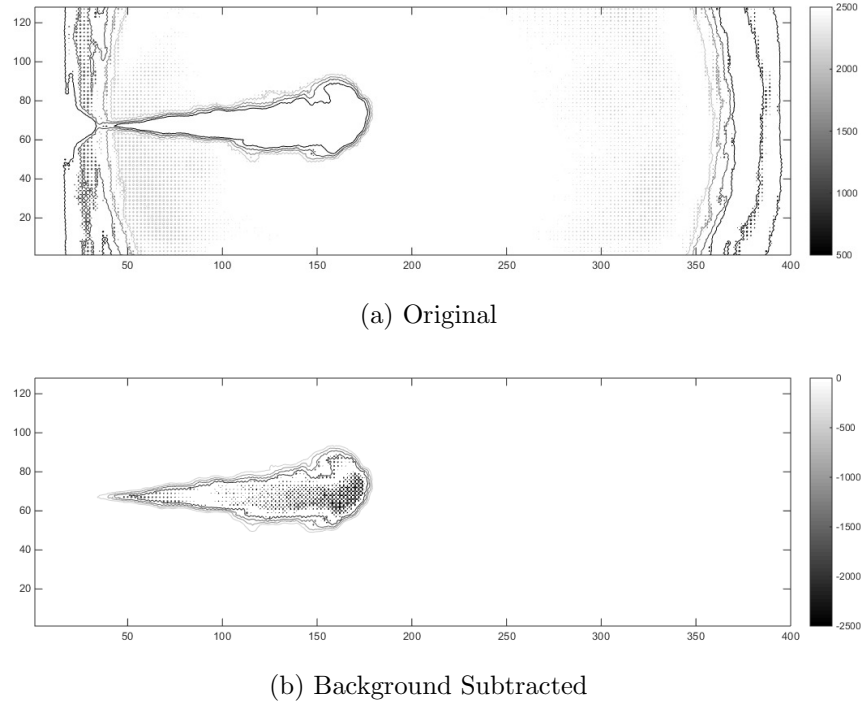


Figure 3.9: Noisy background subtraction results.

3.3.2 Repeatability of the Output

Usually experiment uncertainty is analyzed for a large amount of repeated tests according to the statistic t-test. The comparison of this experiment was not performed with every set of data due to the large amount of data acquired. However, comparisons were done at the highest chamber condition [850 K, 22 kg/m³, 140 MPa], at which point 9 repeated tests are available.

The detailed variation test can be found with Fig. 3.10 for the G60 case, where the liquid and vapor jet plots over the 3 injection events are compared. As can be seen, the variation between a single run is small, and the curves are similar. Fluctuations of the area plots are higher compared to the penetration curves. This deviation could be from the violation of axisymmetric assumption. High Reynolds number jets are in the turbulent regime, therefore perfect symmetry is not expected, while the penetration parameter is not restricted to the axisymmetric assumption. In summary, the single

run repetition shows good consistency as the jet grows.

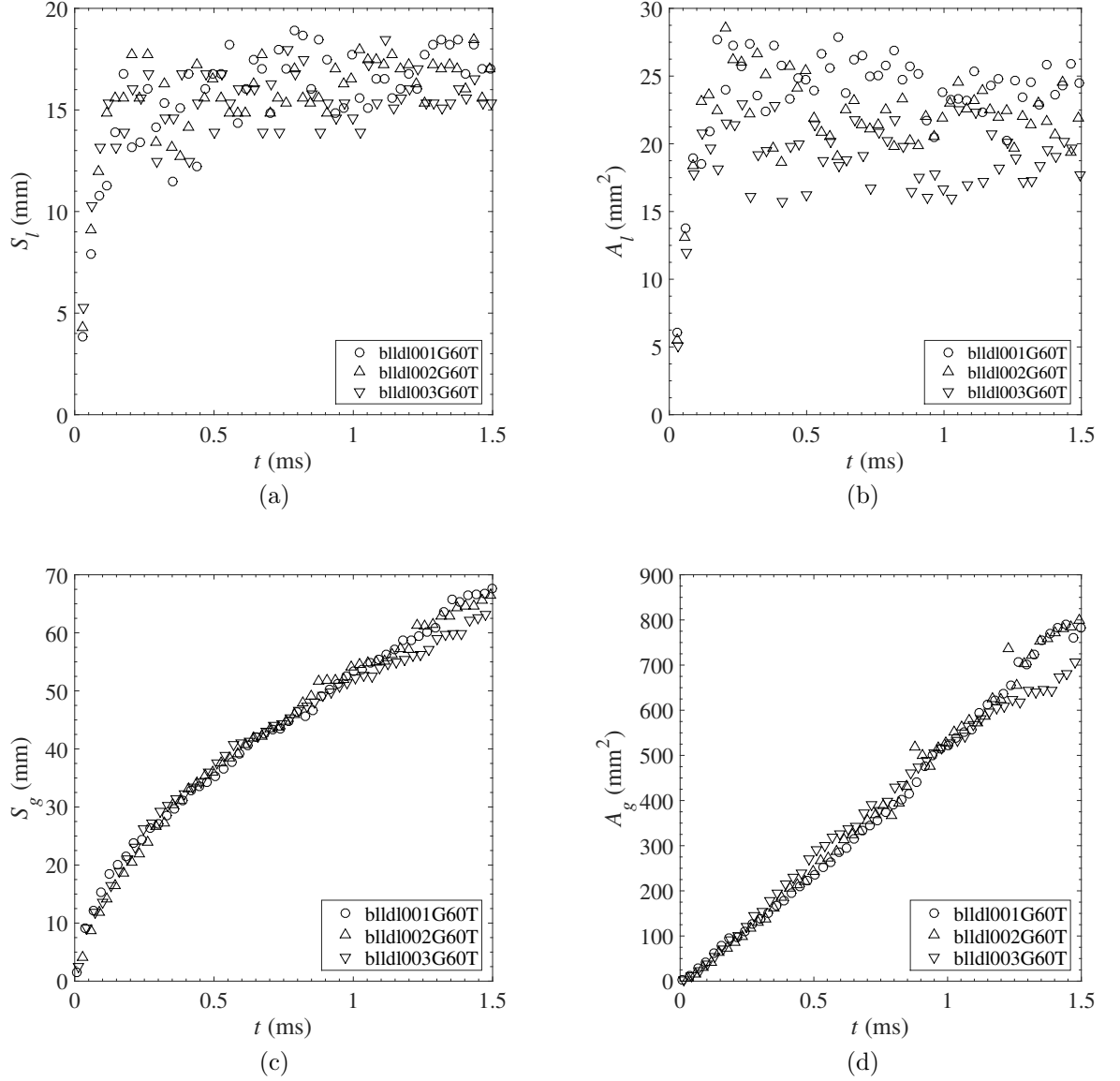


Figure 3.10: Variations on a single run on jet penetrations and jet areas, with $\rho_{ch} = 22 \text{ kg/m}^3$, $T_{ch} = 850 \text{ K}$ and $P_{inj} = 140 \text{ MPa}$, G60 fuel temperature variation run.

The repetition tests for the experimental origin [850 K, 22 kg/m³, 140 MPa] are shown in the Fig. 3.11 for the G20 and G60 case. The comparison is done to compare the different ways of reaching the highest operation condition, showing how well the

conditions are controlled and if the setup can repeat the results between realizations. The jet penetration is used as the comparison output parameter, as it is not affected by the axisymmetric assumption. The graphs show that the consistency is obtained well with the G20 case for the liquid and vapor jet penetration. For the G60 case, the jet fluctuation is high. The consistency obtained from the vapor jet penetration implies the experimental conditions are acceptable. At this stage, it can be concluded that at 60% gasoline blended fuel there is stress on the current pumping system, preventing the possibility of increasing the blending ratio. This could be because at this blending ratio a low viscosity mixture is obtained. The repeatability of the system is concluded to be acceptable from these graphs.

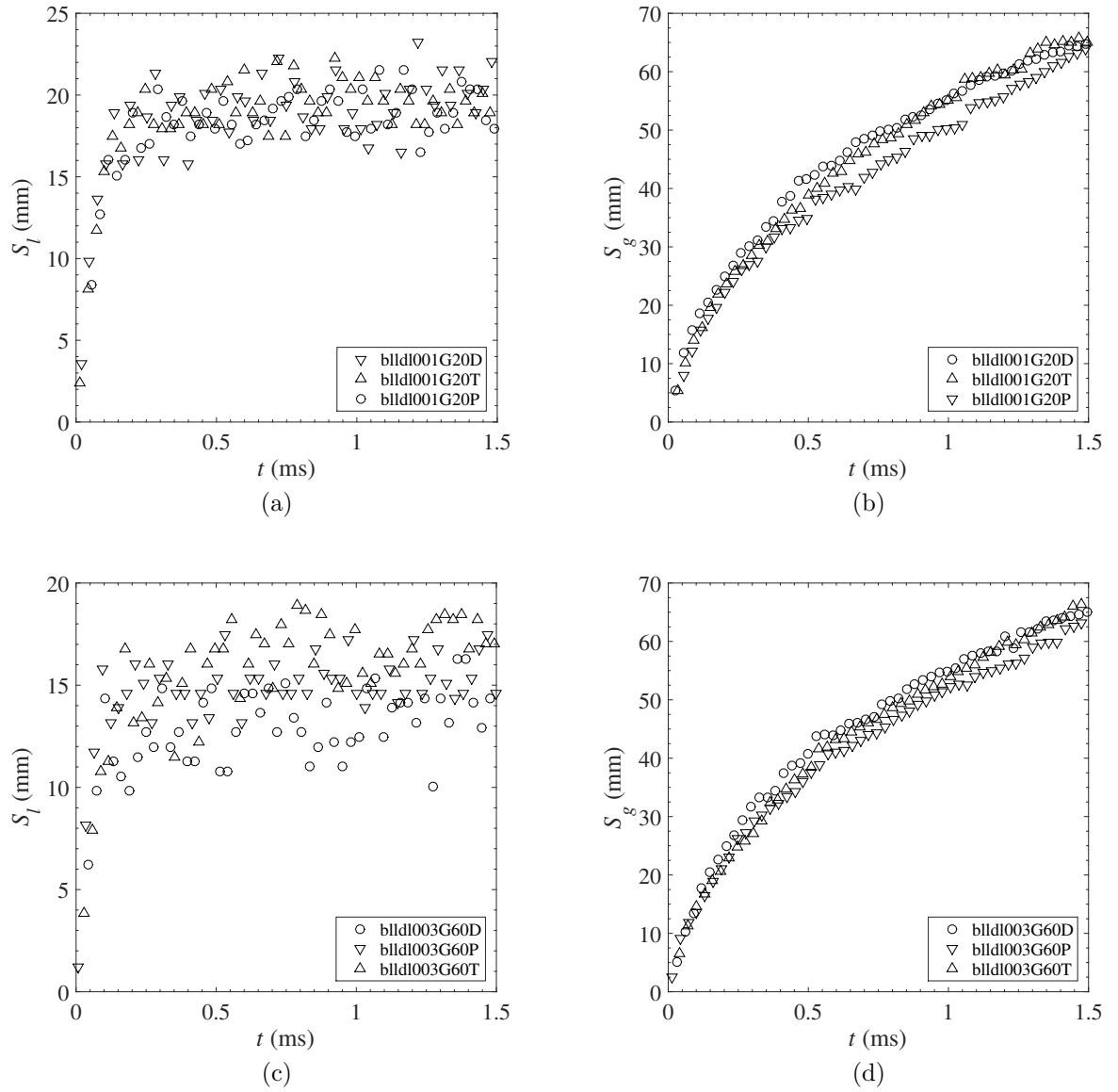


Figure 3.11: Repetition tests result for G20 and G60 diesel fuel jet penetrations, with $\rho_{ch} = 22 \text{ kg/m}^3$, $T_{ch} = 850 \text{ K}$ and $P_{inj} = 140 \text{ MPa}$.

CHAPTER 4

RESULTS

An overview of experimental spray visualization results and spray morphology are given in this chapter. First focused shadowgraph and shadowgraph results are described and shown, and then spray metrics such as jet penetration and jet area as a function of time are plotted. A vaporizing jet is compared to a non-vaporizing jet and a discussion of jet edge detection follows. Three Dieseline fuels (G0, G20 and G60) are visually compared to examine the effect of fuel type on the spray. For both gas and liquid jets the effect of background density, chamber temperature and injection pressure are examined. The purpose of this chapter is to provide an overview of the extensive amount of experimental data by presenting a small number of representative examples that illustrate the key features. The complete listing of experiments conducted in this thesis is summarized in Table A.1 and Table A.2 in Appendix A, and totally consists of 63 runs. A more detailed comparison, including cross-examination of the liquid and vapor jet data follows in Chapter 5. As discussed in Chapter 3, observations after 1.5 ms are not used due to the growing image processing error.

4.1 Visualization Results

The fuel jet is visualized using the optical techniques described in Chapter 3 with two sets of simultaneous images taken to examine both the liquid and vapor state

of the fuel jet. The word “simultaneous” means the two images shown in Fig. 4.1 are taken from two different cameras at almost the same time. As it is discussed in Chapter 3, the simultaneous measurement always have one frame of error (or misalignment), therefore plotting the data in curves is preferred over using the raw image data. Room temperature (300 K) focused shadowgraph and shadowgraph results are both shown in Fig. 4.2 for a non-vaporizing jet. This is a case with injection pressure of $P_{inj} = 140$ MPa and $T_{ch} = 300$ K, and G20 fuel (case bvldlG20 in Table A.1) with this example image taken 0.96 ms (24 frames) after the first frame of injection. It is difficult to discern the fuel jet trend visually, partially because the images have a different scale and resolution, so the images are processed. A comparison of the fuel jet penetration S and jet area A (S & A definition see Chapter 1) for the vapor and liquid jet are shown in Fig. 4.2. In the figure, the jet penetration between the vapor and liquid jet matches closely while the area plot of the vapor and liquid jet only matches at the beginning (up to 0.3 ms). One possible explanation is that for the vapor jet case, the non-liquid element, namely the vaporization of the jet, is not easily seen. This reasoning is a possible explanation for the difference found in jet area between the two curves in Fig. 4.2b. Another possible explanation is that, if the jet is not axisymmetric, an error would occur since the images are on orthogonal planes. This, however, is unlikely as the liquid jet area is always higher than the vapor jet plot at room temperature. Yet another possible reason could be the processing scheme where the vapor jet processing standard is less well defined (described in chapter 3) compared with the liquid jet processing scheme (described in section 2.1 and which always centered on the FWHM threshold). Specifically, the vapor jet processing code must be tailored for each frame of a jet video which could result in a higher tolerance when determining the width of the jet, which in turn increases the jet area. The code must be tailored to take into account the distortion from the compressed background; however at room temperature, little ambient distraction is

seen in the background of the images. Thus both schemes should show relatively close S and A , up to $t = 0.3$ ms. For later time $t > 0.3$ ms perhaps the discrepancy in jet area A indicates that some fuel is vaporizing, which is not captured in Fig. 4.2. One conclusion from Fig. 4.2 is that jet penetration is a more robust parameter than area for use in jet flow prediction. Compared to the jet penetration, the jet area seems to provide less information about the jet, perhaps since the jet is not a solid body. Instead, filled with drops and entrained gas, the jet area merely represents the jet dispersion as discussed in the literature and summarized in Chapter 2. However, when investigating the fuel vaporization, the jet area is found to be a better parameter than jet penetration for the experimental results collected in this study.

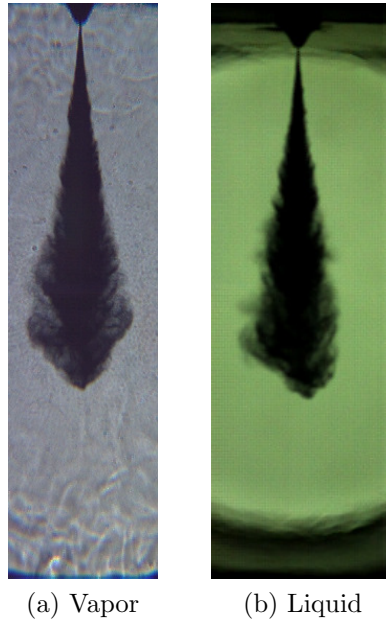


Figure 4.1: G20 (a) Fuel focused shadowgraph and (b) shadowgraph results, with $P_{inj} = 140$ MPa, $T_{ch} = 300$ K, $t = 0.96$ ms (24th frame), case bvldl001G20 in Appendix A.

As is seen in Fig. 4.3, the area ratio of the liquid jet area divided by the vapor jet area is shown for the three different fuels. The area ratio is kept around 0.8 at low temperature conditions (< 450 K), indicating there is unseen evaporation. The area

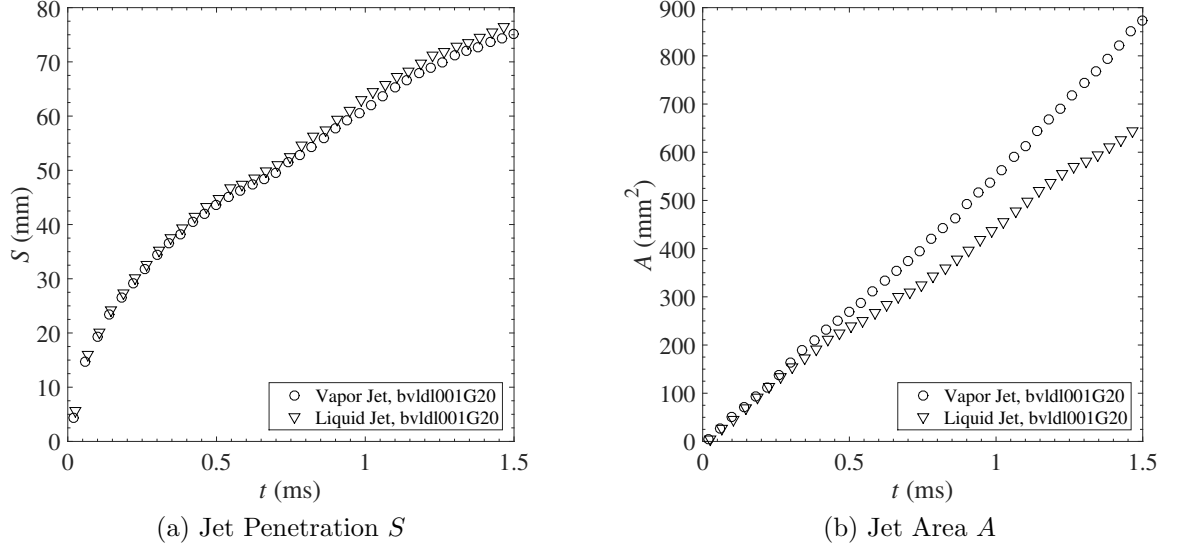


Figure 4.2: Fuel jet time evolution for case buldlG20 – shown in Fig. 4.1.

ratio starts to show declining slopes at 550 K and 650 K, indicating significant evaporation. At this stage, it can only be deduced from these graphs that the evaporation starts at 550 K for all fuel blends.

In contrast to what is seen in Fig. 4.1a, the vaporizing jet image in Fig. 4.4a shows a complex background structure compared to Fig. 4.1a. The difference between Fig. 4.4a and Fig. 4.1a is the temperature $T_{ch}=850$ K and $T_{ch}=300$ K, respectively. The nozzle is also harder to identify in both images of Fig. 4.4 compared to Fig. 4.1. The first image of injection is used to approximate the nozzle position for the vapor jet image. The complex background structure creates a high disturbance background for the image processing and is a major reason for not using the knife-edge in the Schlieren-like system. Since the background consists of clean bright edges that imply high density gradient, using a knife-edge to boost the sensitivity of the Schlieren-like setup is not necessary, and may impair the image quality for post-processing. The background structure is attributed to turbulent heat convection from the bottom of the chamber where high temperature gas circulates inside the chamber creating eddies

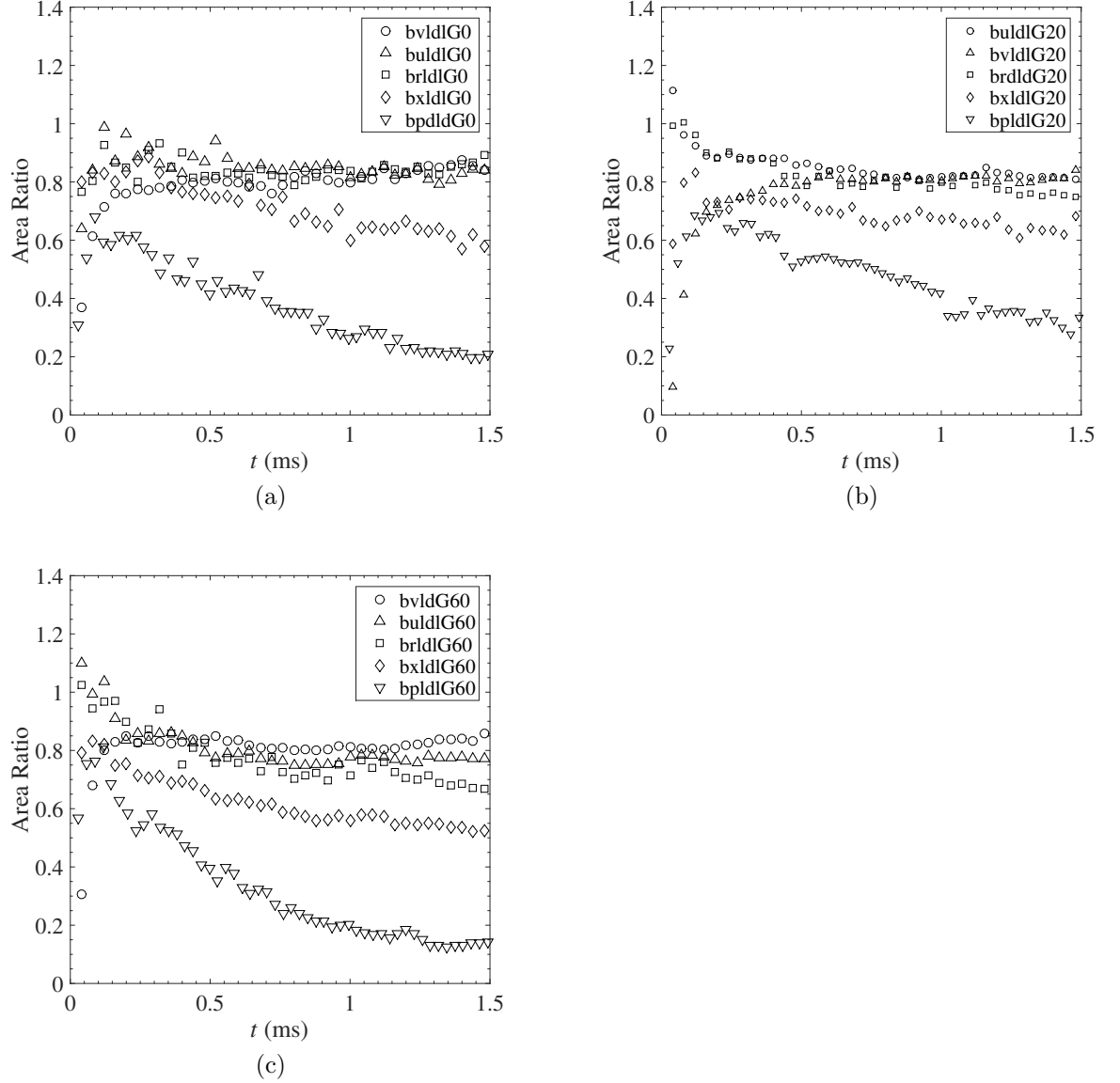


Figure 4.3: Jet area ratio (liquid jet area: vapor jet area) with $T_{ch} = 300$ K, 350 K, 450 K, 550 K and 650 K, $P_{inj} = 140$ MPa, $\rho_{ch} = 22$ kg/m³, cases are defined in Table A.1 and Table A.2.

in density. The turbulent flow inside the chamber also affects the collimated light path, i.e. steering the light significantly from its original direction. For this reason, a Z-type Schlieren setup is not used because of the light loss after the chamber. Instead, a convex lens is placed immediately after the chamber to collect all the light, creating

a semi-Z-type Schlieren setup similar to what is seen with Bardi et al. [2012]. A drawback of this semi-Z setup is the effect known as coma in photography [Settles, 2001] due to asymmetry of the setup which can create a shadow. In these results, heavy shadowing of the fuel jet is not observed, meaning coma is not problematic. Light deflection due to the convex lens is another issue with this method. Using Xenon lamps as the light sources, a natural white light spectrum is expected. When white light passes through the convex lens, it refracts depending on the wavelength, while a surface coated mirror will not refract light. Although a large refraction can significantly distort the image, the vapor jet image only shows small deflection around the bright disturbance edges, as is seen in Fig. 4.5. The arrows shows small red, green and blue (RGB) pixels which is artificially generated by light deflection. The pixels are clustered in the neighbourhood indicating deflection is not severe. The deflection only affects measurement of fine detail (2×2 resolution pixels) in the jet boundary, which is not discussed in this thesis. Compared to the light loss using Z-type Schlieren (which leads to a blurry image), the setup is deemed to be most suitable to investigate this kind of background.

For all cases tested, the jet image characteristics are almost the same for the three fuels tested. The images can be divided into three regions according to the texture. The first region is the outside background gas complex structure. The second region is the jet main structure where high speed flow is visualized as a plume. The third region is the jet boundary near-stationary region. The jet boundary is clearly seen due to the near-stationary diffused fuel suspending on the jet. The three region structure is also clearly visualized in Fig. 4.5. The first and second region is easily recognized in the left image of 4.5. However, after $176 \mu s$, the side-burst portion of fuel becomes stationary and remains in the same position of the image. The texture of this portion changes to become more transparent and close to the background color. Due to the high density of fuel, light refraction is severe and the pixels are showing strong RGB

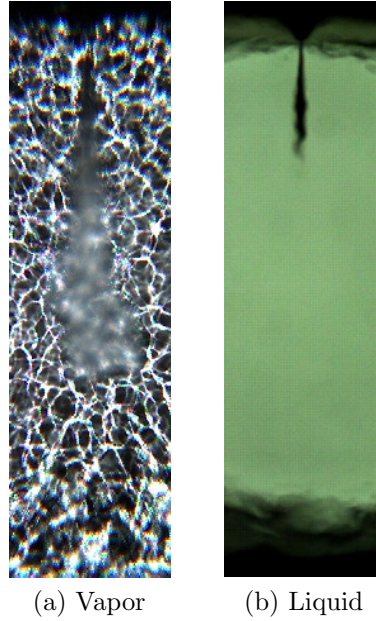


Figure 4.4: G20 fuel focused shadowgraph and shadowgraph results with $P_{inj} = 140$ MPa, $T_{ch} = 850$ K, $\rho_{ch} = 22$ kg/m³, $t = 0.96$ ms (24th frame), case blldl001G20T.

patterns as explained above. Thus, the boundaries become easy to identify because of the convex lens and the color camera used. When conducting the image processing, only greyscale images are used and this layer is less obvious. The current technique cannot distinguish the three regions and therefore the side burst of the jet is not included in the statistics counted. For the future study, it would be interesting to know if the side-burst of the fuel jet occurs more often when higher ratios of gasoline are blended. In the current study, it is only known that side-bursts happen from time to time in different positions of the jet, and the three-layer structure makes the vapor jet processing scheme less responsive and difficult to define the jet boundary.

To eliminate most of the complex background, frame subtraction is used in post processing [Naber and Siebers, 1996]. The process is done by subtracting the current image with one previous image (denoted as $I_i - I_{i-1}$). The reason for not performing image subtraction such as $I_i - I_{i-2}$ is because this artificially lowers the frame speed

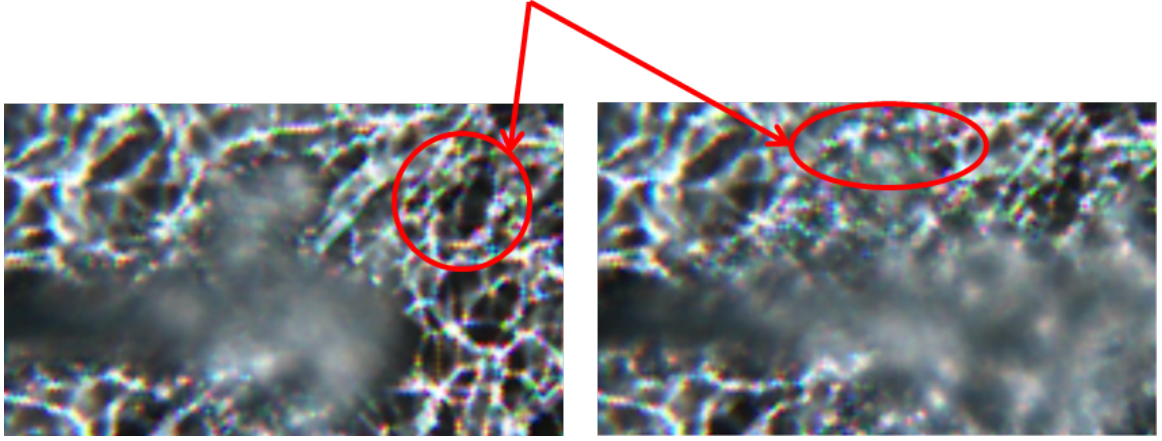


Figure 4.5: Jet Detail with a $T_{ch} = 750$ K Jet of G60 Fuel (run#1), Showing Jet Side Burst Effect, frame #18 (Left) and #24 (Right), Time difference is $176 \mu s$, Case bnldl001G60.

by one half. High frame rate is desired because it gives more velocity field details, and it makes the slower moving background structure seem stationary. An optimal frame rate requires knowledge about the life span of a background structure, which is out of the scope of this thesis. Therefore, $I_i - I_{i-1}$ is determined to be the best for this experiment.

The example frame subtraction images are shown in Fig. 4.6, which is the complete video (every third frame) for Fig. 4.5. The subtraction is based on the speed differences of the background structure and the jet itself. The background structure is observed to have little movement over subsequent image frames but the high speed jet moves rapidly as is seen Fig. 4.5. The boundary of the jet is seen usually in the bottom half of the jet ($> 0.5S$), indicating the boundary remains relatively unchanged in the beginning section of the jet. The side burst is clearly seen from frame# 18 to frame# 24. The residue of the side-burst fuel persist to frame# 33 but with weaker contrast. As time progresses, the jet edge becomes clearer and so it is easier to detect by the algorithm. For this reason, the program to find the jet boundary is as follows:

- Current frame is subtracted from the previous frame to reduce background

noise.

- Using contrast, the algorithm starts searching for jet boundaries from the designated nozzle position. The contrast threshold may vary from frame to frame to obtain a match of jet contour.
- In the near field, no boundary can be detected due to the weak contrast after frame subtraction, so contours are found further downstream.
- The weak boundary in the downstream region may be difficult to find or conversely may dominate, so the jet contour can be adjusted with the “Erode/dilate” function. Adjustment is tailored for the research by researcher using experience.
- The downstream contour and the designated nozzle position are connected with straight lines to close a complete jet contour.

After the processing, a complete vapor jet contour is formed. Processing error is found at the front of the jet which is penetrating, and the high speed jet distorts the surroundings (slightly compressed due to the high speed motion of fuel jet). This may somewhat affect the measurement of spray penetration causing fluctuations in the penetration curves.

The main differences in the visualization results among these three test fuels is shown in Fig. 4.7 to Fig. 4.9. To accommodate the color camera, image interpretation are configured as: Gamma is 1.5, white balance with red to be 1.23 and blue is 1.53, as the default setting of PCC 2.2 software. The visualization images in Fig. 4.7 show that at 450 K, all fuel types are clearly not vaporizing. At a background temperature of 550 K, the vaporization states are clearly different for the three fuels. As is expected, adding volatile fuel like gasoline into the diesel increases the vaporization regardless of the atomization mechanism. At 650 K, shown in Fig. 4.9, the fuels all vaporize. The

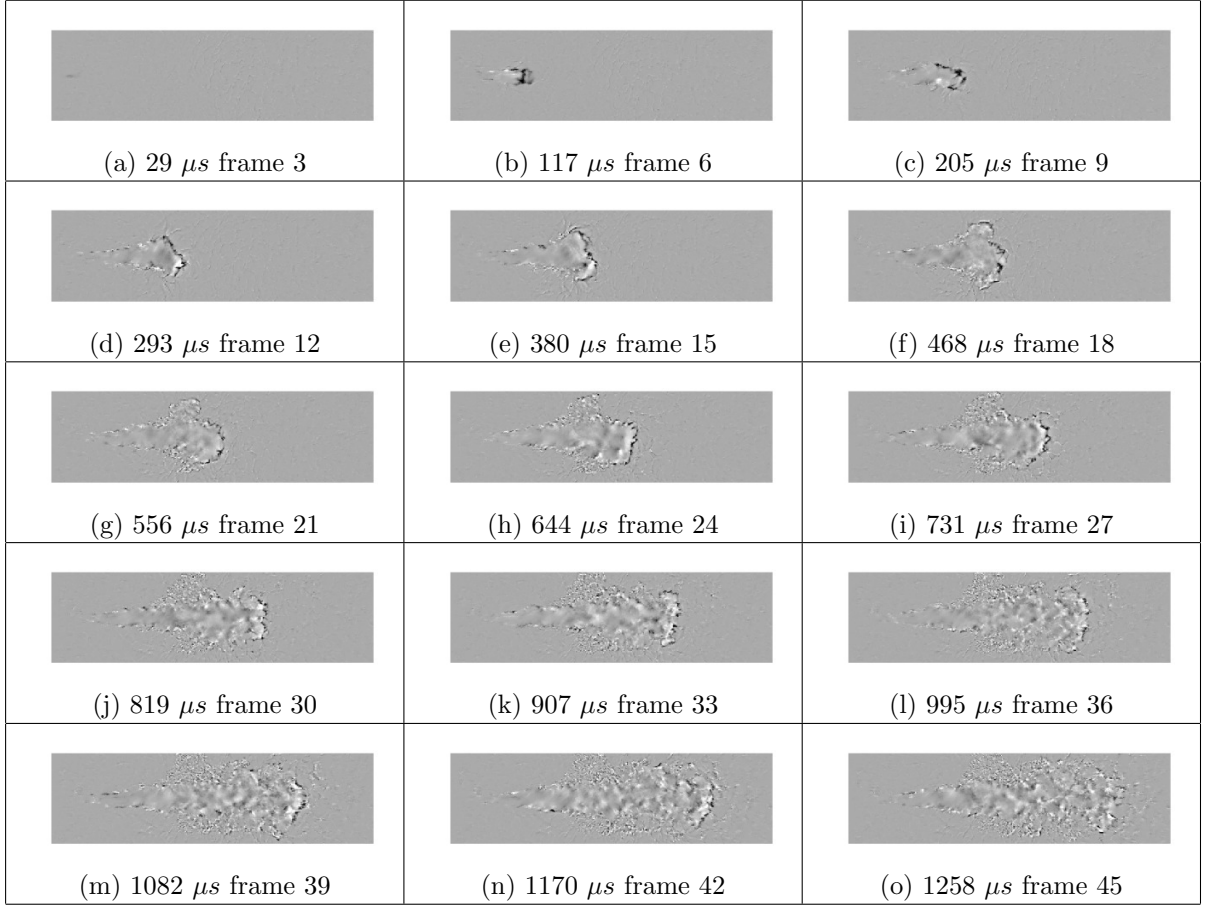


Figure 4.6: Jet evolution with a $T_{ch} = 750$ K jet of G60 Fuel (run#1) with frame subtraction, case bnldl001G60.

vaporization state seems to be advanced by adding gasoline fuel, but the advancement of onset is observed to be less than over 200 K (i.e. 650 K – 450 K) in these visualizations.

4.2 Gas Jet Results – from image post processing

Typical post-processed plots for gas jets are shown in this section. As is discussed in the Chapter 3, the experiments are designed around a base point of [T_{ch} =850 K, ρ_{ch} =22 kg/m³, P_{inj} =140 MPa] (or “bnldl” for the case name), which are the background temperature, gas density and injection pressure. To understand the effects of changing experimental conditions, only one aspect of the experiment is changed at a

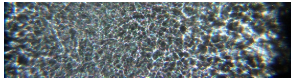
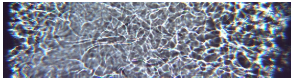
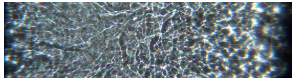
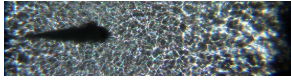
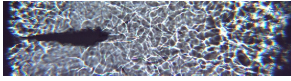
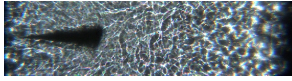
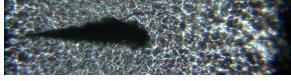
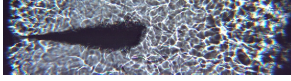
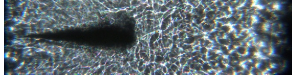
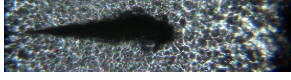
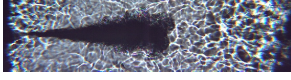
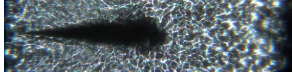
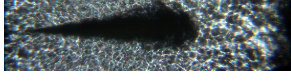
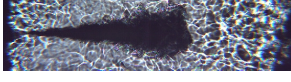
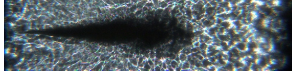
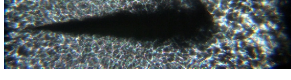
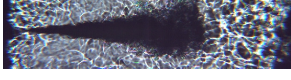
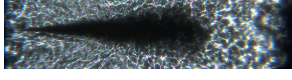
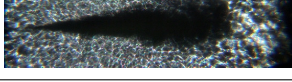
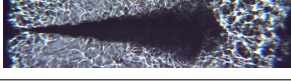
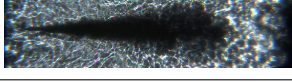
time/frame#	(a) G0	(b) G20	(c) G60
$40\mu\text{s}/2$			
$280\mu\text{s}/8$			
$520\mu\text{s}/14$			
$760\mu\text{s}/20$			
$1000\mu\text{s}/26$			
$1240\mu\text{s}/32$			
$1480\mu\text{s}/38$			

Figure 4.7: Jet evolution details at $T_{ch} = 450$ K chamber temperature, case brldl001.

time and the post processing is performed. The gas background density for the G0 fuel, G20 and G60 fuels is varied. The image processing algorithms then calculate the jet penetration, jet area and jet angle, as shown in Fig. 4.10 for several background gas densities. The variation of gas density is found to have the highest effect on the jet evolution compared to background temperature and injection pressure over the experimental range – these are later in the discussion of this chapter and will be discussed in Chapter 5. The vapor jet penetration decreases as the background density increases as shown in Fig. 4.10a. The start of injection has less than a frame delay, as discussed earlier, as the image processing program only starts seeing the jet when it emanates from the nozzle. For plotting, the jet penetration curves are moved toward the origin and the subsequent curves are plotted based on this.

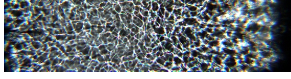
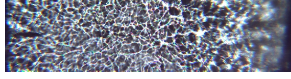
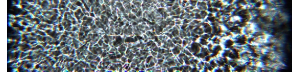
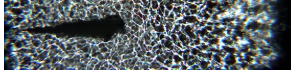
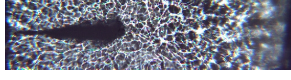
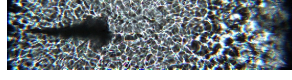
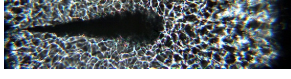
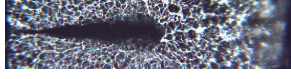
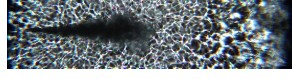
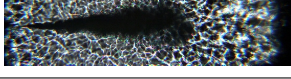
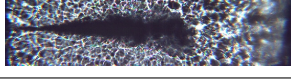

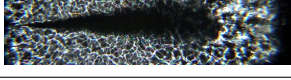
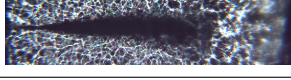
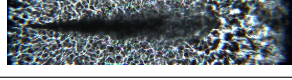
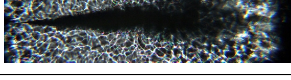

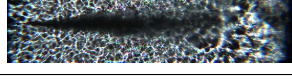
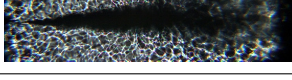
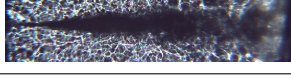
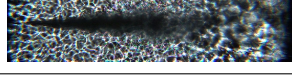
time/frame#	(a) G0	(b) G20	(c) G60
$29\mu\text{s}/2$			
$263\mu\text{s}/10$			
$497\mu\text{s}/18$			
$731\mu\text{s}/26$			
$965\mu\text{s}/34$			
$1199\mu\text{s}/42$			
$1433\mu\text{s}/50$			

Figure 4.8: Jet evolution details at $T_{ch} = 550$ K chamber temperature, case bxldl001.

The experimental data shown in Fig. 4.10 shows a clear trend as a function of chamber density variation. As the background density increases from 10 kg/m^3 to 22 kg/m^3 , the jet penetration decreases. The jet gas angle θ in Fig. 4.10c, shows a steady final value, while the jet area, A in Fig. 4.10b shows continuous increase as the background density increases. The remaining unchanged gas jet angle implies that the entire jet is quasi-steady. Further analysis of the jet penetration at times $t = 0.1 \text{ ms}$ and $t = 0.9 \text{ ms}$, plotted in Fig. 4.11 as a function of background density show an approximate linear relationship at $t = 0.9 \text{ ms}$. At the initial penetration (0.1 ms), the background density increase does not seem to affect the penetration. As the jet processes to 0.9 ms , the background density has a linear effect on the vapor jet. This effect is also seen with the jet angle plot in Fig. 4.10c as the angle

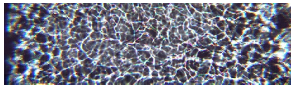
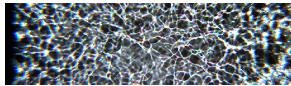
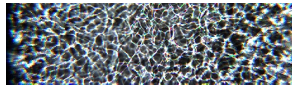
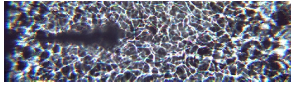
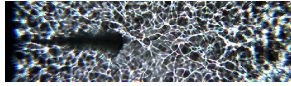
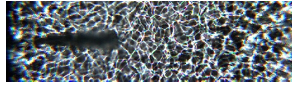
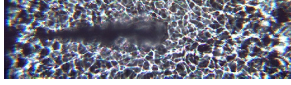
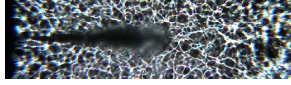
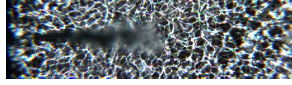
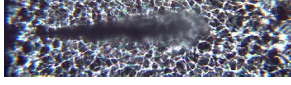
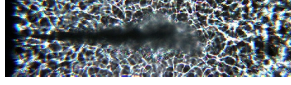
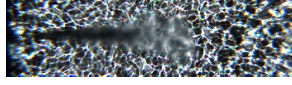
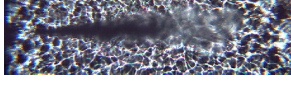
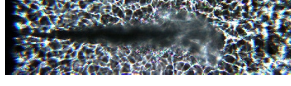
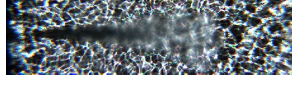
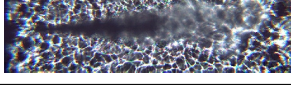
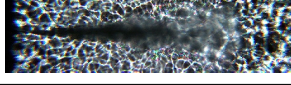
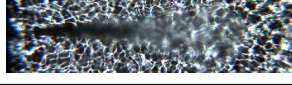
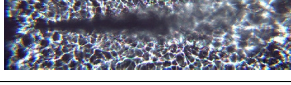
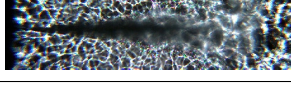
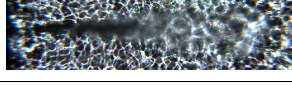
time/frame#	(a) G0	(b) G20	(c) G60
$29\mu s/2$			
$263\mu s/10$			
$497\mu s/18$			
$731\mu s/26$			
$965\mu s/34$			
$1199\mu s/42$			
$1433\mu s/50$			

Figure 4.9: Jet evolution details at $T_{ch} = 650$ K chamber temperature, case bpldl001.

tends to increase with the increase of background density. Therefore, in an actual engine stroke process, the jet angle should expand slightly as the piston continues to compress the charge. When designing an engine combustion chamber geometry, the chamber gas density is an important parameter to consider for the designer to have the knowledge at which crank angle the jet will hit the wall.

The jet angle varies from 15° to 22° as the chamber background density increases. In this experiment, an upper limit of the jet angle is not observed, but in Pickett et al. [2011] and Musculus [2009], a constant jet angle (around 19° to 21°) is used to model the jet. The jet area plot shows a linear growth rate in Fig. 4.10b. This implies that the jet grows steadily within a thermally-steady environment. The linearity is always observed within different kinds of fuel, and seems to be a well-known property

of turbulent jets instead of a fuel properties.

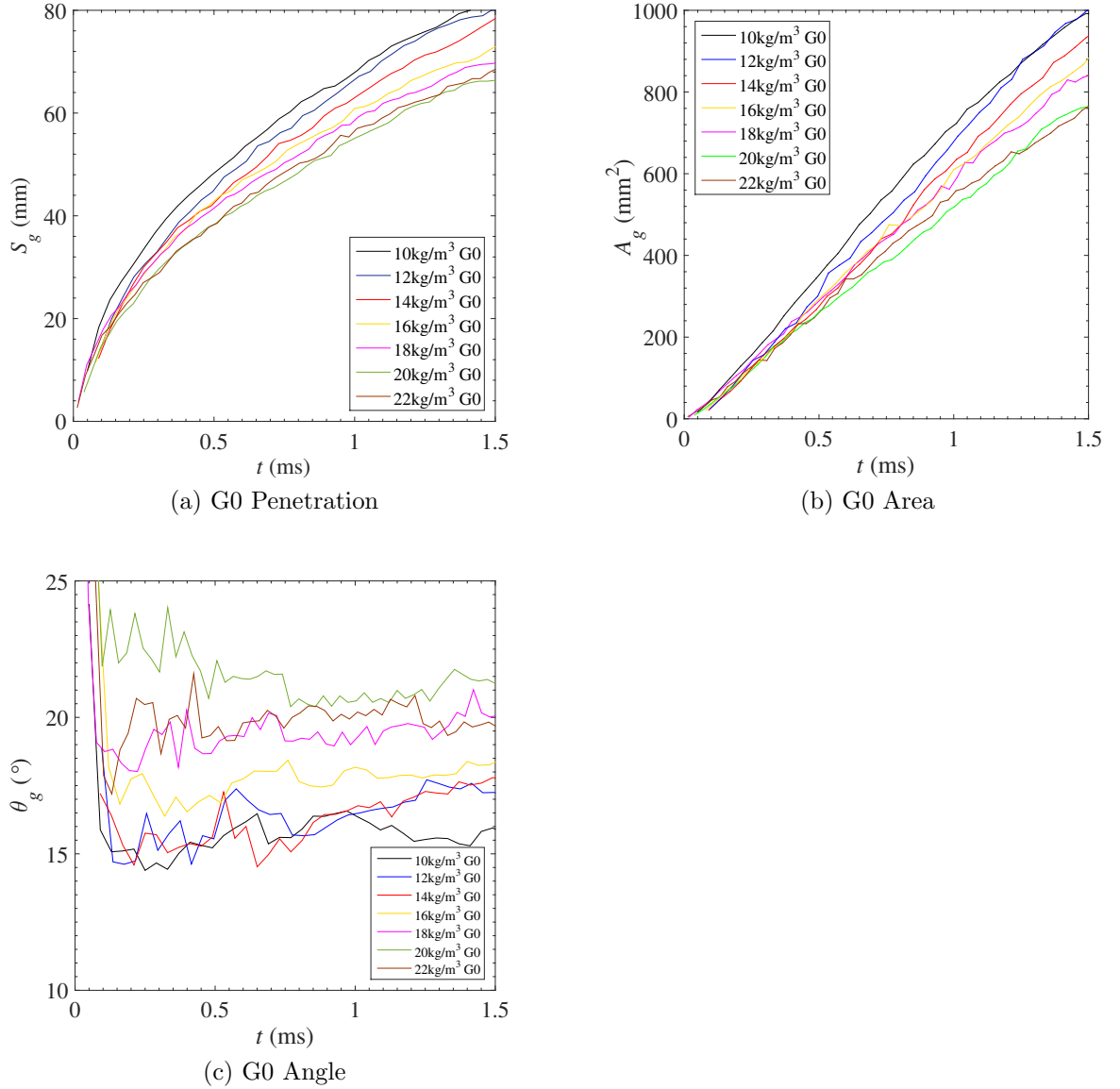


Figure 4.10: Gas jet behavior at various background Gas densities from 10 kg/m³ to 22 kg/m³, $T_{ch} = 850$ K and $P_{inj} = 140$ MPa

The penetrations at two different times are shown in Fig. 4.11. A linear regression indicates that at a short time after injection (0.1 ms), different chamber densities do not affect the initial penetration, while later at $t = 0.9$ ms, higher chamber density impedes the penetration of the jet. The regression equation is $S_g = -0.832 \cdot \rho_{ch} + 70.08$

for $t = 0.1$ ms and $S_g = -0.2 \cdot \rho_{ch} + 20.18$ for $t = 0.9$ ms.

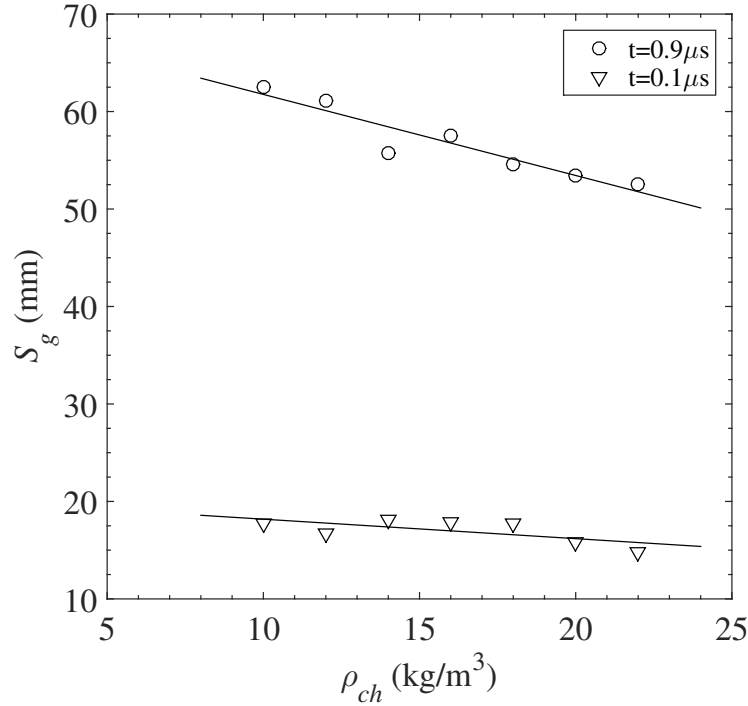


Figure 4.11: Penetration at different times for Fig. 4.10a.

While it is relatively straightforward to compare the background density, temperature and injection pressure variation for a single fuel, comparing two fuels is more difficult. To do so each fuel type, a full set of experiments (seven variations levels on chamber temperature, background gas density and injection pressure) is conducted. The typical comparison [e.g. Naber and Siebers, 1996] between fuel types is shown in Fig. 4.12 along with Fig. 4.10a, showing only density is variation. Jet penetration is found not to change much for different types of fuels. As an illustration, at $t > 1.1$ ms, the penetration sensitivities to different chamber densities are: G0 is -1.04 mm/[kg/m³], G20 is -1.16 mm/[kg/m³] and G60 is -1.03 mm/[kg/m³], as calculated from data. The overall trend of penetration appears independent of fuel type.

In summary, the results presented of the vapor jets are:

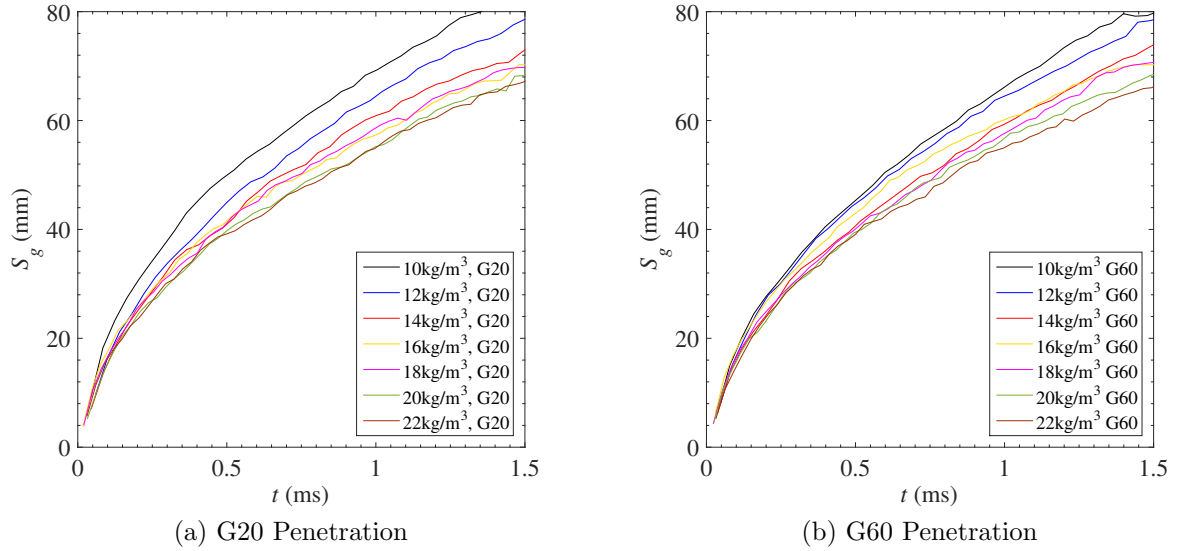


Figure 4.12: Gas penetration of G20 and G60 on density variation, $\rho_{ch} = 10$ to 22 kg/m^3 , $T_{ch} = 850 \text{ K}$ and $P_{inj} = 140 \text{ MPa}$.

- As the **temperature increases**, the jet penetration decreases, this change does not seem to be affected by fuel type. The area does not follow any specific trend as the curves are close together. A similar trend applies to the jet angle – no specific trend is observed as the temperature increases. The jet angle varies between 15° to 20° .
- As the **background density increases**, the jet penetration decreases. The decrease seems to be linear with the chamber gas density for pure diesel. As the blended gasoline percentage goes up, the penetration curves does not seem to be affected. The jet area plots follow almost the same trend as the penetration plots. At $t = 1.5 \mu s$, the maximum jet area is approximately 1000 mm^2 for 10 kg/m^3 chamber gas density and the minimum jet area is approximately 800 mm^2 for a 22 kg/m^3 background density. Similar observations occur for the G0, G20 and G60 cases. The steady jet angle shows no specific trends for the three different types of fuel. The steady jet angles are between 15° to 23° .

- As the **injection pressure increases**, the penetration increases as expected, and the effect seems to be linear. For each of the different fuels (G0, G20 and G60), this observed span of the jet penetration increase remains unchanged by each injection pressure increase (10 MPa). The jet angles do not show a specific trend for the increase of injection pressure. The dieseline jet angles seem to have less variation with injection pressure than the pure diesel cases. The jet angles vary from 17° to 21° in this test.

4.3 Liquid Jet Results – from image post processing

The time evolution of the liquid jet for cases of density variation is shown in Fig. 4.13. The liquid jet is characterized with the quasi-steady penetration length S_l , and the jet area A_l as is shown in Fig. 4.13a and Fig. 4.13b. These two subplots have similar time profiles, which may indicate the linear dependency of jet area and jet penetration temporal plots. Therefore, it is deemed sufficient only to examine their penetration curves. Further examination of the linearity can be found in Chapter 5.

The quasi-steady liquid jet penetration, S_l in Fig. 4.13, decreases as that the ambient gas density increases. The jet penetrations will be further discussed in Chapter 5, where the penetration distance will be fitted to an exponential function. The study by Desantes et al. [2005] also shows an influence of the ambient density change on the quasi-steady penetration length. As described, in the last section, the vapor jet penetration also decreased with the increase in ambient gas density, so ambient gas density clearly affects both the spray growth rate and the quasi-steady jet length. While the other parameter, injection pressure, does not show a significant influence on the penetration (more details in Appendix B).

For the liquid jet, the injection pressure is varied from 80 to 140 MPa around the base cases for fuels G0, G20 and G60 in Fig. 4.14a, Fig. 4.14b and Fig. 4.14c

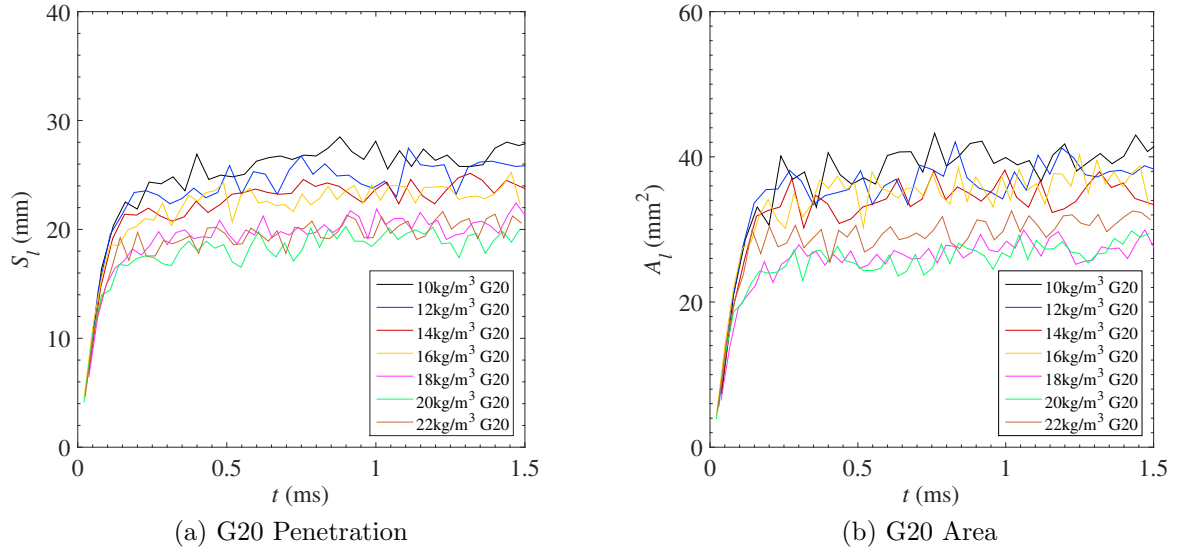


Figure 4.13: Liquid jet Penetration and jet area plot with background density varies from 10 to 22 kg/m³, $P_{inj} = 140$ MPa and $T_{ch} = 850$ K.

respectively. For each type of fuel, the jet penetration is only weakly affected by the injection pressure. Unlike the vapor jet observations, when comparing the three fuels, the liquid jet penetration is now dependent on the fuel type and shows a marked decline in the final ($t > 0.6$ ms) penetration length S_l as the gasoline blend percentage increases. For the case shown in Fig. 4.14, the quasi-steady jet penetration decreases from about 20 mm to 17 mm and finally to 15 mm for the G0, G20 and G60 cases. These values are also shown in Chapter 5 and are the curve fit. For actual engine operation, a decrease of liquid penetration prevents the fuel impingement, which affects the engine design Arcoumanis et al. [1997]. For the G60 case at 120 MPa the penetration curve seems to deviate from the trend of the other cases in Fig. 4.14c. The quasi-steady jet length is less than 13 mm at 120 MPa while other injection pressure shows quasi-steady jet length of 14-16 mm (more discussion in Chapter 5). This could be attributed to pressure oscillations in the high pressure pump and in the injector common rail that are observed for this case when running the experiment. When

conducting the experiment, higher pressure fluctuations are observed with higher gasoline blended fuel. Unfortunately, the rail pressure data cannot be exported from the system in this study.

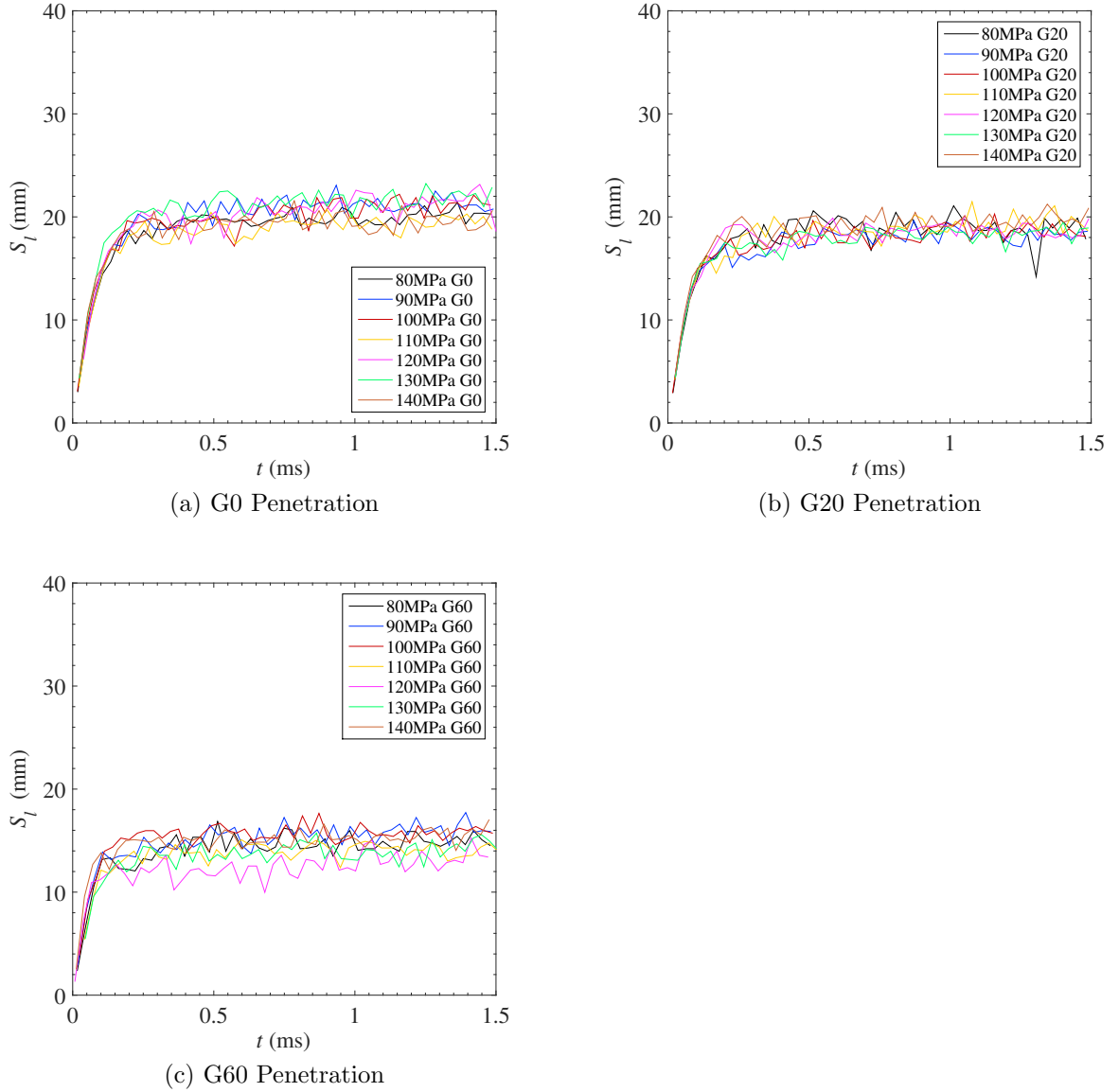


Figure 4.14: liquid jet penetration on various injection pressure ($P_{inj} = 80$ MPa to 140 MPa) G0, G20 and G60, $\rho_{ch} = 22 \text{ kg/m}^3$ and $T_{ch} = 850 \text{ K}$.

4.3.1 Effect of temperature on vaporization

To understand the effect of vaporization, the effect of temperature on the liquid jet is examined. The chamber temperature is varied from approximately 300 K to 850 K. This range covers non-evaporation to complete evaporation of the three gasoline/diesel blended fuels. Complete evaporation is defined as when the liquid jet reaches a quasi-steady length. For example G20 fuel penetration length S_l and jet angle θ_l are plotted for 7 chamber temperatures T_{ch} in Fig. 4.15. The liquid penetration plot Fig. 4.15a shows that the evaporation is complete when a quasi-steady penetration length of approximately 45 mm is reached at $t = 0.7$ ms at $T_{ch} = 650$ K. Higher temperatures promote the faster jet evaporation and a shorter penetration length. For example, in Fig. 4.15 at 850 K chamber temperature, the jet vaporization is complete at $t = 0.15$ ms and at a penetration length $S_l = 19$ mm into the chamber. A quantitative relation between the quasi-steady jet length and the temperature cannot be plotted from this study due to insufficient data. This experiment is limited by the resolution of the temperature controller and the maximum combustion chamber temperature. Equation (18) in Siebers [1998] uses the enthalpies of ambient gas and liquid fuel to estimate the quasi-steady jet length as introduced in Chapter 2. This relation is complicated and difficult to correlate directly with the ambient temperature as is discussed with Eq. 2.2.6 and Eq. 2.2.8 in Chapter 2. Figure 13 in Siebers [1998] gives plots that show the non-linear trend of temperature variation. They did not provide an equation for the temperature, so instead the model from Higgins et al. [1999], shown in Eq. 2.2.8, is widely used in the current literature.

For the jet angles shown in Fig. 4.15b, it is found that non-evaporating and evaporating jets have a slightly different steady jet angle. The evaporating jet angles are approximately 11° while the non-evaporating jet angles are approximately 14° . These values are approximations since an equation to estimate the steady angle is not yet

available. This difference in jet angle is not unexpected because the jet morphology is abruptly changed once complete evaporation has occurred. At some time after injection, the jet angle measurement stabilizes to a nearly constant value as shown in Fig. 4.15b. The observed liquid jet spray angles are always less than the observed vapor jet case, meaning that the liquid jet is contained within the vapor jet.

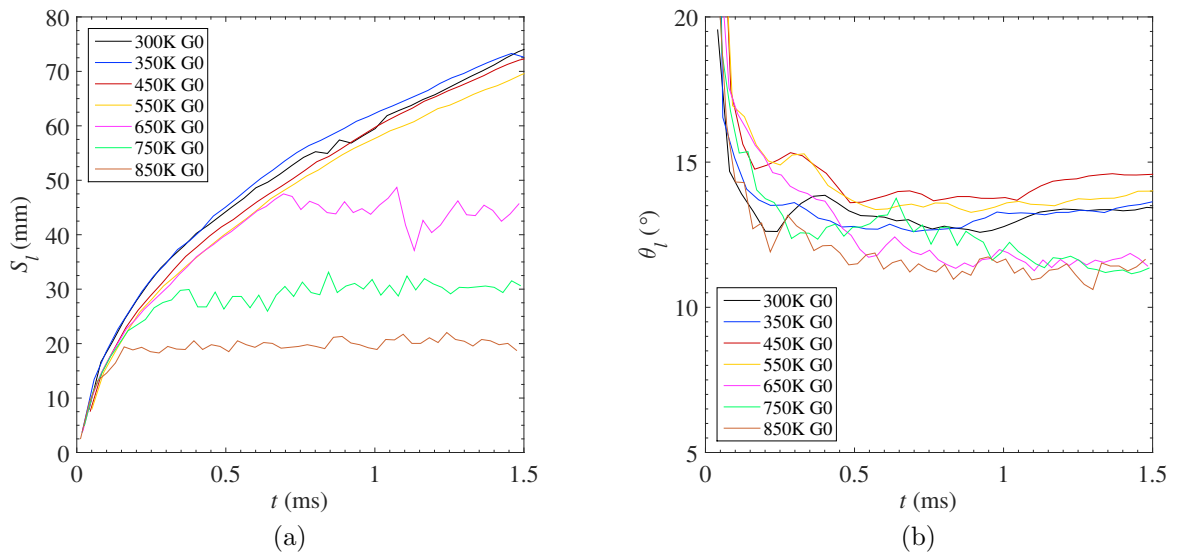


Figure 4.15: Examination of temperature variation ($T_{ch} = 300 \text{ K} - 850 \text{ K}$) on liquid jet penetration and jet angle, $\rho_{ch} = 22 \text{ kg/m}^3$ and $P_{inj} = 140 \text{ MPa}$.

While jet penetration curves are not sensitive to the start of evaporation, the jet area curves are shown to be better indicators for the start of evaporation. As is shown in Fig. 4.16, the curves start deviating from the lower temperature curves at a temperature of 550 K. This matches what is seen in Fig. 4.8. The difference in evaporation between the three fuels in Fig. 4.16 does not seem large when compared to the visualization results in Fig. 4.7, Fig. 4.8 and Fig. 4.9. Thus it seems that the blending gasoline into diesel does not significantly reduce the required background temperature for the jet to evaporate. Only for the G60 case in Fig. 4.16c perhaps is the liquid jet converging into a quasi-steady value at 550 K. At higher temperatures

the steady lengths all decrease with increasing gasoline content.

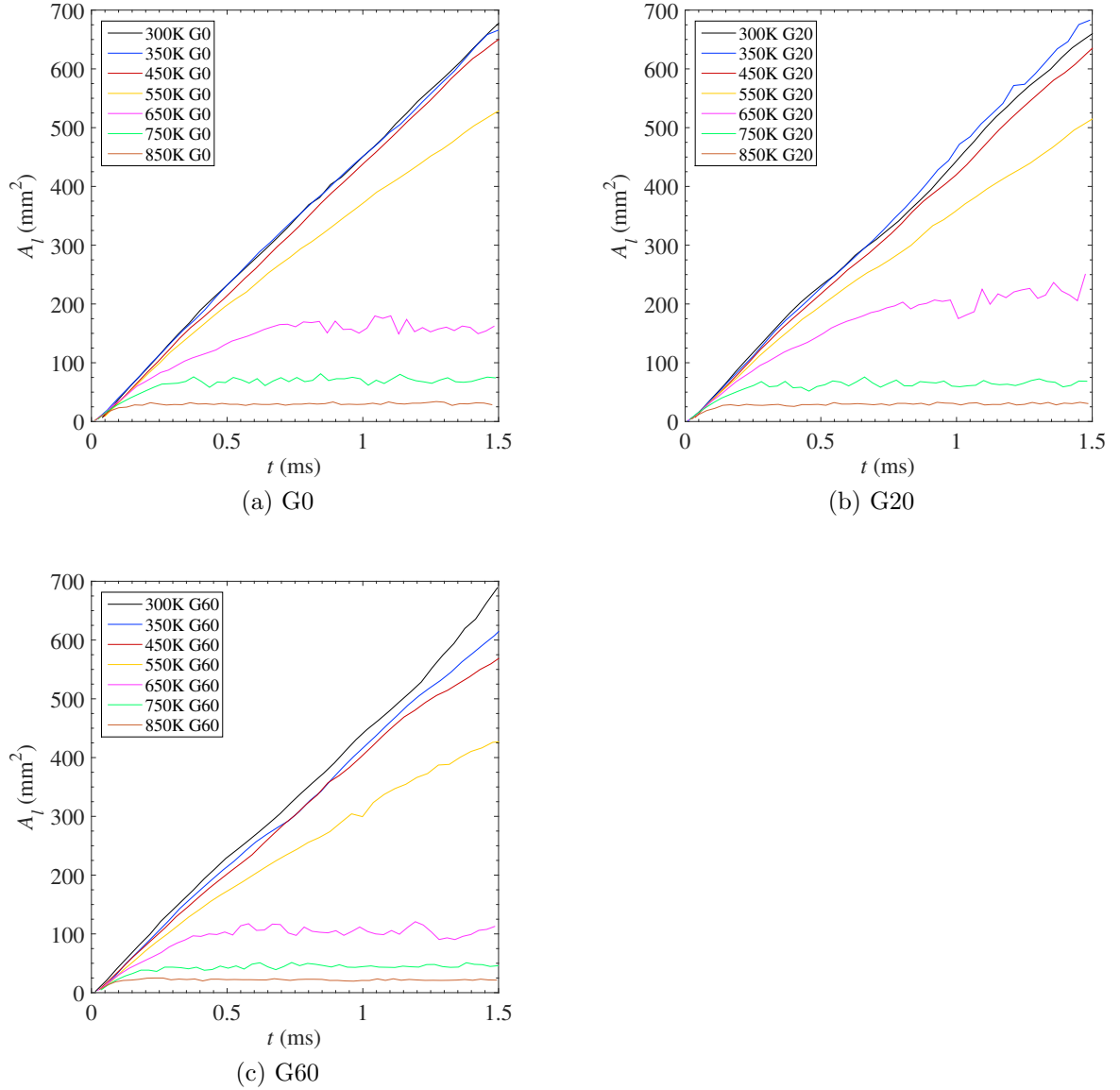


Figure 4.16: Jet area plots for the three fuel blends (G0, G20, G60) on temperature variation ($T_{ch} = 300 \text{ K} - 850 \text{ K}$), $\rho_{ch} = 22 \text{ kg/m}^3$, $P_{inj} = 140 \text{ MPa}$.

A summary of this section is:

- As the **background density increases**, the jet penetration decreases. As a comparison, the quasi-steady penetration of background density 22 kg/m^3 converges at approximately 20 mm, 18 mm and 14 mm for G0, G20 and G60

fuel respectively, meaning higher gasoline ratio shortens the liquid jet length. The jet area seems to be linearly correlated with jet penetration. In contrast, the jet angle increases as the background density increases. The jet angles are ranged at 8° to 15° for all the three types of fuel.

- The penetration of the jet seems to be uncorrelated with **injection pressure** in the experimental range, as is shown in Fig. 4.14. The jet angle is neither a function of injection pressure. The G60 jet angle plots fluctuate much more as compared with the G0 and G20 cases. For the G0 and G20 cases, the jet angles range from 12° to 14° . While in the G60 case, the jet angles range from 12° to 18° .
- As the **chamber temperature increases**, the jet behavior is as plotted in Fig. 4.15 and Fig. 4.16. This test involves the transition from a non-evaporating jet to an evaporating jet, which discussions must be separated. Detailed discussion on the jet penetration and area plots is seen above. The jet angle behavior is not seen to be sensitive to the chamber temperature except when the phase transition (from non-evaporating to evaporating jet) is completed. The jet angle is observed to be between 11° to 14° for all three fuels tested.

CHAPTER 5

DISCUSSION

This chapter further explores the experimental results and the inner relationship of the output variables. First the jet self-similarity assumption is validated from the jet penetration, jet area and jet angle data. Secondly, the quasi-steady liquid jet length is fitted with the first order linear time-invariant (LTI) response equation. Quantified results are discussed here and the sensitivities of the independent variables (chamber temperature, background gas density, injection pressure and fuel type) are found. Finally, the jet penetration, jet area and jet angle data are compared with the literature to show the validity of this study.

5.1 Jet Self-Similarity Analysis

Self similarity is often assumed for a shear-free jet at $S/d_0 > 30$ [Pope, 2000]. Self-similarity assumes the flow development to be uniform in the stream-wise direction. From Pope [2000], the self-similarity variables can be defined as the following equations in a shear free jet.

$$\eta_1 = \frac{r}{R} \tag{5.1.1}$$

$$\eta_2 = \frac{r}{S} \tag{5.1.2}$$

To further correlate the similarity, the spreading rate (Ω) is defined. Realizing the Ω is constant within the jet, the two self-similarity parameters are correlated with Ω as shown below.

$$\Omega = \frac{dR}{dS} \quad (5.1.3)$$

$$\eta_2 = \Omega \cdot \eta_1 \quad (5.1.4)$$

Indicating the 2-D projection of a jet can be seen as a triangle. The Ω will be approximated as the tangent of jet half angles. The jet projected area is therefore calculated with the triangle area formula. The resulting equation indicates the three output parameters (jet area, jet penetration and jet angle) are correlated in a self-similar jet, which is shown below.

$$\Omega = \tan(\theta/2) \quad (5.1.5)$$

$$A = \frac{1}{2}(2R)S = S^2 \tan(\theta/2) \quad (5.1.6)$$

To examine the validity of the relation shown in Eq. 5.1.6, plots are generated as shown with Fig. 5.1 and Fig. 5.2. From observations, the curves in Fig. 5.1 and Fig. 5.2 match well, indicating the equation is usable for a self-similar jet. Furthermore with a self-similar jet, a constant experimental angle (instead of using time-series jet angle data) can be assumed and the results is seen in Fig. 5.2. To generalize this equation for this experiment, it applies to all fuel blends (G0, G20 and G60) in vapor jet images and non-evaporating liquid jet images.

A careful researcher may question the goodness of fit between prediction and experimental observations. This experiment adapts specific definitions of the jet penetration and jet angle, and would be misleading if the definition already contained an assumption of self-similarity. Reviewing the jet measurement scheme given by the

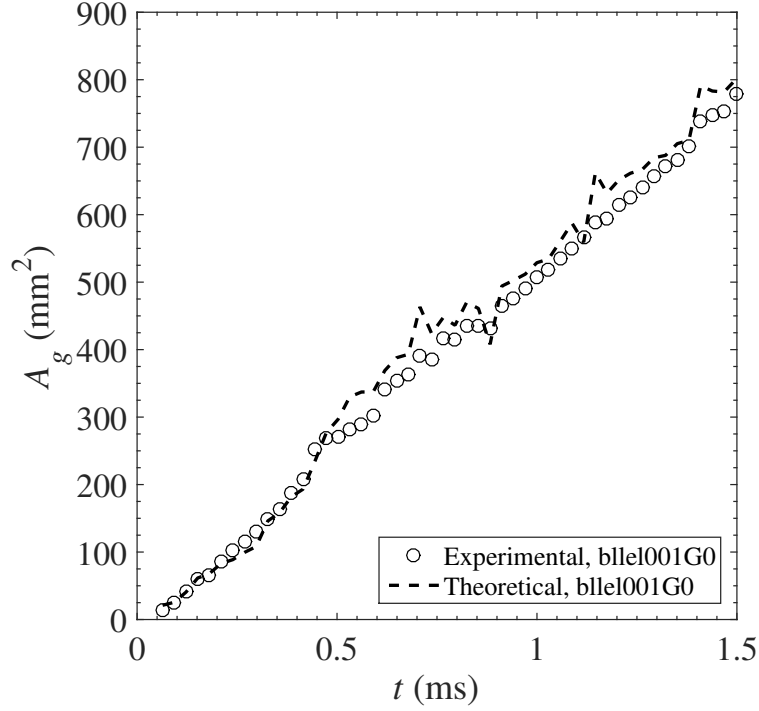


Figure 5.1: Self-similarity prediction applied to vapor jet, with $P_{inj} = 130$ MPa, $T_{ch} = 850$ K, $\rho_{ch} = 22$ kg/m³, G0 case 1.

Sandia National Lab, U.S. [Siebers, 1999], the jet angle is defined with the selected portion of jet (starts with x_1 , ends with x_2). The post-processing algorithm adapted a simplified version (at each time instant, $x_1 = 0$, x_2 is half of the jet) of the equations shown:

$$\frac{\theta}{2} = \tan^{-1} \left(\frac{A_x}{x_2^2 - x_1^2} \right) \quad (5.1.7)$$

$$\frac{\theta}{2} = \tan^{-1} \left[\frac{A_x}{(0.5b)^2} \right] \quad (5.1.8)$$

The equations are very similar to the self-similarity equation in the mathematical form. In the equation, b is the observed jet end, and A_x is the upstream half of the jet area measured (the portion of $< 0.5b$). Discarding b as the final jet penetration, the program searches an arc with $\theta/2$ angle, starting at the nozzle position. The final

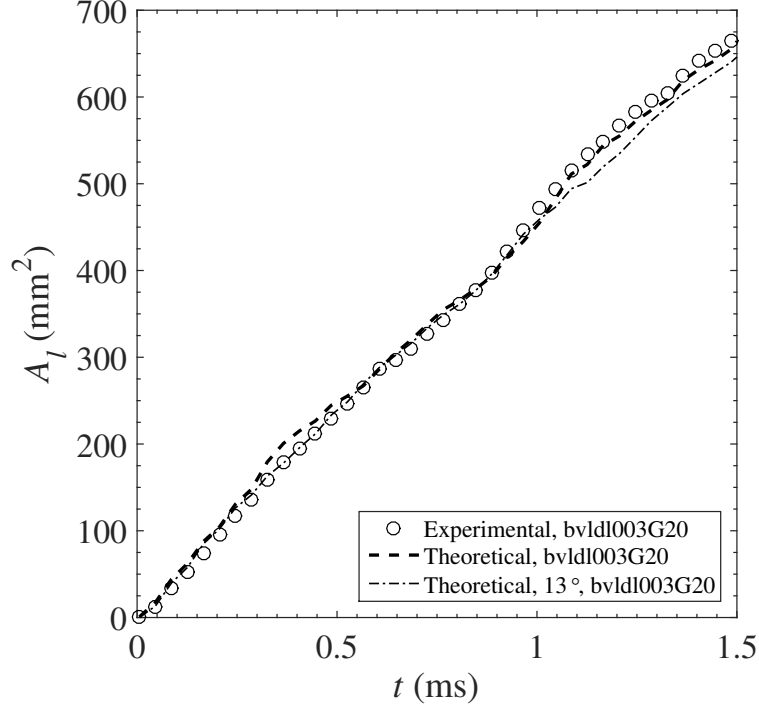


Figure 5.2: Self-similarity prediction applied to liquid jet, $P_{inj} = 140$ MPa, $T_{ch} = 300$ K, $\rho_{ch} = 22$ kg/m³, G20 case 3.

penetration S is defined where the arc has more than half of the pixels outside of the jet (based on the contour detected).

Examining this definition, the program does begin with the self-similarity assumption, cutting the jet into half and using the upstream portion ($< 0.5b$), where similarity is well preserved, to define the spray angle. Further, even though the parameter b is not equal to the penetration S , they are close in value if the measurements are accurate enough. The arc-searching method is more like a fail-safe mechanism in finding the jet penetration. In the actual measurement, S is shown to be close to b . For later references, the upstream half of the jet is expressed as $< 0.5S$.

Overall, the good match of the similarity equation 5.1.6 with the experimental observations is partially due to measurement algorithm. Siebers [1999] assumes the upstream half of the jet ($< 0.5S$) is self-similar, and the experimental data confirm

that the entire jet is well represented by the self-similarity assumption (gas phase and liquid phase), even if the jet shape is more irregular rather than a pure triangle (as seen in Fig. 3.7 in Chapter 3). The examination justifies much of the current literature which only concerns the jet penetration, because the jet area can be well predicted with the measurement of jet penetration and a constant jet angle.

One might ask if jet area is an independent variable, since in an independent study the jet area can be extrapolated from measurements of jet penetration and jet angle. The answer would be yes because jet area shows obvious linear behavior compared with the other two and it physically represents the jet dispersion. It is only when the area plots were generated that researchers realized the relationship between jet penetration and time. Thus the relationship is by correlation, and is not implicit. The linearity of jet area is shown below for a liquid jet. In addition, with the jet area shown to be linear, the jet penetration is therefore related with \sqrt{t} as shown in Fig. 5.3.

For a non-self-similar jet, the self-similarity correlation is not assumed, as seen with Fig. 5.4. The self-similarity equation, Eq. 5.1.6, does not accurately predict an evaporating liquid jet. In these cases, the jet area is independent of jet penetration and jet angle. In fact, where a quasi-steady jet length is obtained, the jet penetration is more linearly correlated with the jet area, as fitted with Fig. 5.5.

The distinction between a self-similar jet and a non-self-similar jet becomes useful when searching for the point of evaporation in the liquid jet data. Fig. 5.6 illustrates the change of chamber temperature from 450 K to 650 K for fuel G20. It is seen that at a temperature of 650 K, significant evaporation is observed. Before that, the self-similarity is well-preserved over the entire jet; therefore the evaporation is not initiated at 550 K.

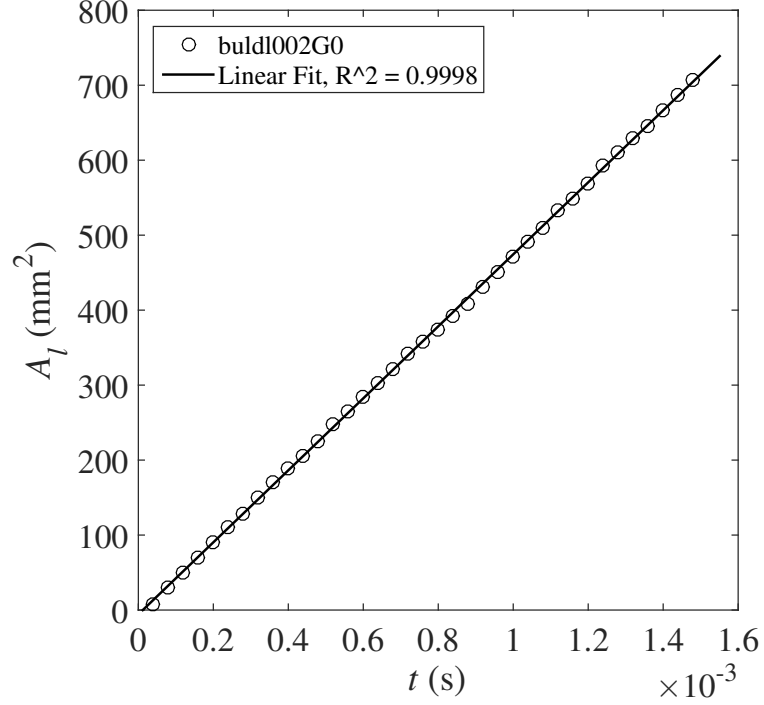


Figure 5.3: Self-similarity evident on area plot, $P_{inj} = 140$ MPa, $T_{ch} = 350$ K, $\rho_{ch} = 22$ kg/m³, G0 case 2, Liquid Jet, $R^2 = 0.9998$, slope = 4.801×10^5 mm²/s, intercept = -5.712 mm².

5.2 Sensitivity of Independent Variables

The sensitivity of the input parameters (background density, temperature and injection pressure) to the output quasi-steady jet liquid length (L) is studied in this section. Fitting is done with the response equation in the first order LTI system.

$$S = L(1 - e^{-t/\tau}) \quad (5.2.1)$$

L is found so as to predict the sensitivities. Only the liquid jet quasi-steady length is studied in this work; the time constant τ will not be discussed. The vapor jet processing is not done with a unified criterion therefore, quantifiable discussions may not be accurate. For the non-evaporating jet, the L is not attained, and therefore is not discussed in this context either. In another set of equations, $S \propto \sqrt{t}$ can be

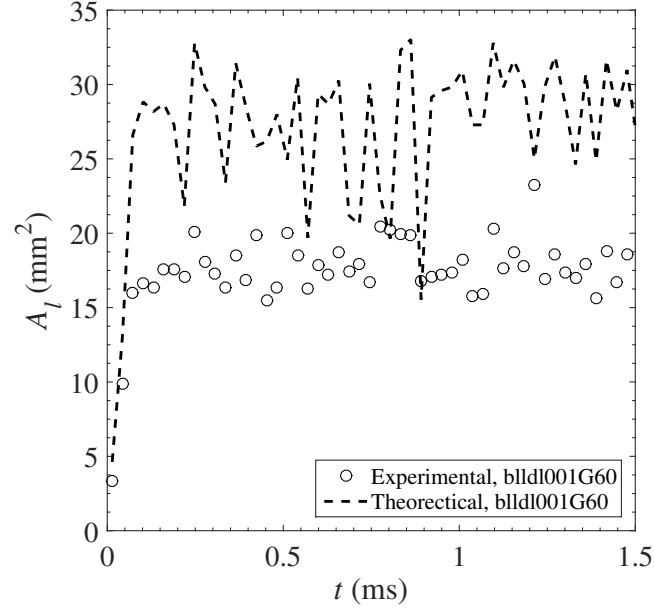


Figure 5.4: Self-similarity prediction with high temperature liquid jet, $P_{inj} = 140$ MPa, $T_{ch} = 850$ K, $\rho_{ch} = 22$ kg/m³, G60 case 1.

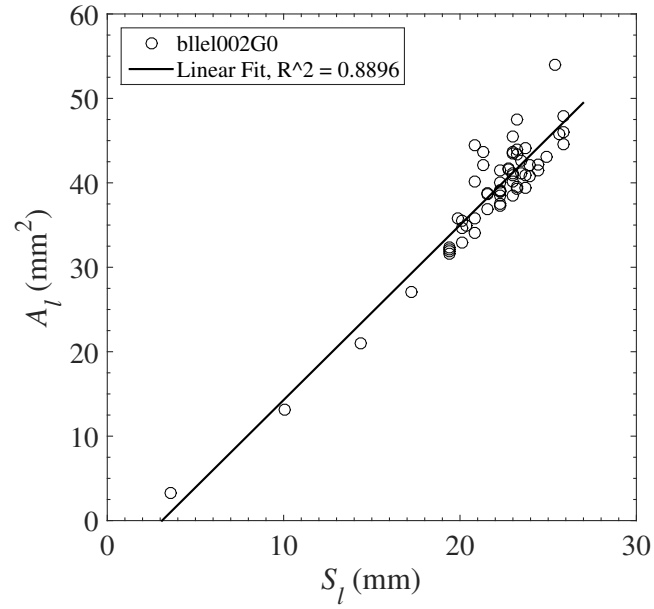


Figure 5.5: Jet area v.s. jet penetration, $P_{inj} = 130$ MPa, $T_{ch} = 850$ K, $\rho_{ch} = 22$ kg/m³, G0 case 2 on injection pressure variation test, liquid jet, $R^2 = 0.8896$.

used as is seen in the literature, and is compared in next section. The constant shown in this equation, which has units of $[\text{mm}/\sqrt{s}]$, does not contain the physical

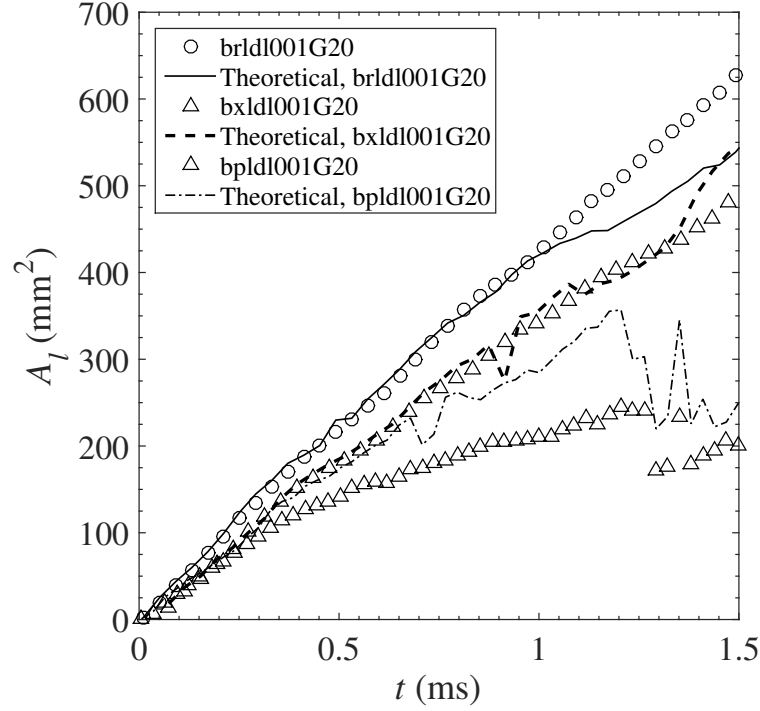


Figure 5.6: Jet self-similarity change over chamber temperature 450 K to 650 K, $P_{inj} = 140$ MPa and $\rho_{ch} = 22$ kg/m³ respectively.

meaning of jet growth rate. As a result of self-similarity discussed in previous section, the equation $A \propto t$ is more appropriate when comparing the sensitivities of input variables; because the constant [mm²/s] represents the jet growth rate. The non-evaporating jet sensitivity is not yet discussed for this section.

The findings of Fig. 5.7 – Fig. 5.9 display some trends. As the background gas density increases, the quasi-steady jet length decreases almost linearly. The same observation is found with the increase of background temperature. There are only three data points in the evaporating jet temperature tests, therefore the linearity is not well demonstrated. For the injection pressure cases, the increase of injection pressure shows a small effect to the quasi-steady jet length compared with the previous two variables. In general, fuels with higher volatility decrease the quasi-steady jet length. The quantified sensitivities are shown with Table 5.1 using linear regression. How-

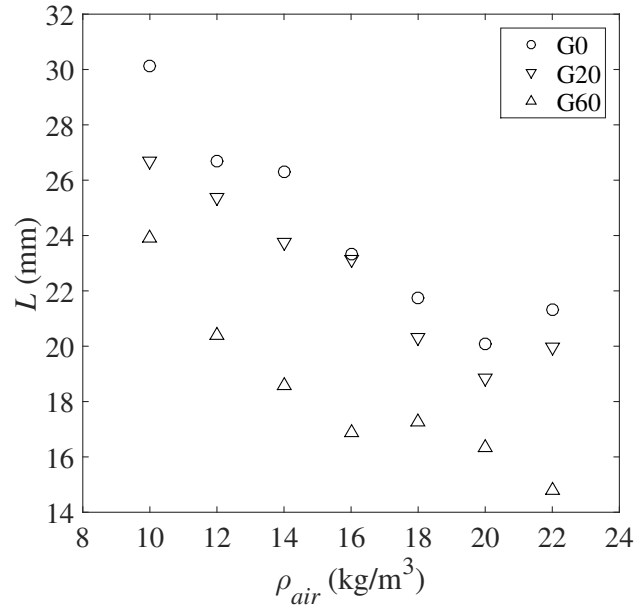


Figure 5.7: The effect of density on quasi-steady liquid jet length.

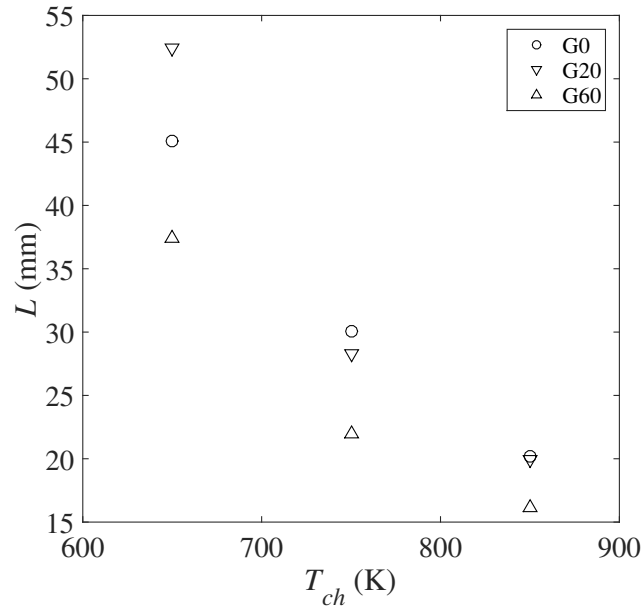


Figure 5.8: The effect of temperature on quasi-steady liquid jet length.

ever, these absolute sensitivities do not give comparison among the three independent variables. A dimensionless sensitivity table must be given.

The dimensionless sensitivity table can be considered over the experimental span

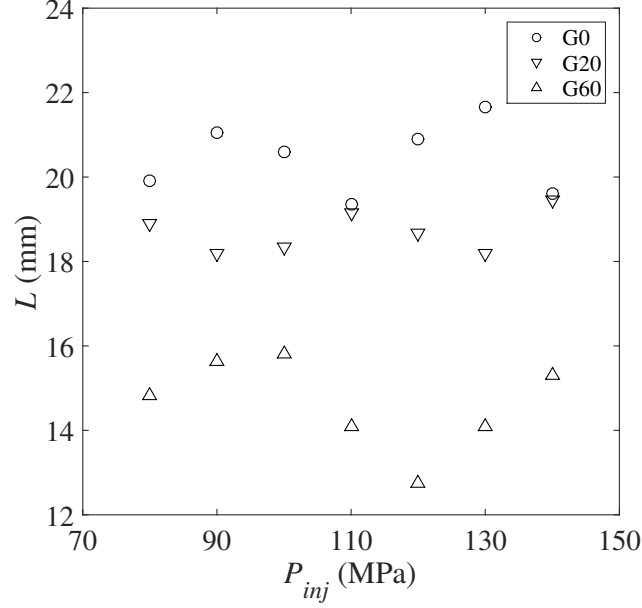


Figure 5.9: The effect of injection pressure on quasi-steady liquid jet length.

	G0	G20	G60
P_{inj}	0.00197mm/MPa	0.007179mm/MPa	-0.01686mm/MPa
ρ_{ch}	-0.7898mm/[kg/m ³]	-0.6546mm/[kg/m ³]	-0.6582mm/[kg/m ³]
T_{ch}	-0.1248mm/K	-0.1626mm/K	-0.1061mm/K

Table 5.1: Summary of sensitivities.

of each independent variable. For instance, the chamber temperature span of the quasi-steady penetration length measurement is 200 K (850 – 650 K), and this span can be considered as 100%. The maximum absolute change of L over the different spans occurs at the G20 chamber temperature case, with change to be 32.52 mm. This maximum change is used as the length scale for comparison. As is shown in Table 5.2, the local maximum is -1.00 at G20 T_{ch} case, and other cases are compared to this value. It is observed that the chamber temperature affects the quasi-steady jet length most, while the injection pressure shows negligible effect on L . Changing the gasoline blended ratio does not seem to change the sensitivities on any of the independent variables.

	G0	G20	G60
P_{inj}	0.00	0.01	-0.03
ρ_{ch}	-0.29	-0.24	-0.24
T_{ch}	-0.77	-1.00	-0.65

Table 5.2: Non-dimensional sensitivities.

For fuel type, the sensitivity to fuel blend is not desirable because this would make the fuel mixing technology complex and difficult to employ. In addition, the physical properties (viscosity, heat capacity and etc.) of the blended fuel are unavailable to characterize the fuel in this study. The box-plots of L for different fuels are given below as a reference.

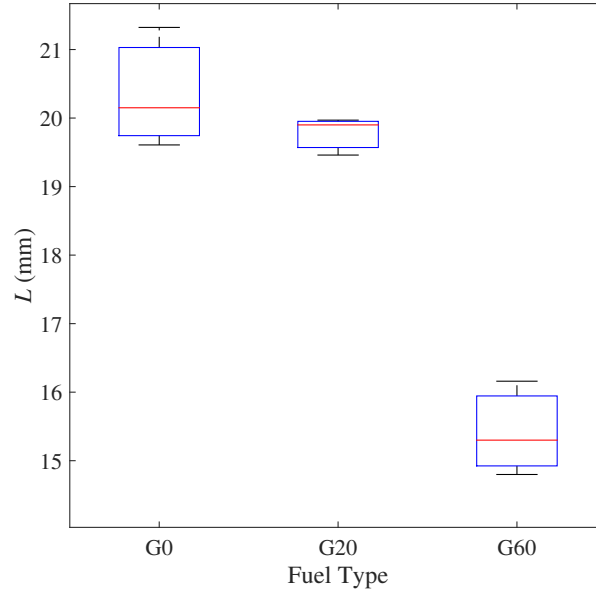


Figure 5.10: different fuel effect on quasi-steady liquid length, with $P_{inj} = 140$ MPa, $T_{ch} = 850$ K, $\rho_{ch} = 22$ kg/m³, each box contain 3 tests.

5.3 Comparison to the Literature

5.3.1 Penetration Data

Comparison of jet penetration is widely available in the current literature. However, data from the literature are not conducted under the same experimental conditions and equipment. Therefore it is most convenient to compare the literature findings with their predictive models. The literature findings are summarized in the Table 5.3.

Authors	Equations
J.C. Dent [1971]	$S = 13.6[(\frac{\Delta P}{\rho_{ch}})^{1/2} t d_0]^{1/2} \frac{530}{T_{ch}}$
Hiroyasu & Arai [1990]	$S = 2.95(\frac{\Delta P}{\rho_{ch}})^{0.25} (d_0 t)^{0.5}$
Naber & Siebers [1996]	$\tilde{t} = \frac{\tilde{S}}{2} + \frac{\tilde{S}}{4} \sqrt{1 + 16\tilde{S}^2} + \frac{\ln(4\tilde{S} + \sqrt{1 + 16\tilde{S}^2})}{16}$
Musculus & Kattke [2009]	$t = \frac{1 - \rho_{ch}/\rho_l}{2\beta u_f} [S + \frac{S}{2} \sqrt{1 + (qS)^2} + \frac{1}{2q} \ln(qS + \sqrt{1 + (qS)^2})]$
S. Sazhin [2014]	$S = \frac{\sqrt{u_f d_0 t}}{(\rho_g/\rho_{ch})^{1/4} \sqrt{\tan \theta}}$

Table 5.3: Summary of literature.

Many of the equations require estimation of parameters and more explanations, which can be summarized below,

- Dent [1971] model is in imperial unit.
- Hiroyasu and Arai [1990] model requires the calculation of the first breakup mode time (or transient time), which is found to be 0.05ms, which is negligible.
- Naber and Siebers [1996] and Musculus and Kattke [2009] used numerous non-dimensional variables, which are explained below.

- Sazhin [2014] requires the entrainment parameter in his equation, which is approximated as 0 for this practical spray. Sazhin [2014] justifies this in his Chapter 2. Sazhin's model is based on a physical model instead of on experimental data.

The following parameters are involved for Siebers model and Musculus model to estimate the required inputs [Sandia, 2011]. For a brief introduction: C_d is the discharge coefficient of nozzle; C_v is the velocity coefficient of nozzle; u_f is the corrected injection velocity; d_f is the corrected nozzle size; x_0 is estimated start point of cone-shaped jet; α is the corrected jet angle; q is the non-dimensional penetration parameter.

$$C_d = \frac{\Delta m}{\Delta t A_0 \rho_l \sqrt{\frac{2\Delta P}{\rho_l}}} \quad (5.3.1)$$

$$C_v = C_d / C_a \quad (5.3.2)$$

$$u_f = C_v \sqrt{2 \frac{\Delta P}{\rho_l}} \quad (5.3.3)$$

$$d_f = \sqrt{C_a} d_0 \quad (5.3.4)$$

$$x_0 = \frac{1}{2} \frac{d_f}{\tan(\alpha/2)} \quad (5.3.5)$$

$$\alpha = \tan^{-1}(a \tan(23^\circ)) \quad (5.3.6)$$

$$q = \sqrt{\frac{4\pi\beta}{A_0} \frac{\rho_{ch}}{\rho_l} \frac{\tan \theta/2}{1 - \rho_{ch}/\rho_l}} \quad (5.3.7)$$

The nozzle discharge coefficient (C_d) used for this comparison is 0.94, accounting for the three 140 MPa tests in Appendix E. The area contraction coefficient C_a cannot be estimated at this time because the literature used a reference nozzle. The literature value $C_a = 0.86$ [Pickett et al., 2011] is used for current estimation. The parameters a (in Eq. 5.3.6) and β (in Eq. 5.3.7) are given to be 0.66 and 105/52

respectively in [Pickett et al., 2011]. It is worthy to mention that these model include a modeling spray angle, which is bigger than the experimental observations found in this study, which is 13° . The literature model value (23°) is better fitted when conducting comparison. Flow velocity at the nozzle vicinity is therefore estimated as U_f in the above equations. The velocity is used in Sazhin [2014] model as well.

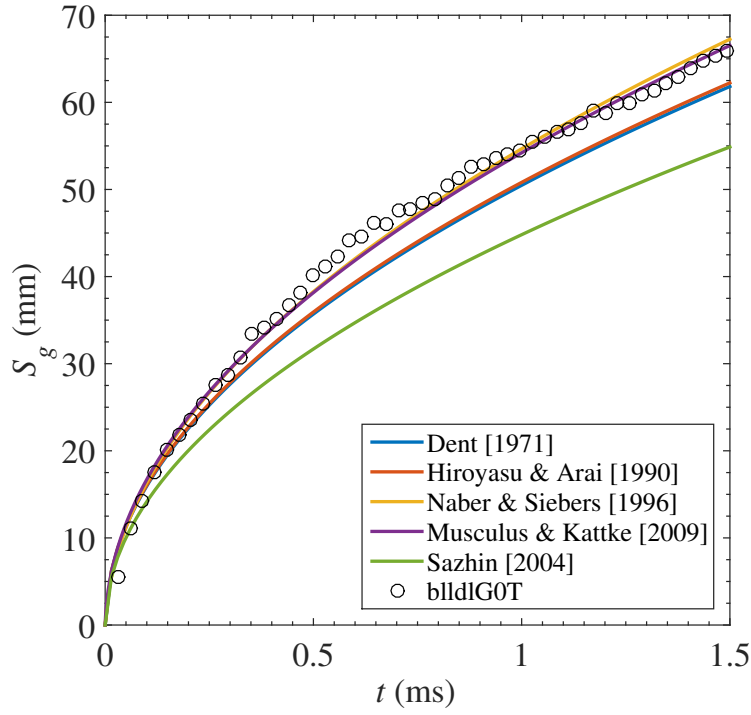


Figure 5.11: Vapor jet penetration compared with literatures, $P_{inj} = 140$ MPa, $T_{ch} = 850$ K, $\rho_{ch} = 22$ kg/m³, pure diesel.

The result of comparison can be summarized as follows:

- Previous experiments were done with diesel fuel, therefore only the diesel injection is compared here. From these observation, the observations here are consistent with the predictions in the literature. Agreements is evident.
- The models by Naber and Siebers [1996] and Musculus and Kattke [2009] are found to best match with the current data set.

- The mathematical form of Dent [1971] and Hiroyasu and Arai [1990] along with Sazhin [2014] are close and produce similar results.
- The equation produced by Naber and Siebers [1996] and Musculus and Kattke [2009] from their mixing-limited theorems produce almost the same results as shown by Pickett et al. [2011].
- Both Naber and Siebers [1996] and Musculus and Kattke [2009] also include adjustment parameters which allow one to make the curves fit better into the observed data.

5.3.2 Quasi-steady Jet Length and Jet Angle

The quasi-steady jet length depends highly on the fuel components. The current literature available for quasi-steady jet length studies is from Siebers [1998], Siebers [1999] and Higgins et al. [1999]. As is seen in the literature review chapter, Higgins et al. [1999] requires the heat capacity and mass fraction of each fuel component and employs fuel temperature, which is beyond the measurements of this study. The data can only be compared with their diesel fuel #2. Although there is no direct data available, Higgins et al. [1999] has a series of experiments done with varying density at an injection pressure of 140 MPa, a chamber temperature of 850 K and a nozzle diameter of 0.246 mm. The orifice diameter is twice as large as was used in this experiment. Higgins et al. [1999] and Siebers [1999] show that nozzle diameter varies linearly with the quasi-steady jet lengths. Therefore, the data from Higgins et al. [1999] can be directly compared by dividing them half, as shown in Fig. 5.12. The comparison shows a reasonable agreement between the experimental data of this study with the literature.

Unlike the jet penetration, jet angle is difficult to model due to the transient behavior at the beginning of fuel injection. In terms of literature models, nozzle

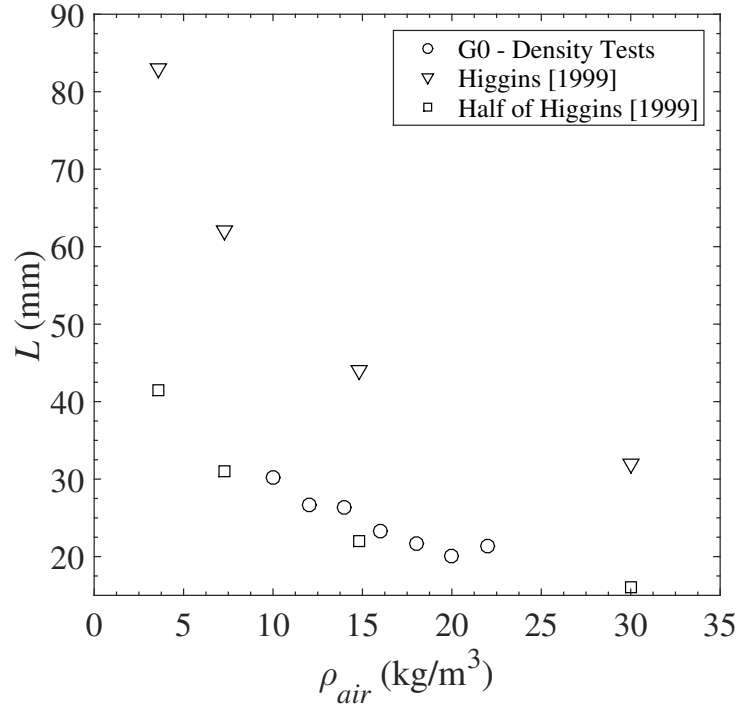


Figure 5.12: Quasi-steady liquid jet length comparison, $T_{ch} = 850$ K, $P_{inj} = 140$ MPa. Higgins et al. [1999] original data has an orifice size 0.246 mm, halved data represents a 0.123 mm nozzle.

aspect ratio, We number and Re number are usually required to solve the exact jet angle [Reitz and Bracco, 1979; Hiroyasu and Arai, 1990]. An approximation may be adapted to find the angle given in equation (2) of Reitz and Bracco [1979].

$$\tan \frac{\theta}{2} = 0.13 \left(1 + \frac{\rho_{ch}}{\rho_l} \right) \quad (5.3.8)$$

Eq. 5.3.8 equation predicts the jet angles to be around 15° under all experimental conditions from this study. However, it does not seem to be accurate enough for the current measurements. The experiments done by Siebers [1999], who is also the one established the jet angle definition used in this thesis, showed that background temperature and fuel type did not affect the jet angle. Siebers [1999] observed jet angles of range from 10° to 16° at chamber conditions of 3.6-30.2 kg/m³, 1000 K,

136 MPa and 246 mm nozzle. Siebers [1999] proposed the a correlation to predict jet angle:

$$\tan \frac{\theta}{2} = 0.26 \left[\left(\frac{\rho_{ch}}{\rho_l} \right)^{0.19} - 0.0043 \sqrt{\frac{\rho_l}{\rho_{ch}}} \right] \quad (5.3.9)$$

Eq. 5.3.9 (also shown in Eq. 2.2.10 of Chapter 1) applied to liquid jets only, since the experiments done by Siebers [1999] only observed the liquid jet. The equation predicts the angle to be 12° to 14° in the conditions of this study, as can be seen in Fig. 5.13. The jet angle shows better consistency in the high background density case (22 kg/m^3) than in the low background density case (10 kg/m^3). It is concluded that the jet angles in current study are more affected by the background gas densities compared with Siebers [1999].

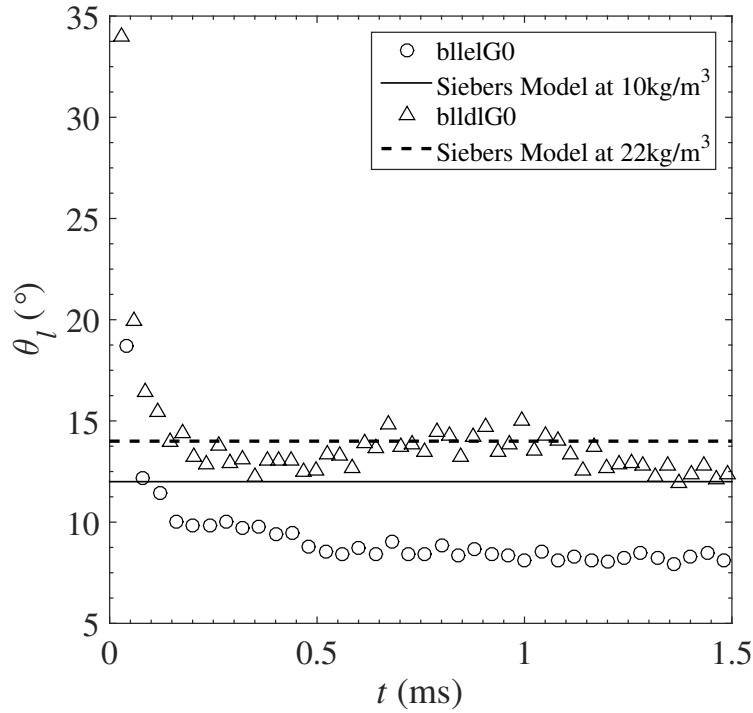


Figure 5.13: Comparison of liquid jet angle with Eq. 5.3.9 from Siebers [1999], at $\rho_{ch} = 10 \text{ kg/m}^3$ and 22 kg/m^3 , with $P_{inj} = 140 \text{ MPa}$, $T_{ch} = 850 \text{ K}$, on pure diesel.

CHAPTER 6

CONCLUSION

6.1 Summary

To study of the jet morphology of a diesel fuel injected into a constant pressure chamber focused shadowgraph and general shadowgraph flow visualization is used successfully. As the jet is injected, high speed images were collected and then analyzed. To understand the behavior of diesel fuel, three gasoline blend ratios: 0, 20% and 60% were used and then compared using image processing techniques. A constant volume combustion chamber with optical accessibility was used to mimic the engine in-cylinder condition. In addition to the fuel blend, three controllable independent output variables were altered in this study: chamber temperature, background gas density and injection pressure, and each varied, one at a time, and the jet characteristics of the liquid and vapor phases were studied using backlit shadowgraphy and focused shadowgraphy respectively. The captured images clearly showed the jet evolution over the recorded time. It was found that the liquid jets reached quasi-steady jet lengths once the chamber temperature is greater than 650 K, while the vapor jet images indicated that the evaporated fuel continued to penetrate throughout the chamber. The vapor jet behaviors were found to have a similar pattern compared with the non-evaporating liquid jets.

The jet penetration, jet area and jet angles calculated from the sequential time images for the three independent variables and for the three different fuels blends were calculated. The main results for jet penetration, jet area, jet angle and fuel blend are:

- The liquid and vapor jet penetration shows consistent temporal patterns and values. Vapor jet penetration at the most extreme chamber condition (chamber temperature 850 K, background gas density 22 kg/m³, injection pressure 140 MPa) is approximately 65 mm at 1.5 ms for the three fuel blends. Quasi-steady liquid jet penetrations at this condition are approximately 20 mm, 19 mm, 15 mm, for G0, G20, G60 fuel. The consistency is also seen in the jet area graphs, which show linear growth in vapor jets and non-evaporating liquid jets. As the injected jet grows, the liquid and vapor areas diverge, indicating the evaporation which is not visible. An example is found in Fig. 4.2b.
- Liquid jets and vapor jets are clearly distinguished by observing if the jet reaches a quasi-steady jet length at evaporating conditions. The quasi-steady jet length is found to be fitted with the first order LTI response function. The sensitivities are summarized in Table 5.1 and Table 5.2. The vapor jet penetration development (which never reaches a quasi-steady length) is found to scale with the $t^{1/2}$ rule, which is consistent with the literature. The vapor jet area is found to be linear as a function of time, which is close to self-similar. Detailed discussions are in Chapter 5.
- The jet behavior is not significantly affected by the injection pressure. In general, an increase of injection pressure increases the vapor jet penetration. No specific trend is observed in quasi-steady jet length or in jet angle as injection pressure is increased.

- An increase of background gas densities decreases the vapor jet penetration, quasi-steady jet length, and increases the jet angle. Usually vapor jet angle has the same trend as the liquid jet angle but is larger than the corresponding liquid jet.
- The chamber temperature has different effects, depending on if the jet is non-evaporating or evaporating. The temperature does not affect the non-evaporating jet penetration case. For the evaporating jet, the quasi-steady jet penetration length decreases as the temperature increases. For example, the quasi-steady jet length changes from 35 mm to 20 mm for the G60 case from a chamber temperature of 650 K to 550 K. For the vapor jet cases, the increase in temperature decreases the jet penetration.
- An increase of blended gasoline percentage greatly decreases the quasi-steady jet length. The increase in gasoline percentage does not affect the vapor jet temporal penetration or the jet angles.

6.2 Future Work

This work has resulted in a number of further research questions and recommendations to make the results and analysis even better. An investigation of the chamber background turbulence is a first step. Modern computational algorithms (e.g. WAVE model previous mentioned and implemented with KIVA code) usually requires the chamber turbulence intensity as an input of the model. Schlieren-like Videography as the most suitable non-intrusive technique could be combined with PIV cross-correlation algorithms to quantify the background motions. For example, the images in Fig. 6.1 show the small motions of the background over $263 \mu\text{s}$. Compared with the high speed jet, the background is almost stationary between two frames. This is why frame subtraction is effective. Background motion over multiple

frames is also discernable and could be quantified using a simple PIV algorithm, an 8×8 window would give the most movement vectors. However, the current study image resolution (128×456) is small which would results in small PIV windows. It is recommended for the future work that less zoom and full camera resolution be used to capture the chamber turbulence. Apart from the PIV cross-correlation algorithm, auto-correlations algorithm on the background structure scale can be measured. Turbulent energy spectrum can be estimated in the future study.

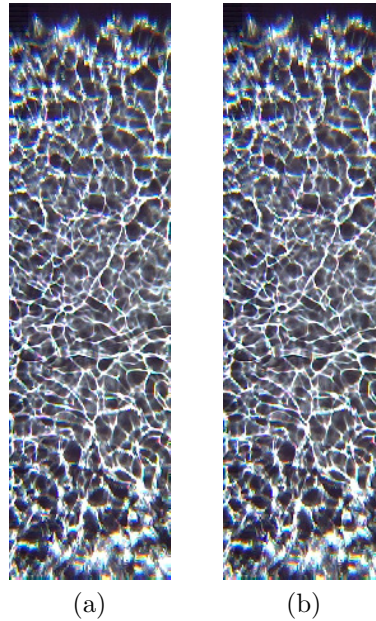


Figure 6.1: Pure background motions, interval of 9 frames or $263 \mu\text{S}$.

To further this work these steps are suggested,

- Improvement of the gas phase jet detection algorithm would allow quantitative discussion of vapor jet penetrations and jet angles.
- Study the actual combustion characters of dieseline fuel. Unlike the inert spray condition, an active burning jet is close to real engine conditions. Addition parameters like lift-off length (i.e. the jet length where combustion is started) can be visualized with shadowgraphy.

- Investigate the behavior of a supercritical diesel jet, using a preheated common-rail fuel inlet. Supercritical jet study is not yet fully understood. This may help resolving the current understanding of jet behavior. For instance, does this increase the spray angle or change the air/fuel mixing method?

REFERENCES

- Abramovich, G. (1963). *The Theory of Turbulent Jets*. The MIT Press, Cambridge, MA, USA.
- Anitescu, G. (2008). *Supercritical Fluid Technology Applied to the Production and Combustion of Diesel and Biodiesel Fuels*. PhD thesis, Syracuse University.
- Anitescu, G., Bruno, T. J., and Tavlarides, L. L. (2012). Dieseline for Supercritical Injection and Combustion in Compression-Ignition Engines: Volatility, Phase Transitions, Spray/Jet Structure, and Thermal Stability. *Energy & Fuels*, 26(10):6247–6258.
- Arcoumanis, C., Gavaises, M., and French, B. (1997). Effect of Fuel Injection Processes on the Structure of Diesel Sprays. In *SAE Technical Papers 970799*.
- Atassi, N., Borée, J., and Charnay, G. (1993). Transient behavior of an axisymmetric turbulent jet. *Applied Scientific Research*, 51(1-2):137–142.
- Austen, A. E. W. and Lyn, W.-T. (1960). Relation between fuel injection and heat release in a direct-injection engine and the nature of the combustion processes. *ARCHIVE: Proceedings of the Institution of Mechanical Engineers, Automobile Division 1947-1970*, 1960(1960):47–62.
- Bao, T.-t., Zhou, B., Deng, J., and Wu, Z.-j. (2014). Research on the physical property

- of diesel-gasoline blend fuel. *Journal of Shanghai Jiaotong University (Science)*, 19(6):721–727.
- Bardi, M., Payri, R., Malbec, L. M., Bruneaux, G., Pickett, L. M., Manin, J., Bazyn, T., and Genzale, C. (2012). Engine Combustion Network: Comparison of Spray Development, Vaporization, and Combustion in Different Combustion Vessels. *Atomization and Sprays*, 22(10):807–842.
- Batchelor, G. K. and Gill, a. E. (1962). Analysis of the stability of axisymmetric jets. *Journal of Fluid Mechanics*, 14(04):529.
- Borée, J., Atassi, N., and Charnay, G. (1996). Phase averaged velocity field in an axisymmetric jet subject to a sudden velocity decrease. *Experiments in Fluids*, 21(6):447–456.
- Borée, J., Atassi, N., Charnay, G., and Taubert, L. (1997). Measurements and image analysis of the turbulent field in an axisymmetric jet subject to a sudden velocity decrease. *Experimental Thermal and Fluid Science*, 14(1):45–51.
- Canny, J. F. (1986). A Computational Approach to Edge Detection. *IEEE Transactions on Pattern Analysis and Machine Intelligence*, 8(6):679–698.
- Crow, S. C. and Champagne, F. H. (1970). Orderly structure in jet turbulence. *Journal of Fluid Mechanics*, 48(03):547.
- Dent, J. C. (1971). A Basis for the Comparison of Various Experimental Methods for Studying Spray Penetration. In *SAE Paper 710571*, pages 1881–1884.
- Dernotte, J., Hespel, C., and Houill, S. (2012). Influence of Fuel Properties on the Diesel Injection Process in Nonvaporizing Conditions. *Atomization And Sprays*, 22(6):461–492.

- Desantes, J. M., Pastor, J. V., Payri, R., and Pastor, J. M. (2005). Experimental Characterization of Internal Nozzle Flow and Diesel Spray Behavior, Part II: Evaporative Conditions. *Atomization and Sprays*, 15(5):517–544.
- Eggers, J. and Villermaux, E. (2008). Physics of liquid jets. *Reports on Progress in Physics*, 71(3):036601.
- Ghaemi, S. (2009). *Investigation of Effervescent Atomization Using Laser-Based Measurement Techniques*. PhD thesis, University of Alberta.
- Giffen, E. and Muraszew, A. (1953). *The Atomisation of Liquid Fuels*. CHAPMAN & HALL LTD.
- Grant, R. P. and Middleman, S. (1966). Newtonian jet stability. *AIChE Journal*, 12(4):669–678.
- Haenlein, A. (1931). Disintegration of a Liquid Jet. Technical report, N.A.C.A Tech. Memo No. 659.
- Hariprasad, T. (2013). Effect of Injection Pressure on Performance of Dual Fuel Diesel Engine. In *SAE paper 2013-01-2887*.
- Hay, N. and Jones, P. L. (1972). Comparison of the Various Correlations for Spray Penetration. In *SAE paper 720776*.
- Higgins, B. S., Mueller, C. J., and Siebers, D. L. (1999). Measurements of fuel effects on liquid-phase penetration in DI sprays. *SAE transactions*, 108(724):630–643.
- Hiroyasu, H. and Arai, M. (1990). Structures of Fuel Sprays in Diesel Engines. In *SAE paper 900475*, number 412.

- Kokjohn, S. L., Hanson, R., Splitter, D., Kaddatz, J., and Reitz, R. (2011). Fuel Reactivity Controlled Compression Ignition (RCCI) Combustion in Light- and Heavy-Duty Engines. *SAE Int. J. Engines*, 4(1):360–374.
- Kook, S., Le, M. K., Padala, S., and Hawkes, E. R. (2011). Z-type Schlieren Setup and its Application to High-Speed Imaging of Gasoline Sprays. In *SAE Paper 2011-01-1981*.
- Kook, S. and Pickett, L. M. (2012). Liquid length and vapor penetration of conventional, Fischer-Tropsch, coal-derived, and surrogate fuel sprays at high-temperature and high-pressure ambient conditions. *Fuel*, 93:539–548.
- Lee, D. W. (1936). A Comparison of Fuel Sprays from Several Types of Injection Nozzles. Technical report, N.A.C.A. Report No. 520.
- Lee, D. W. and Spencer, R. C. (1933). Photomicrographic Studies of Fuel Sprays. Technical report, N.A.C.A. Report 454.
- Leermakers, C., Van den Berge, B., Luijten, C., Somers, L., de Goey, L., and Albrecht, B. (2011). Gasoline-Diesel Dual Fuel: Effect of Injection Timing and Fuel Balance. In *SAE Paper 2011-01-2437*.
- Li, X. (1995). Mechanism of Atomization of A Liquid Jet. *Atomization and Sprays*, 5(1):89–105.
- Liepmann, D. and Gharibs, M. (1992). The role of streamwise vorticity in the near-field entrainment of round jets. *Journal of Fluid Mechanics*, 245:643–668.
- Luijten, C. C. M. and Kurvers, C. (2010). Real Gas Effects in Mixing-Limited Diesel Spray Vaporization Models. *Atomization and Sprays*, 20(7):595–609.

- Ma, X., Zheng, L., Li, Y., Wang, Z., Xu, H., and Wang, J.-X. (2014). High Speed Imaging Study on the Spray Characteristics of Dieseline at Elevated Temperatures and Back Pressures. *SAE International Journal of Fuels and Lubricants*, 7(1):2014–01–1415.
- Ma, Y. J., Huang, R. H., Deng, P., and Huang, S. (2015). The development and application of an automatic boundary segmentation methodology to evaluate the vaporizing characteristics of diesel spray under engine-like conditions. *Measurement Science and Technology*, 26(4):045004.
- Marmottant, P. and Villermaux, E. (2004). On spray formation. *Journal of Fluid Mechanics*, 498:73–111.
- McCarthy, M. and Molloy, N. (1974). Review of stability of liquid jets and the influence of nozzle design. *The Chemical Engineering Journal*, 7(1):1–20.
- Michikawauchi, R., Tanno, S., Ito, Y., and Kanda, M. (2011). Combustion Improvement of Diesel Engine by Alcohol Addition - Investigation of Port Injection Method and Blended Fuel Method. *SAE International Journal of Fuels and Lubricants*, 4(1):2011–01–0336.
- Musculus, M. P., Miles, P. C., and Pickett, L. M. (2013). Conceptual models for partially premixed low-temperature diesel combustion. *Progress in Energy and Combustion Science*, 39(2-3):246–283.
- Musculus, M. P. B. (2009). Entrainment waves in decelerating transient turbulent jets. *Journal of Fluid Mechanics*, 638:117.
- Musculus, M. P. B. and Kattke, K. (2009). Entrainment Waves in Diesel Jets. *SAE International Journal of Engines*, 2(1):2009–01–1355.

- Myong, K., Arai, M., Suzuki, H., Senda, J., and Fujimoto, H. (2004). Vaporization Characteristics and Liquid-Phase Penetration for Multi-Component Fuels. In *SAE Paper 2004-01-0529*, volume 2004.
- Naber, J. and Siebers, D. L. (1996). Effects of Gas Density and Vaporization on Penetration and Dispersion of Diesel Sprays. In *SAE Technical Paper 960034*.
- Öz, I. H. (1969). Calculation of Spray Penetration in Diesel Engines. In *SAE paper 690254*.
- Park, S. H., Youn, I. M., Lim, Y., and Lee, C. S. (2013). Influence of the mixture of gasoline and diesel fuels on droplet atomization, combustion, and exhaust emission characteristics in a compression ignition engine. *Fuel Processing Technology*, 106:392–401.
- Parks, M. V., Polonski, C., and Toye, R. (1966). Penetration of Diesel Fuel Sprays in Gases. In *SAE paper 660747*.
- Pastor, J. V., Javier López, J., García, J. M., and Pastor, J. M. (2008). A 1D model for the description of mixing-controlled inert diesel sprays. *Fuel*, 87(13-14):2871–2885.
- Pastor, J. V., Payri, R., Garcia-oliver, J. M., and Nerva, J.-g. (2012). Schlieren Measurements of the ECN-Spray A Penetration under Inert and Reacting Conditions. *SAE Technical Paper*, (2012-01-0456).
- Payri, R., García-Oliver, J. M., Bardi, M., and Manin, J. (2012). Fuel temperature influence on diesel sprays in inert and reacting conditions. *Applied Thermal Engineering*, 35(1):185–195.
- Pei, Y., Davis, M. J., Pickett, L. M., and Som, S. (2015). Engine Combustion Network

- (ECN): Global sensitivity analysis of Spray A for different combustion vessels. *Combustion and Flame*, 162(6):2337–2347.
- Pickett, L. M., Kook, S., and Williams, T. C. (2009). Visualization of Diesel Spray Penetration , Cool-Flame , Ignition , High- Temperature Combustion , and Soot Formation Using High-Speed Imaging. *SAE Int. J. Engines*, 2(1):439–459.
- Pickett, L. M., Manin, J., Genzale, C. L., Siebers, D. L., Musculus, M. P. B., and Idicheria, C. a. (2011). Relationship Between Diesel Fuel Spray Vapor Penetration/Dispersion and Local Fuel Mixture Fraction. *SAE International Journal of Engines*, 4(1):2011–01–0686.
- Pickett, L. M., Manin, J., Payri, R., Bardi, M., and Gimeno, J. (2013). Transient Rate of Injection Effects on Spray Development. In *SAE Paper 2013-24-0001*, pages 15–16.
- Pope, S. B. (2000). *Turbulent Flows*. Cambridge University Press, Cambridge, UK.
- Rayleigh, L. (1878). On the Instability of Jets. In *Proceedings of the London mathematical society*, pages 4–13.
- Reitz, R. D. and Bracco, F. B. (1979). On the Dependence of Spray Angle and Other Spray Parameters on Nozzle Design and Operating Conditions. In *SAE Paper 790494*.
- Reitz, R. D. and Bracco, F. V. (1982). Mechanism of atomization of a liquid jet. *Physics of Fluids*, 25(10):1730–1742.
- Reitz, R. D. and Duraisamy, G. (2015). Review of high efficiency and clean reactivity controlled compression ignition (RCCI) combustion in internal combustion engines. *Progress in Energy and Combustion Science*, 46:12–71.

- Sandia (2011). Schlieren Image Contour Extraction Code. <http://www.sandia.gov/ecn/code.php>. [Online; accessed 02-June-2016].
- Sazhin, S. (2014). *Droplets and Sprays*. Springer, Germany.
- Schweitzer, P. H. (1937). Mechanism of Disintegration of Liquid Jets. *Journal of Applied Physics*, 8(8):513.
- Seebald, P. and Sojka, P. (2011). Supercritical and transcritical injection. In Ashgriz, N., editor, *Handbook of Atomization and Sprays*, chapter 11, pages 255–261. Springer, Springer New York Dordrecht Heidelberg London.
- Settles, G. S. (2001). *Schlieren and Shadowgraph Techniques*. Springer, Germany.
- Siebers, D. L. (1998). Liquid-Phase Fuel Penetration in Diesel Sprays. *SAE Technical Paper 980809*, (724).
- Siebers, D. L. (1999). Scaling Liquid-Phase Fuel Penetration in Diesel Sprays Based on Mixing-Limited Vaporization. *SAE technical paper 1999-01-0528*, (724).
- Smallwood, G. J. and Gülder, O. L. (2000). Views on the Structure of Transient Diesel Sprays. *Atomization And Sprays*, 10:355–386.
- Splitter, D. a., Hanson, R., Kokjohn, S. L., and Reitz, R. D. (2011). Reactivity Controlled Compression Ignition (RCCI) Heavy-Duty Engine Operation at Mid- and High-Loads with Conventional and Alternative Fuels. *SAE Technical Paper Series*, 1(Ci):0363.
- Tanaka, T., Ando, A., and Ishizaka, K. (2002). Study on pilot injection of DI diesel engine using common-rail injection system. *JSAE Review*, 23(3):297–302.
- Tennekes, H. and Lumley, J. (1972). *A First Course In Turbulence*. The Massachusetts Institute of Technology.

- Turner, D., Tian, G., Xu, H., Wyszynski, M. L., and Theodoridis, E. (2009). An Experimental Study of Dieseline Combustion in a Direct Injection Engine. In *SAE Paper 2009-01-1101*.
- Varde, K. S. and Popa, D. M. (1983). Diesel Fuel Spray Penetration at High Injection Pressures. In *SAE Paper 830448*.
- Versaevel, P., Motte, P., and Wieser, K. (2000). A New 3D Model For Vaporizing Diesel Sprays Based on Mixing-Limited Vaporization. In *SAE Paper 2000-01-0949*.
- Zhang, F., Xu, H., Zeraati Rezaei, S., Kalghatgi, G., and Shuai, S.-J. (2012). Combustion and Emission Characteristics of a PPCI Engine Fuelled with Dieseline. In *SAE Paper 2012-01-1138*.

APPENDIX A

APPENDIX A: EXPERIMENT DATA SUMMARY

The experiment chart is shown in this section. The chart is arranged with chronological order. The cases are named using the following conventions, and this kind of convention is adapted from the code by Sandia [2011].

- First character **b** means inert gas environment.
- Second character means the chamber temperatures, with **v** is 300 K, **u** is 350 K, **r** is 450 K, **x** is 550 K, **p** is 650 K, **n** is 750 K, **l** is 850 K.
- Third character means the background gas densities, with **e** is 10 kg/m³, **g** is 12 kg/m³, **h** is 14 kg/m³, **m** is 16 kg/m³, **s** is 18 kg/m³, **x** is 20 kg/m³, **l** is 22 kg/m³.
- Fourth character means the injection pressures, with **i** is 80 MPa, **h** is 90 MPa, **l** is 100 MPa, **g** is 110 MPa, **f** is 120 MPa, **e** is 130 MPa, **d** is 140 MPa.
- Fifth character **l** means the nozzle orifice is 0.12 mm.
- Each cases contains 3 separate injection events, to identify each test, the numbers 001, 002 or 003 are inserted after the 5 characters, e.g. buldl001G0.
- **G0**, **G20**, **G60** means the gasoline blended ratio is 0%, 20% or 60%.

- Character after the fuel type, means the highest condition (850 K, 22 kg/m³ and 140 MPa) is conducted in which parameter variation run. **T** means chamber temperature variation, **D** means density variation, **P** means injection pressure variation, e.g. blldlG0T, the highest condition is reached by temperature increment run.

Case	T_{ch} (C) °C	T_{ch} (K) K	P_{ch} (MPa) MPa	ρ_{ch} (kg/m ³) kg/m ³	P_{inj} (MPa) MPa	Fuel
buldlG0	27	300	1.98	22.22	140	G0
bvldlG0	77	350	2.32	22.32	140	G0
brldlG0	177	450	3.02	22.60	140	G0
bxldlG0	276	549	3.64	22.32	140	G0
bpldlG0	375	648	4.43	23.02	140	G0
bnldlG0	478	751	5.09	22.82	140	G0
blldlG0T	572	845	5.63	22.43	140	G0
bledlG0	577	850	2.64	10.46	140	G0
blgdlG0	575	848	3.11	12.35	140	G0
blhdlG0	582	855	3.60	14.18	140	G0
blmdlG0	575	848	4.12	16.36	140	G0
blsdlG0	583	856	4.60	18.09	140	G0
blxdlG0	577	850	5.09	20.17	140	G0
blldlG0D	578	851	5.52	21.84	140	G0
blldlG0	579	852	5.63	22.25	80	G0
blldlG0	573	846	5.42	21.58	90	G0
blldlG0	583	856	5.57	21.91	100	G0
blldlG0	579	852	5.61	22.17	110	G0
blldlG0	574	847	5.65	22.47	120	G0
blldlG0	577	850	5.62	22.27	130	G0
blldlG0P	575	848	5.59	22.20	140	G0
buldlG20	25	298	1.90	21.47	140	G20
brldlG20	273	546	3.59	22.14	140	G20
bxldlG20	181	454	2.88	21.36	140	G20
bpldlG20	376	649	4.27	22.16	140	G20
bnldlG20	473	746	4.97	22.44	140	G20
blldlG20T	572	845	5.59	22.28	140	G20
bledlG20	575	848	2.62	10.41	140	G20

Table A.1: Experiment cases: summary, 3 injections of each.

Case	T_{ch} (C) °C	T_{ch} (K) K	P_{ch} (MPa) MPa	ρ_{ch} (kg/m ³) kg/m ³	P_{inj} (MPa) MPa	Fuel
blfdlG20	574	847	3.18	12.64	140	G20
bledlG20	578	851	3.61	14.29	140	G20
bledlG20	572	845	3.98	15.86	140	G20
bledlG20	573	846	4.61	18.35	140	G20
bledlG20	575	848	5.03	19.98	140	G20
blldlG20D	575	848	5.49	21.80	140	G20
blldlG20	571	844	5.50	21.95	80	G20
blldlG20	579	852	5.53	21.86	90	G20
blldlG20	573	846	5.69	22.65	100	G20
bvldlG20	77	350	2.31	22.23	140	G20
blldlG20	563	836	5.37	21.63	110	G20
blldlG20	584	857	5.60	22.01	120	G20
blldlG20	568	841	5.51	22.06	130	G20
blldlG20P	570	843	5.53	22.09	140	G20
brldlG60	177	450	3.00	22.45	140	G60
bxldlG60	278	551	3.74	22.86	140	G60
bpldlG60	373	646	4.26	22.21	140	G60
bnldlG60	474	747	4.99	22.50	140	G60
blldlG60T	573	846	5.74	22.85	140	G60
bledlG60	580	853	2.68	10.58	140	G60
blldlG60	590	863	3.13	12.21	140	G60
blldlG60	578	851	3.72	14.72	140	G60
blldlG60	580	853	4.12	16.27	140	G60
blldlG60	580	853	4.63	18.28	140	G60
blldlG60	577	850	5.18	20.52	140	G60
blldlG60D	575	848	5.55	22.04	140	G60
blldlG60	577	850	5.65	22.39	130	G60
blldlG60	585	858	5.76	22.61	80	G60
blldlG60	574	847	5.63	22.39	90	G60
blldlG60	570	843	5.71	22.81	100	G60
blldlG60	570	843	5.52	22.05	110	G60
blldlG60	585	858	5.65	22.18	120	G60
blldlG60P	580	853	5.60	22.11	140	G60
bulldlG60	31	304	1.97	21.82	140	G60
bvldlG60	77	350	2.34	22.52	140	G60

Table A.2: Experiment cases: summary, 3 injections of each.

APPENDIX B

APPENDIX B: LIQUID JET CODE DOCUMENTATION

The liquid jet processing program is built with Matlab, and it is explained as follows,

- data were read directly from the high speed camera output (.cine file), therefore the images are 12 bits, which gives much more margins to threshold compared with 8 bits jpeg/png formats.
- image subtraction is always done with the first image ($i - 1$), where the jet does not come out yet.
- the code is divided into these parts:

liquidmain: the main code to run the process and plot the data.

readcin90: a code developed by Sandia Lab to read the Phantom high speed camera images directly, adapted here for loading images.

readandsort: read the folder that contains all the T_{ch} , ρ_{ch} and P_{inj} . data, sort them in a defined order to process.

filenameExtract: identify the file naming rule and output the experiment condition.

imageProcess: conduct the main imaging processing algorithm.

measureJet: a code developed by Sandia Lab to give spray angle, spray penetration and spray area of the processed binary jet images. Definitions used from the Sandia [2011] but adapted to output the results.

- the main constraints used to process are as follows:

Centerline. Jet centerline is found as the peak of greyscale of jet cross-section in the first 50 pixels, before the jet gets very turbulent and bent by vortices.

Nozzle exit or start of jet. By observing the first image, it is determined that the sharp (local maxima) change from nozzle (black) to background (white) is the nozzle exit.

Mask. Images are masked with polygon enclosed area. The mask starts with two pixels behind the nozzle exit coordinate, with a 90 degree (which is much greater than the spray angle) expansion reaching the upper and lower end of the images, and ignore the last 10 percent of the image (because it reaches the combustion chamber optical window).

Filtering. When finding the end of injection, Gaussian kernel filters are used to suppress the noise, but when doing the FWHM edge detection, the filter is not used.

End of injection. Signal-noise-ratio (SNR) is set to 3 in this case. The noise is defined as the average of whatever is not part of the jet. These exist an sequential problem since the SNR used is from previous images, which assumes the background noise level does not change quickly. The end of the jet is therefore found as the local maxima of greyscale gradient plot, where the point has SNR greater than 3. The local maxima also has to be greater than 50 % of highest greyscale gradient. The greyscale gradient plot is generated from

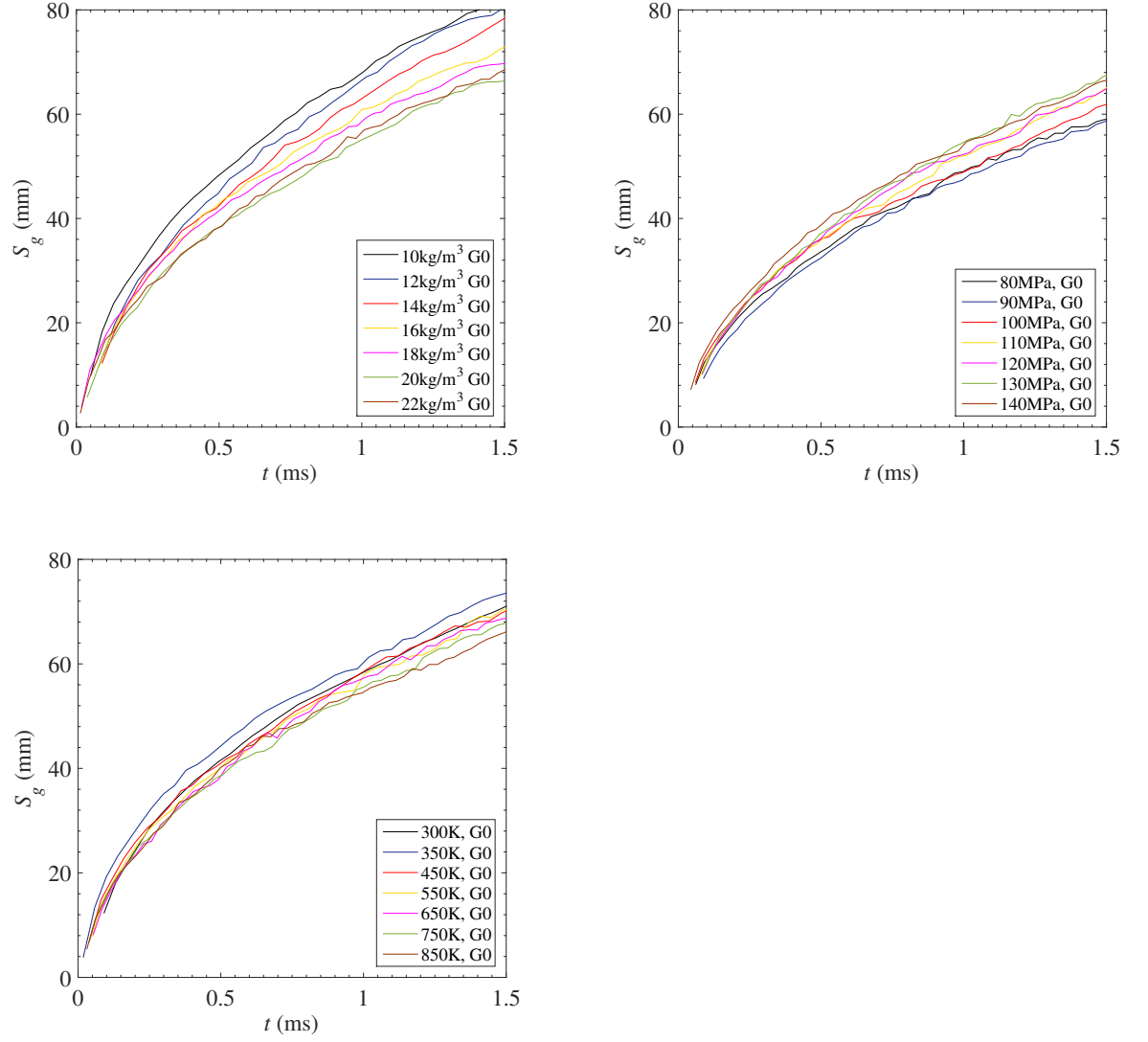
the maximum greyscale plot of each column along the longitudinal direction.

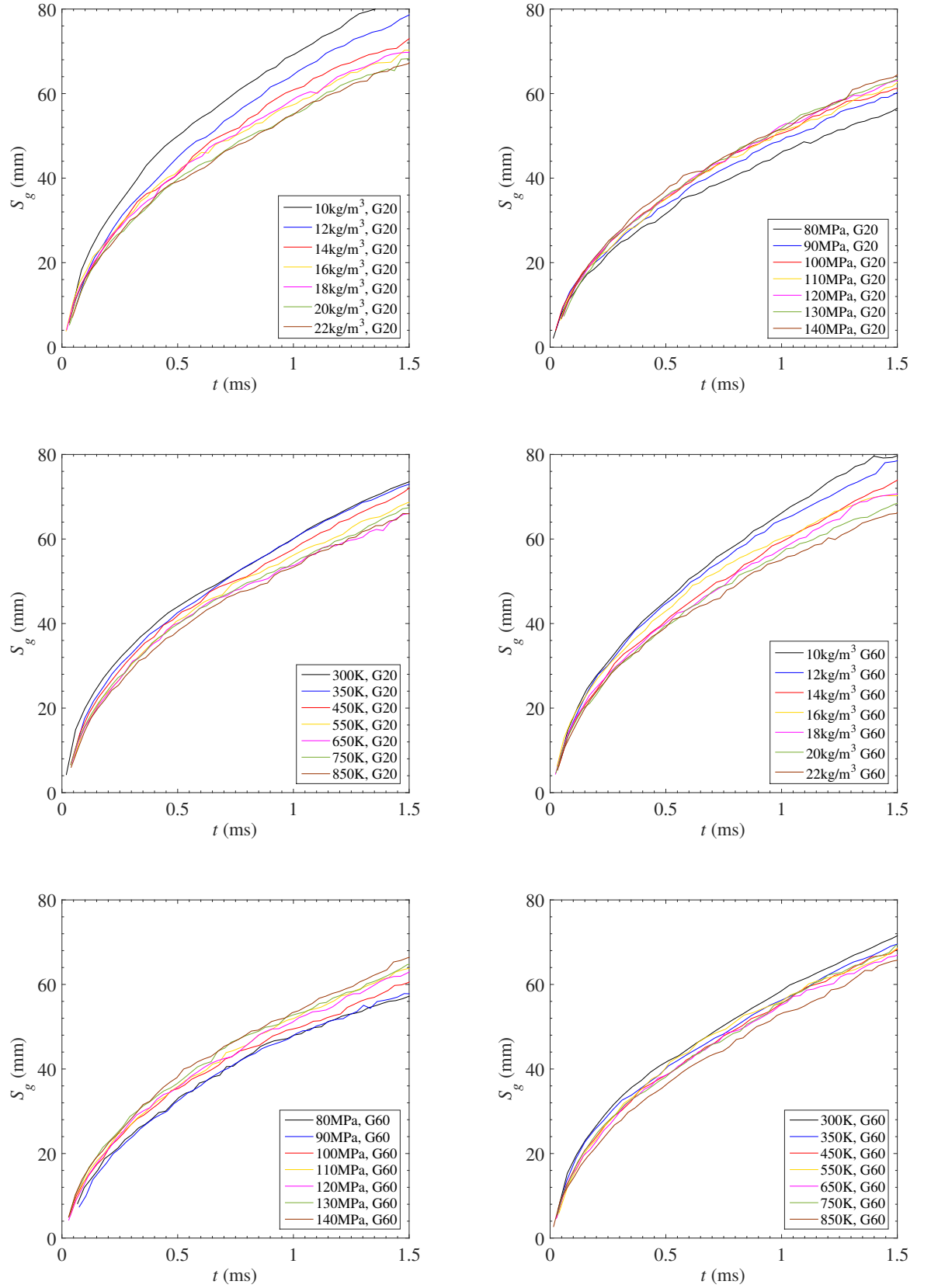
For the jet measurement algorithm, the code detects the binary images for jet region and use geometry commands to measure the jet. To find the jet spray angle and penetration, an iterative definition is implemented in the code. The code is tolerant to noise regions downstream away from the jet, but can be easily affect by noise upstream close to the nozzle exit.

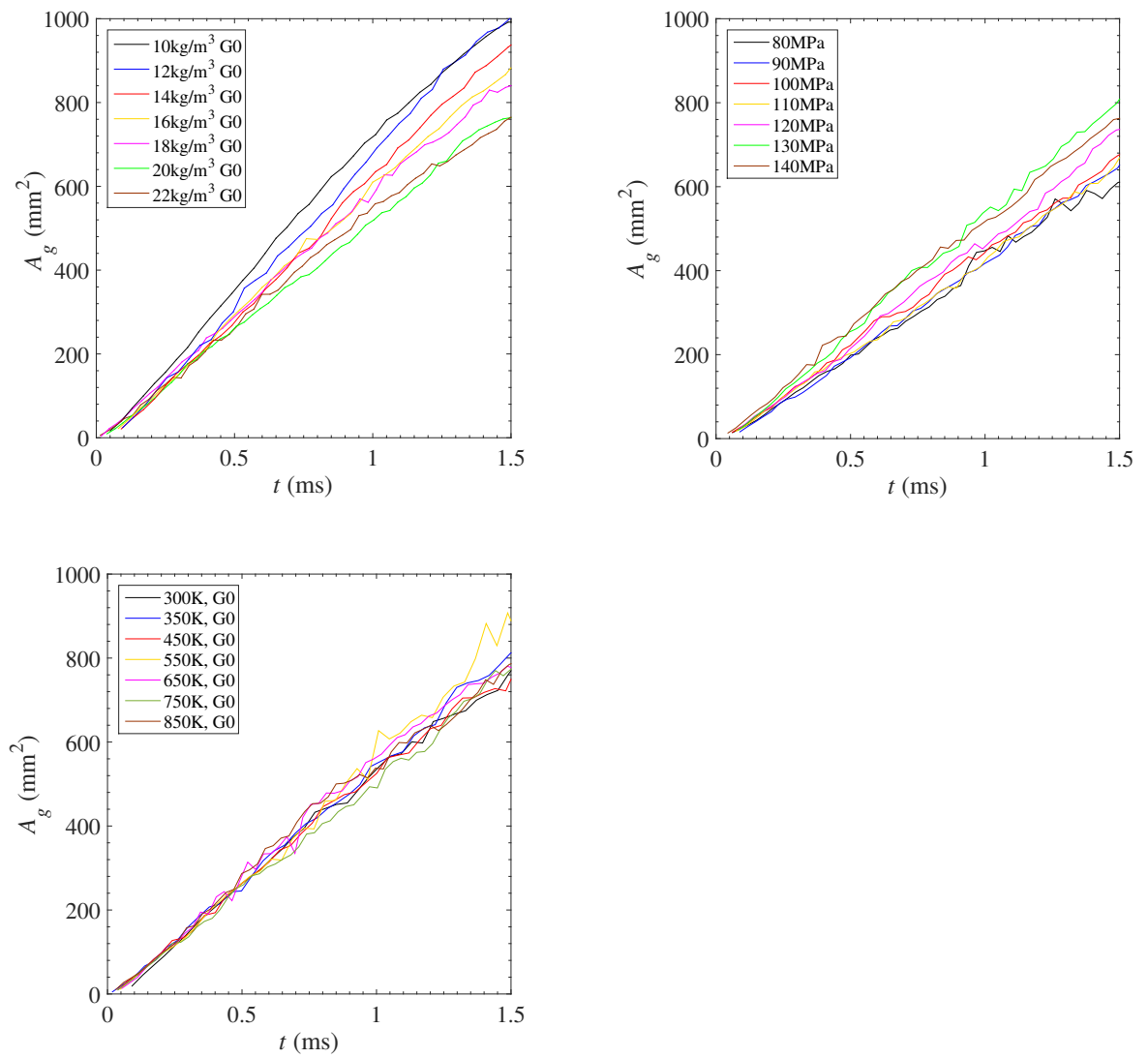
Conclusion: The image edge detection algorithm are often refer to Canny [1986]. Canny's method has intensive signal filtering and with multi-directional detection. Canny proposed the following 4 parameters to control what the algorithm did, and with proper threshold input values, his method generates edges very close to what human eye can see. This is why his algorithm is used to see if the code used here is generating good jet contours. The new algorithm is detecting less noise compared with Canny [1986]. The completeness of the jet is an issue for either the code or Canny's. For code used here, a fix SNR is introduced, but perhaps adaptive SNR should be developed in the future. In the noise filtering, the new code only use a simple tool to remove small noise from the binary images. A more advanced method like orientation-based and aspect-ratio-based filter may be required if the noise is an issue in the future.

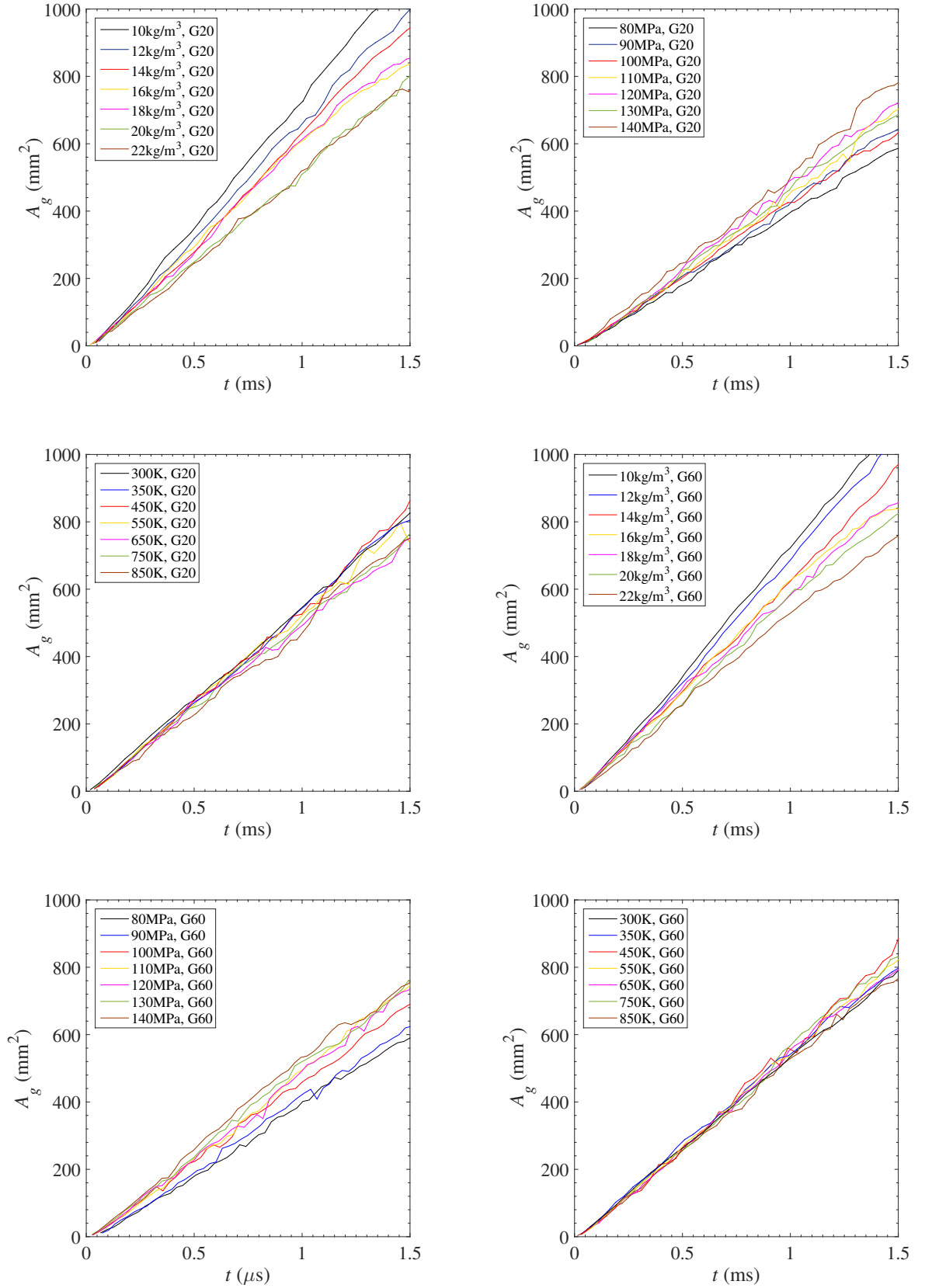
APPENDIX C

APPENDIX C: PLOTS FOR COMPLETE DATA SET

Figure C.1: Vapor penetration S on G0 fuel.

Figure C.2: Vapor penetration S on G20 & G60 fuel.

Figure C.3: Vapor area A on G0 fuel.

Figure C.4: Vapor area A on G20 & G60 fuel.

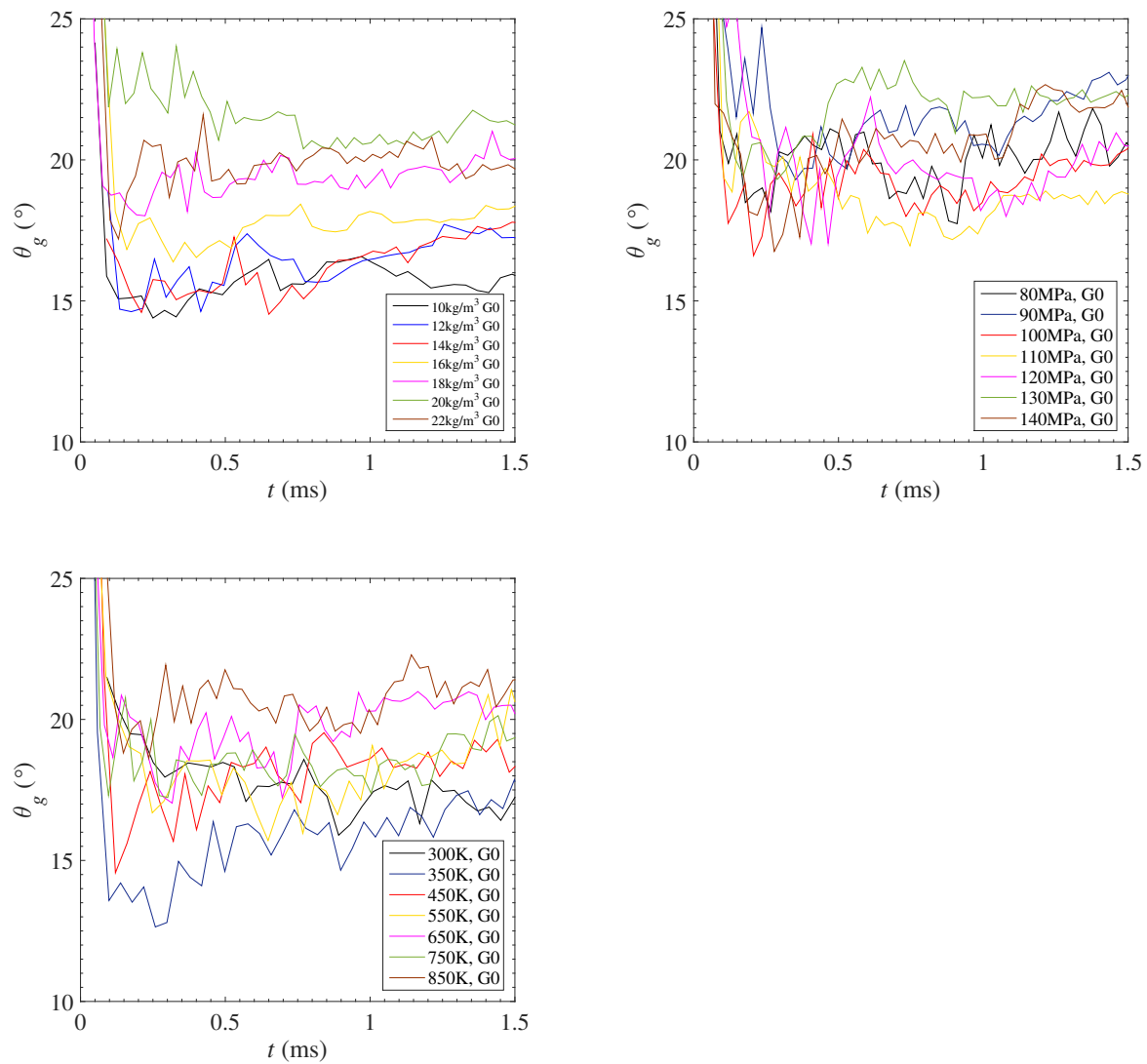
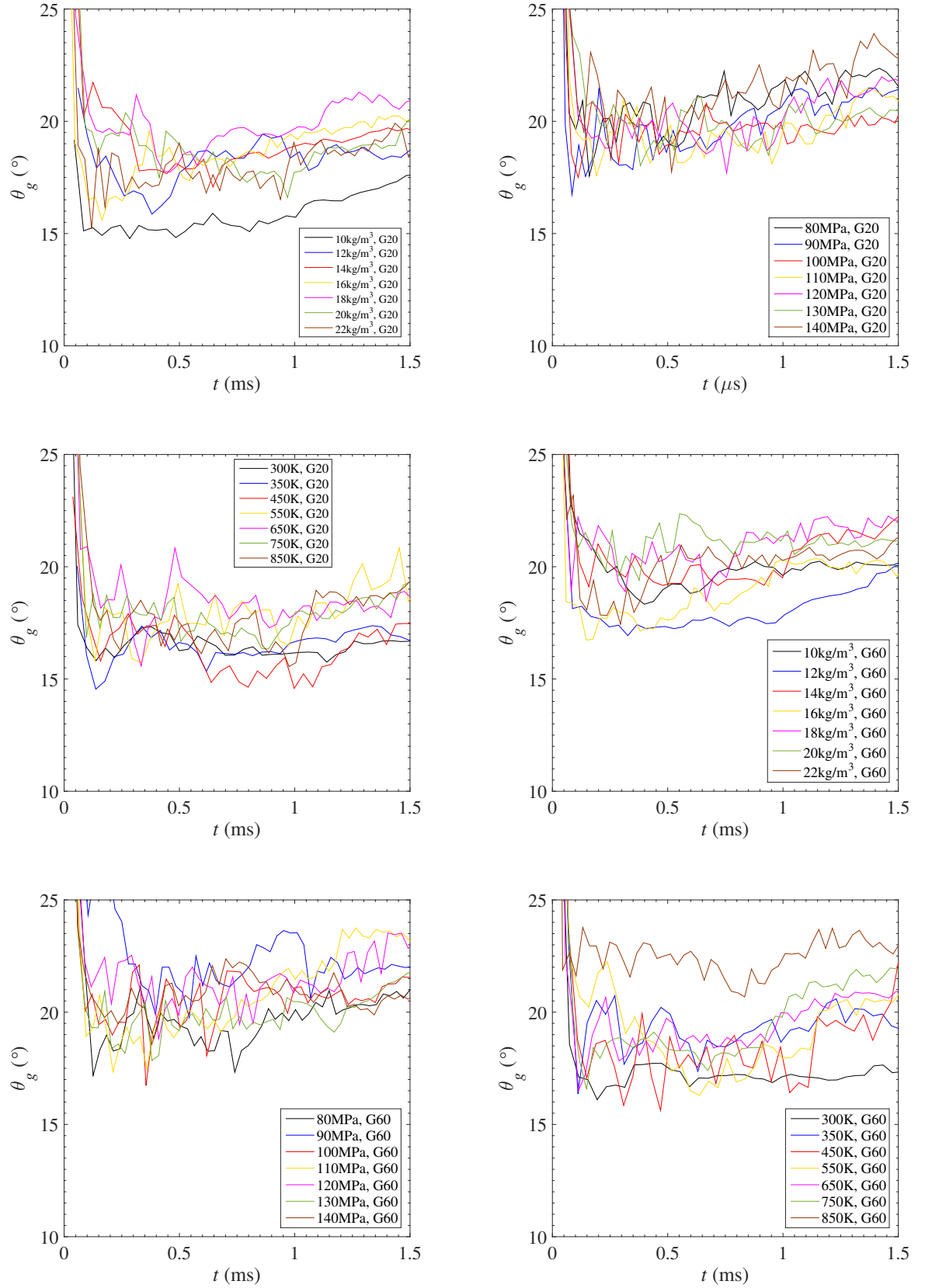
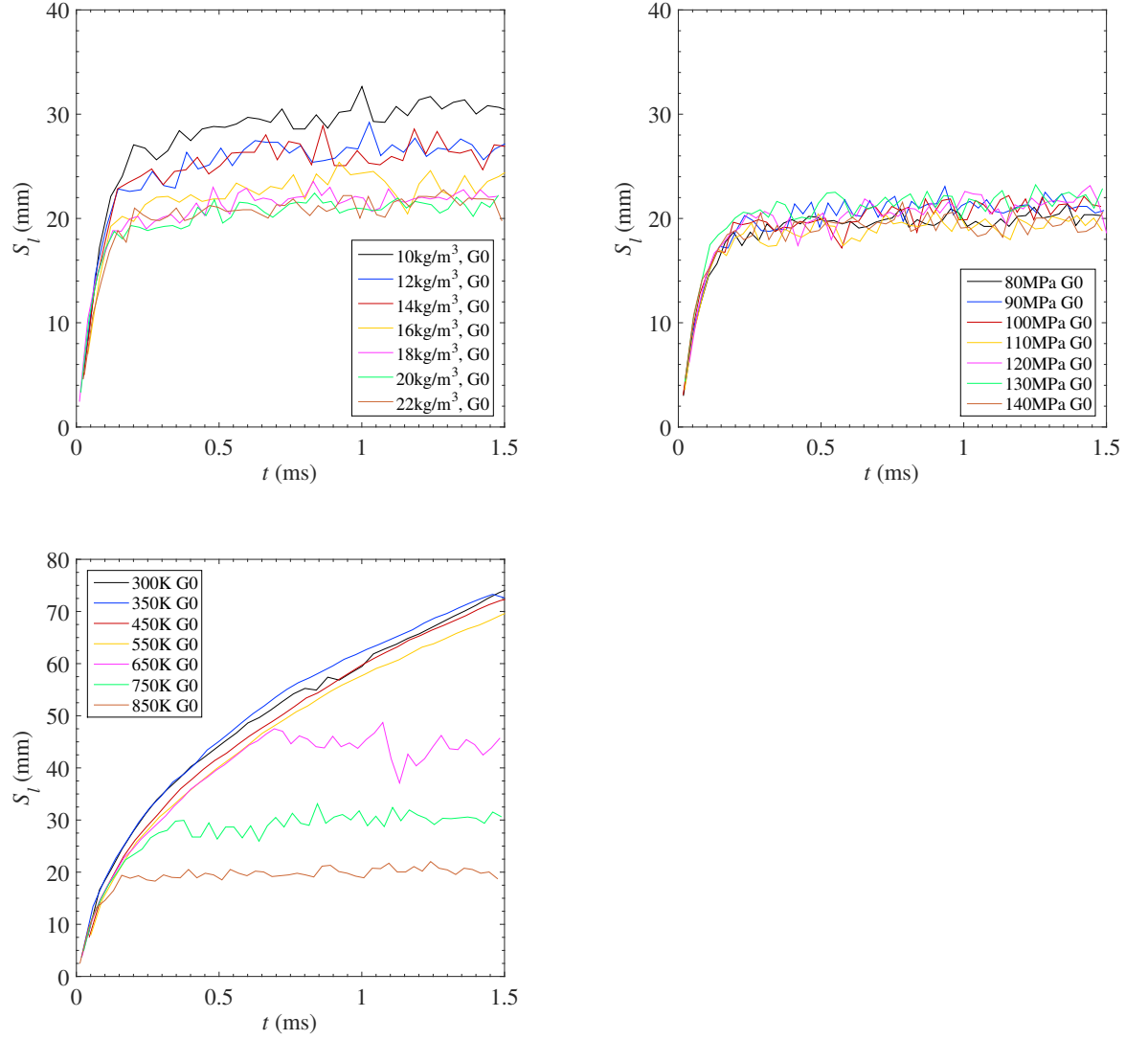
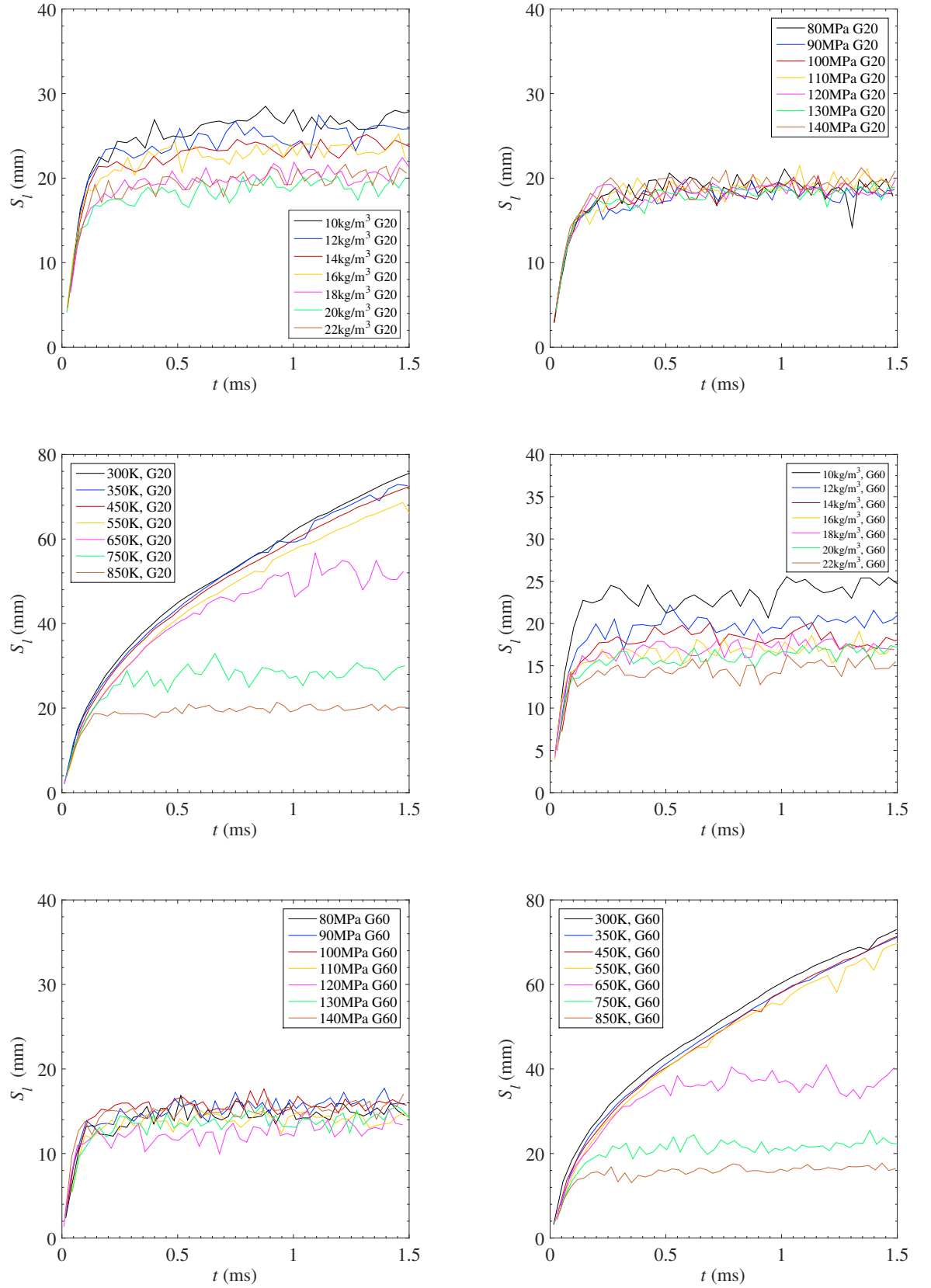
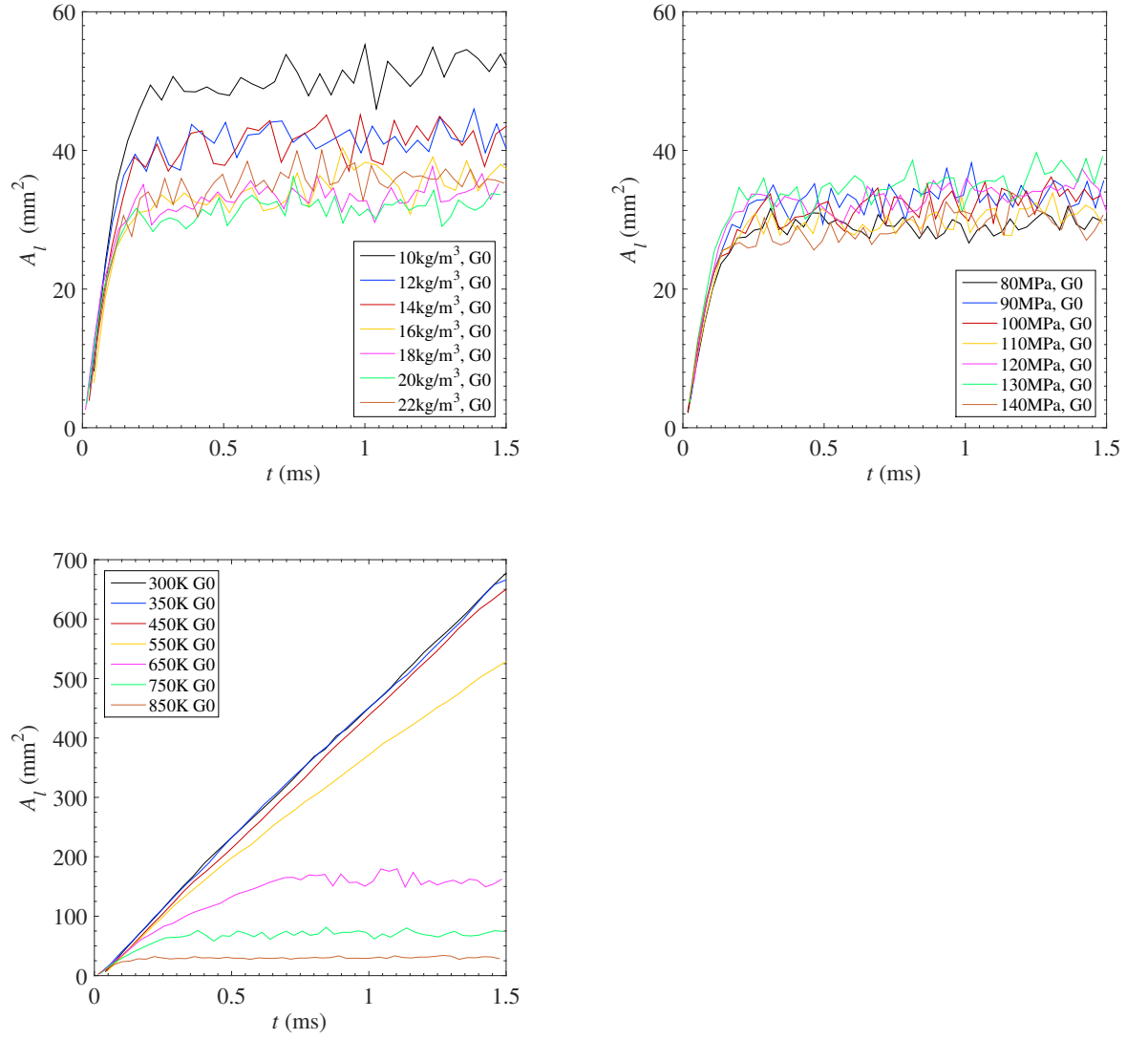


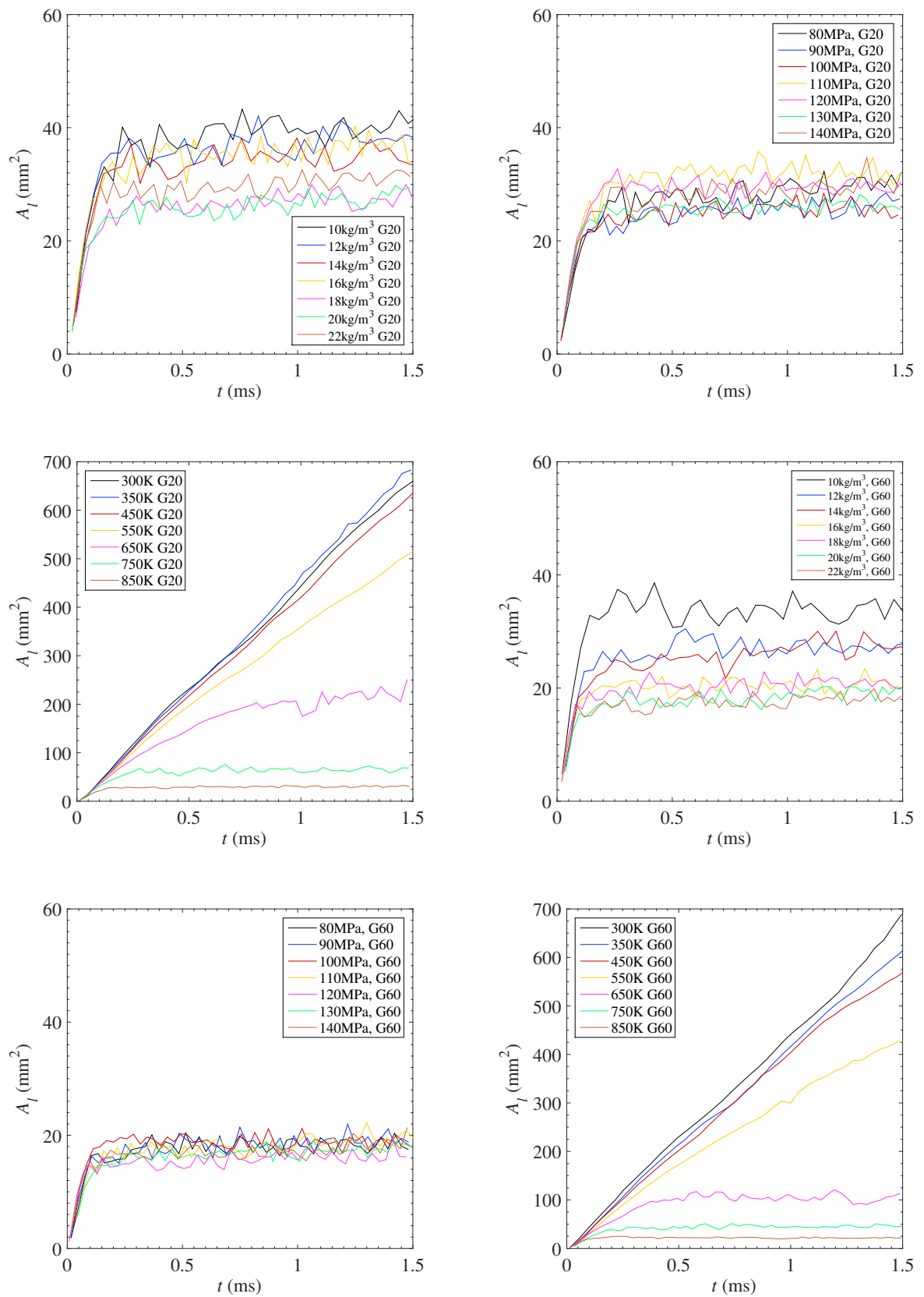
Figure C.5: Vapor jet angle θ on G0 fuel.

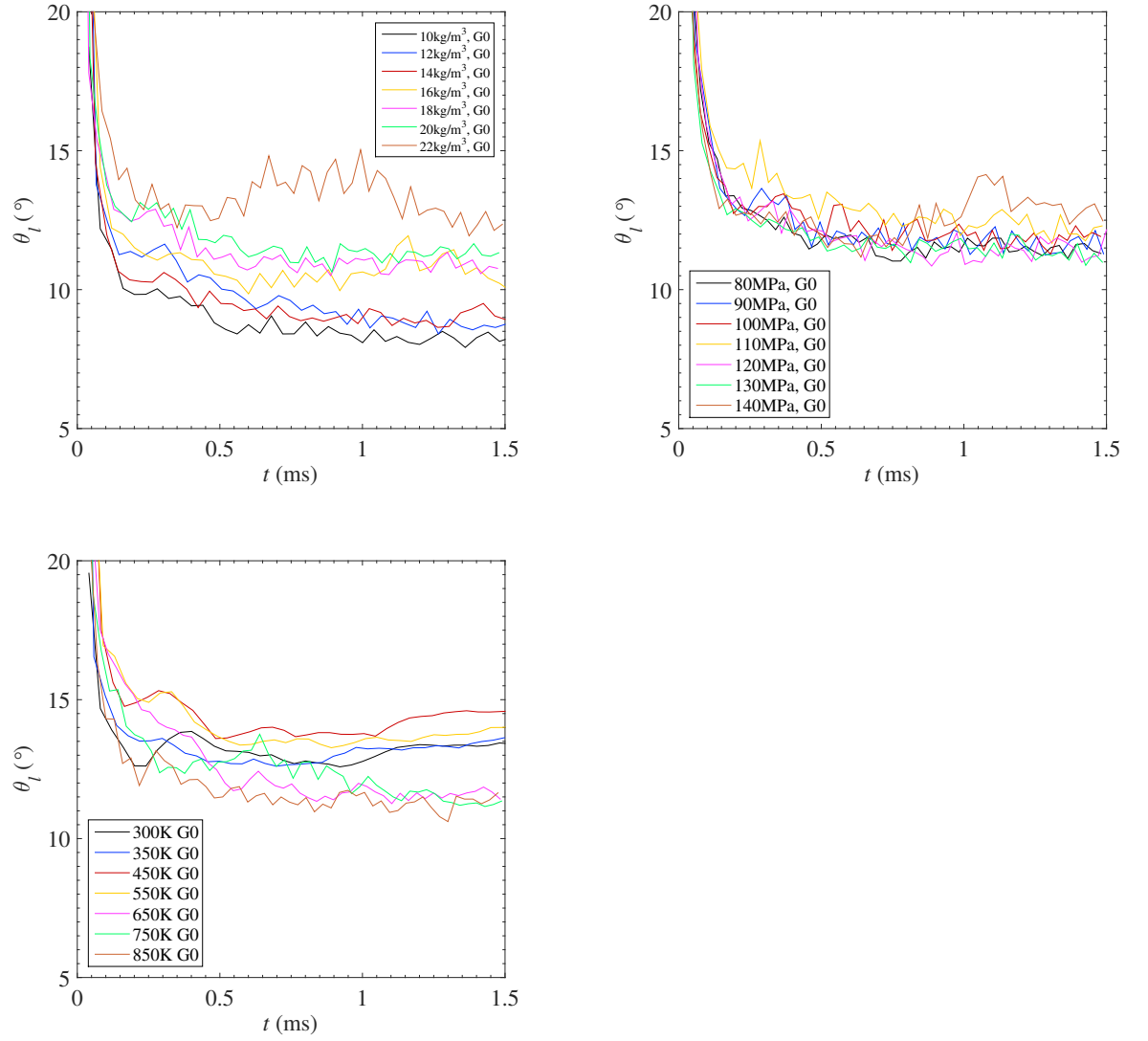
Figure C.6: Vapor jet angle θ on G20 & G60 fuel.

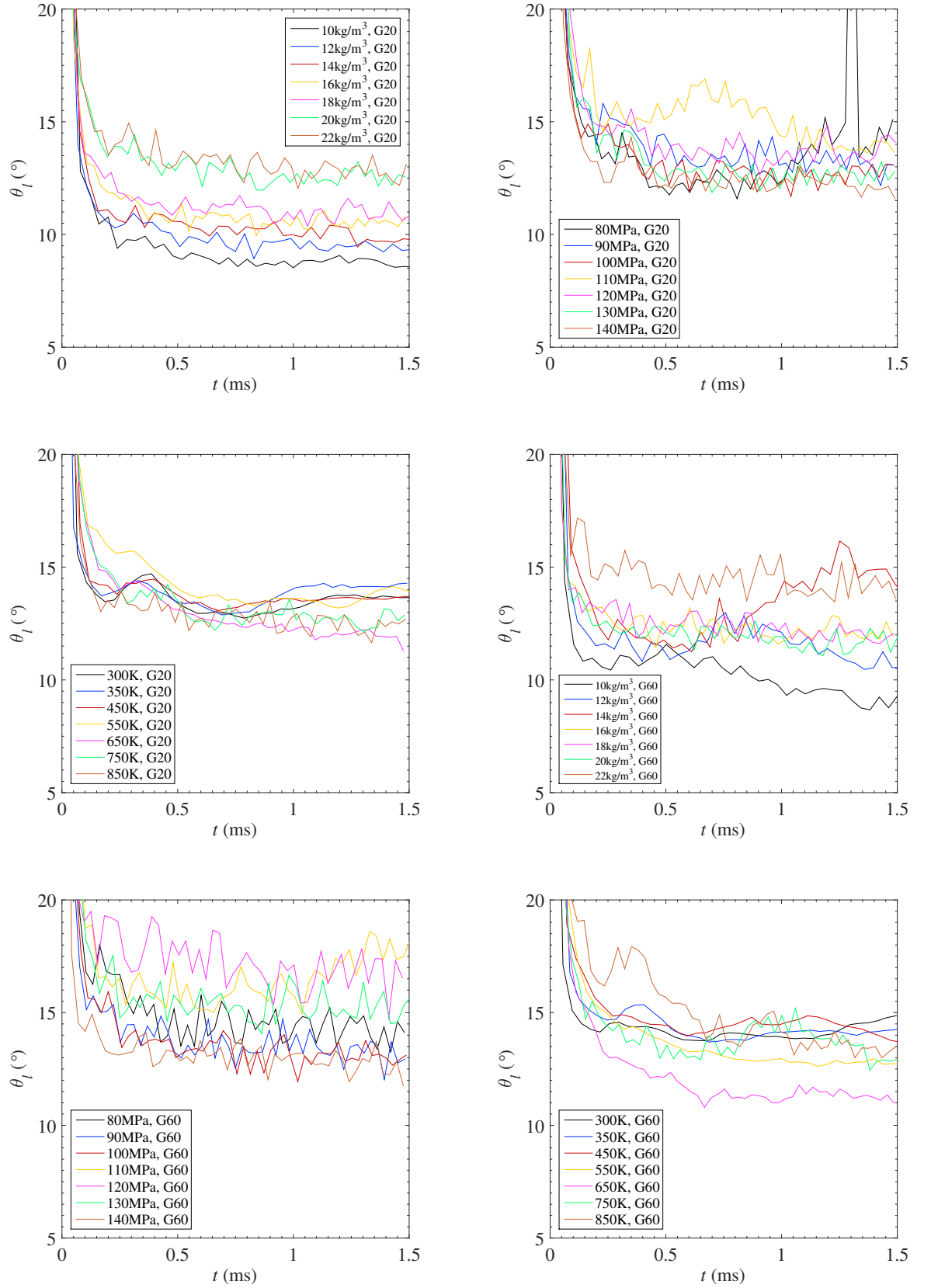
Figure C.7: Liquid penetration S on G0 fuel.

Figure C.8: Liquid penetration S on G20 & G60 fuel.

Figure C.9: Liquid area A on G0 fuel.

Figure C.10: Liquid area A on G20 & G60 fuel.

Figure C.11: Liquid jet angle θ on G0 fuel.

Figure C.12: Liquid jet angle θ on G20 & G60 fuel.

APPENDIX D

APPENDIX D: TEMPERATURE CALIBRATION

The serial number for thermocouple is WRNK-101 manufactured in China. Position of thermocouple is listed as,

- T_{probe1} is the thermocouple close to nozzle.
- T_{probe2} is the thermocouple in the middle.
- T_{probe3} is the thermocouple close to heater.

P_{ch} MPa	T_{ch} K	T_{ch} °C	T_{probe1} °C	T_{probe2} °C	T_{probe3} °C
2.5	500	230	249	251	252
2.5	700	430	472	472	472
2.5	900	630	660	670	693
3.5	500	230	243	241	240
3.5	700	430	444	445	450
3.5	900	630	655	660	673
4.5	500	230	247	246	247
4.5	700	430	447	449	453
4.5	900	630	646	648	667
5.5	500	230	231	230	230
5.5	700	430	438	440	443
5.5	900	630	640	643	660

Table D.1: Thermocouple temperature calibration.

The T_{ch} readings are exact because readings are taken when the wall thermocouple reaches the target temperature. From the derivation table, it can be seen that highest error can be occurring at low chamber pressure and high chamber temperature case. With higher pressure, the differences can be negated.

P_{ch} MPa	T_{ch} K	ΔT_{probe1} K	ΔT_{probe2} K	ΔT_{probe3} K
2.5	500	19	21	22
2.5	700	42	42	42
2.5	900	30	40	63
3.5	500	13	11	10
3.5	700	14	15	20
3.5	900	25	30	43
4.5	500	17	16	17
4.5	700	17	19	23
4.5	900	16	18	37
5.5	500	1	0	0
5.5	700	8	10	13
5.5	900	10	13	30

Table D.2: Derivation table.

APPENDIX E

APPENDIX E: INJECTION RATE

Injection rate profile is shown in Fig. E.1, with conditions in the captions. The testings are done with the EFS fuel injection rate testing machine in the Engine Labs, Beijing Institute of Technology. The machine is an accurate setup that is filled with diesel fuel in its chamber and creates a desired back pressure. Diesel fuel from the injector is injected into the pressure chamber and the volume change is recorded as the injection rate.

With the injection profile known, the spray amount can be integrated. Therefore, the calculated discharge coefficients, using Eq. 5.3.1, are obtained. The injection pressure is scanned from 40 MPa to 160 MPa to obtain a relation between the discharge coefficient and the injection pressure for pure diesel case, as seen in Fig. E.2. It is shown that as the injection pressure increases, the discharge coefficient also increases.

Calculated Discharge Coefficient, is found to be 1.03 for this case, which is literally 1 accounting for the uncertainties. Another set of repeated experiment is done with 140 MPa injection pressure, 1400 μ s preset time, 3 MPa back pressure with a total volume found to be 14.85 mm³. The discharge coefficient is found as 0.87.

Since the dieseline fuel data cannot be tested with the EFS machine, the following data is obtained with weighing method. Results are shown in Table E.1, with a preset injection duration of 1500 μ s. By counting the video frames for the injection, the

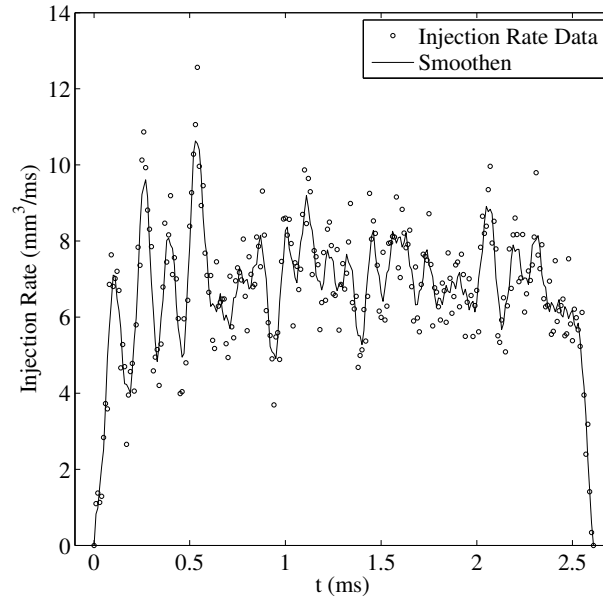


Figure E.1: Injection Rate Profile, $P_{inj} = 140$ MPa, 0.12 mm Nozzle Size, 3 MPa Back Pressure, 1400 μ s Preset Injection Time, 17.59 mm³ Total Injection Volume.

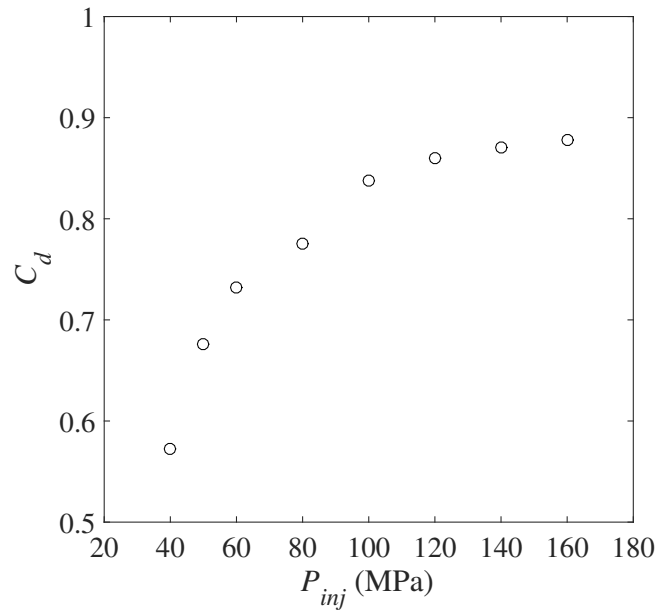


Figure E.2: Discharge coefficient v.s. injection pressure from EFS machine testing, injector diameter is 0.12 mm, preset injection duration 1400 μ s with back pressure is 3 MPa.

actual injection time is approximately $2900 \mu s$ for all the experiments taken.

Pressure MPa	G0 mg	G20 mg	G60 mg
140	14.656	13.862	13.171
130	13.899	13.258	12.491
120	13.228	12.710	11.909
110	12.461	12.134	11.275
100	11.791	11.293	10.622
90	11.074	10.614	9.783
80	10.193	9.840	9.277

Table E.1: Injection amounts for current nozzle used.

The above data leads to discharge coefficients Table E.2. The actual injection time is approximately $2900 \mu s$ from visualization. As is seen, the discharge coefficients are ranged from 0.81 to 0.93 for this injector.

Pressure (MPa)	C_d (G0)	C_d (G20)	C_d (G60)
140	0.932	0.893	0.870
130	0.917	0.886	0.856
120	0.909	0.884	0.850
110	0.894	0.881	0.840
100	0.887	0.860	0.830
90	0.878	0.852	0.806
80	0.857	0.838	0.811

Table E.2: Discharge coefficients for the current nozzle used.

The discharge coefficient relationship with injection pressure at different gasoline blended ratio is therefore obtained, in Fig E.3. The scale weighing method gives close results with the EFS testing. It is observed that as the gasoline percentage goes up, the discharge coefficient decreases.

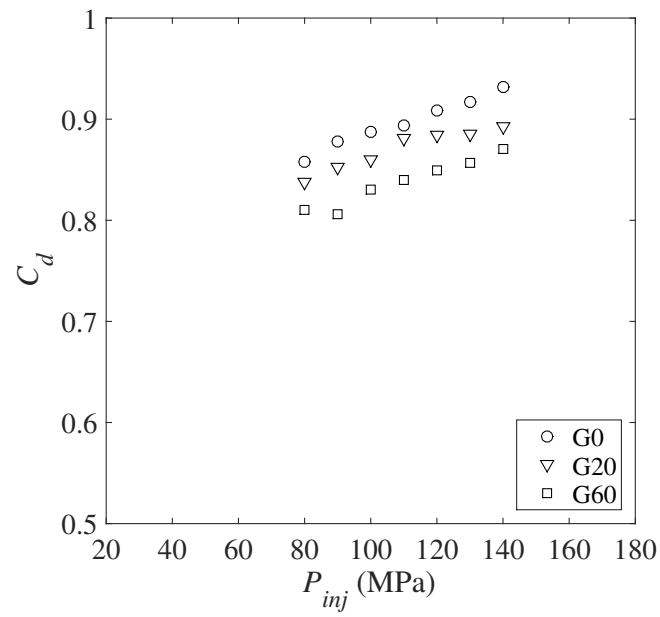


Figure E.3: Discharge coefficient v.s. injection pressure for different gasoline percentage, with injector diameter 0.12 mm, back pressure at 1 atm, preset injection duration of 1500 μ S